AERODYNAMIC CHARACTERIZATION OF A GRIFFITH-TYPE TRANSONIC, LAMINAR-FLOW AIRFOIL

BY

ARMANDO R. COLLAZO GARCIA III

THESIS

Submitted in partial fulfillment of the requirements
for the degree of Master of Science in Aerospace Engineering
in the Graduate College of the
University of Illinois at Urbana-Champaign, 2019

Urbana, Illinois

Adviser:

Assistant Professor Phillip J. Ansell

Abstract

An experimental investigation was conducted at the University of Illinois' Transonic Wind Tunnel Facility on a Griffith-type transonic airfoil to evaluate the effectiveness of its laminar flow qualities and boundary-layer flow-control characteristics in the transonic regime. Airfoil surface and wake pressure data were acquired to characterize the aerodynamic performance across a range of α = -2° − 2° and $M = 0.3 - 0.7$. In addition, surface-oil flow visualization, PIV, and Schlieren imaging were performed to identify the suction influence on boundary-layer transition, momemtum deficit alleviation in the wake, and stability of transonic shocks.

It was observed from the pressure distributions that the flow control application had a beneficial influence, allowing for a more aggressive pressure recovery downstream of the suction slot resulting in higher recovery pressure values at the trailing edge. At the design conditions of $M = 0.7$ and $\alpha = 0°$, a net profile drag reduction of 10.70% and an increase in the L/D ratio of 14.68% were observed when compared to no-suction conditions. Velocity flow field contours obtained from the PIV data showed an increase in the wake velocity magnitude for all Mach numbers at $\alpha = 0°$, displaying excellent agreement for the drag data at these conditions. Surface-oil flow visualization experiments revealed that the airfoil experienced extensive laminar flow runs regardless of suction application due to the low-Reynolds number test condition. The laminar flow was found to be shock limited followed by a laminar separation bubble in most cases. From the Schlieren experiments, a characteristic frequency of 22.38 Hz for the shock oscillatory process was identified at the design conditions which also was observed to stabilize under the influence of suction. In general, the improvements in aerodynamic efficiency and stability of the shock resulting from suction were observed to be greatest at higher angles of attack where the boundary layer was subjected to stronger-unforced pressure gradients.

To Mario and Wanda.

Soli Deo gloria.

Acknowledgments

I would like to first thank my parents, Mario and Wanda, for their unwavering support throughout my life without which I wouldn't be here. In particular, for supporting the desire of a 15-year-old to become a pilot which led to my current endeavors. Much appreciation goes to Bob Vargas for all the valuable life lessons which began at the golf course many years ago. I am also grateful for the guidance of Dr. Luis Gonzalez Linero and Dr. Rafael Rodriguez, both of whom helped guide me through my undergraduate studies and introduced me to research. Also, a special thanks goes to astronaut Sam Gemar for his help and advice as I made the decision to pursue graduate studies.

The family I have gained at the University of Illinois has made my graduate school experience worthwhile. I will forever be grateful to the Aerospace Engineering department for the opportunity of being a student here and for the liberty I have been given to explore my interests in aerodynamics. I am also thankful for the unconditional help and support I have received from all of my labmates. Thanks to Rohit Gupta, Georgi Hristrov, and Prateek Ranjan for great camaraderie and for sharing many ups and downs these past two years. Also, thanks to Emily Weerakkody for great input during my writing process.

Last but foremost, I would like to deeply thank my advisor Dr. Phillip J. Ansell for believing in me and allowing me to be part of the Aerodynamics and Unsteady Flows Research Group. Especially for the guidance, technical conversations, and countless hours in the lab from which I have learned more about aerodynamics than in any class I have ever taken.

Table of Contents

List of Tables

List of Figures

Nomenclature

a	speed of sound
A	airfoil cross-sectional area nondimensionalized by c^2
b_0	airfoil semispan
B_1	first Bernoulli polynomial
B_2	second Bernoulli polynomial
c	chord length
C_a	airfoil axial force coefficient
C_d	airfoil drag coefficient
C_{d_w}	wake drag coefficient
$C_d{}'$	drag coefficient parameter at each wake survey location
${C_{d_{max}}}'$	maximum value of $C_d{}'$
$C_{f,l}$	skin friction coefficient across the lower surface
$C_{f,u}$	skin friction coefficient across the upper surface
C_l	airfoil lift coefficient
C_m	airfoil quarter-chord pitching moment coefficient
$C_{m_{LE}}$	airfoil leading-edge pitching moment coefficient
C_n	airfoil normal force coefficient
C_p	airfoil pressure coefficient
$C_{p,crit}$	critical pressure coefficient
$C_{p,l}$	airfoil pressure coefficient across the lower surface
$C_{p,u}$	airfoil pressure coefficient across the upper surface
C_μ	suction momentum coefficient
f	frequency

F	acquisition rate
G	spectral density function
h	wind tunnel test section height
H	sidewall boundary-layer shape factor
I	pixel intensity
L/D	lift-to-drag ratio
M	Mach number
M_{crit}	critical Mach number
M_∞	freestream Mach number
$M_{\infty c}$	corrected Mach number
n	number of measured quantities in parameter calculation
N_S	number of samples
N_{ens}	number of realizations for ensemble average
p	general parameter calculated
P	static pressure
P_1	static pressure at a survey location behind the wake
P_∞	static pressure at freestream conditions
P_0	stagnation pressure
$P_{0,1}$	stagnation pressure at a survey location behind the wake
$P_{0,\infty}$	stagnation pressure at freestream conditions
P^*	porosity parameter
q_∞	freestream dynamic pressure
R	ideal gas constant
Re	Reynolds number
Re_x	Reynolds number at corresponding x location
S	constant dependent on μ_0 in Sutherland's law
S	raw signal
S_{ens}	extracted raw signal from number of realizations
T	static temperature

T	period
T_0	stagnation temperature
${T_1}^*$	total temperature in Sutherland's law
${T_0}^*$	reference total temperature in Sutherland's law
T^*	variable in Bernoulli polynomials
t/c	airfoil thickness-to-chord ratio
t/c_{max}	maximum airfoil thickness-to-chord ratio
u	x component of velocity
u_W	velocity correction
U	uncertainty
v	y component of velocity
v_W	incidence correction
V_∞	freestream velocity
V/V_∞	local velocity-to-freestream velocity ratio
V_s/V_∞	suction velocity-to-freestream velocity ratio
x	chordwise/streamwise direction
X	discrete Fourier transform
x/c	airfoil streamwise location-to-chord ratio
y	chord-normal/freestream-normal direction
y_w	wake-parallel direction

Greek Symbols

α	angle of attack
β	Prandtl-Glauert compressibility correction factor
δ	Pitot-static probe thickness
δ_0	upwash factor
δ_1	streamline factor
δ^*	sidewall boundary-layer displacement thickness
ΔC_d	drag coefficient correction

ΔM_∞	Mach number correction
$\Delta V/V_\infty$	nondimensional velocity difference between suction and no-suction conditions
$\Delta\alpha$	angle-of-attack correction
ϵ_S	solid blockage factor
ϵ_W	wake blockage factor
γ	ratio of specific heats
μ	doublet strength in the x direction
μ_0	dynamic viscosity at of air at reference conditions
μ_{air}	dynamic viscosity of air
ω	doublet strength in the y direction
Ω_S	solid blockage ratio
Ω_W	wake blockage ratio
ρ_∞	freestream air density
σ	source strength
τ	correction parameter dependent on P^* and β
θ	boundary-layer momentum thickness

Acronyms

DBD	dielectric barrier discharge
DFT	discrete Fourier transform
FFT	fast Fourier transform
HALE	high altitude long endurance
ISR	intelligence, surveying, and reconnaissance
LPM	liters per minute
NASA	National Aeronautics and Space Administration
NLF	natural laminar flow
OAR	open-area ratio
PIV	particle image velocimetry
PSD	power spectral density

RAE	Royal Aircraft Establishment
SLA	stereolithography
SNLF	slotted natural laminar flow
UIUC	University of Illinois at Urbana-Champaign
VFD	variable frequency drive

Chapter 1

Introduction

With aerodynamic efficiency and ecological concerns continuing to serve as driving parameters in new aircraft designs, the use of innovative technologies and design approaches to address present aerodynamic challenges such as drag reduction is paramount. Particularly to flight in the transonic regime, reducing skin friction drag is of high importance as, while being highly dependent on airfoil geometry it is also predominant at higher flight velocities. For transport aircraft, the wing profile drag has been estimated to be one of the largest contributors to drag, accounting for one third of the total drag at cruise conditions [1, 2]. The application of laminar flow airfoils to these types of aircraft could potentially offer a way to reduce the skin friction drag by extending the laminar flow region of the airfoil boundary layer further aft than current transonic airfoil designs [3, 4]. In fact, at the airplane level, the net drag reduction benefits of laminar flow control have been estimated through NASA-supported studies to be as high as 10% [5].

In addition to commercial transport aircraft, there is another category of aircraft that operates in the transonic regime that could benefit from aerodynamic performance improvements resulting from laminar flow. This class of aircraft, known as High-Altitude, Long-Endurance (HALE), are commonly used for intelligence, surveying, and reconnaissance (ISR), communications relaying, weather and agricultural monitoring, and other applications requiring satellite-based systems [6–11]. Generally, these aircraft are designed to operate for long periods of times at target altitudes of up to 35 km [12]. For example, the Global Hawk used by the U.S. Air Force for ISR has a service ceiling of 60,000 ft. and endurance of more than 34 hours. Hence, this high-altitude operating requirement presents an unconventional application outlined by low Reynolds number and transonic Mach number conditions. As a result, these aircraft are also characterized by lower wing loadings (larger surface area), which poses a need for highly efficient airfoil sections in order to minimize the viscous drag component and increase aerodynamic efficiency.

It is evident that aircraft operating in the transonic regime can benefit from the improvements in aerodynamic efficiency that are provided by laminar flow technology. This introduces an alternative way of

increasing aircraft efficiency from an aerodynamic design perspective, rather than by just improving power plant efficiency as is recently been done. However, laminar-flow airfoils have generally been designed for low-speed and low-Reynolds number applications as these conditions allow for better control and tailoring of the boundary-layer transition process. Flight in the transonic regime introduces challenging influences that promote transition, such as shock waves and cross flow under swept wings, for example, that limit the ability to retain laminar flow. Therefore, different design considerations using different methods of flow control (instead of the conventional natural-laminar-flow approaches used for low speeds) should be considered for transonic, laminar-flow airfoils. This investigation intends to indentify the laminar flow capabilities, aerodynamic performance gains, and transonic characteristics of a laminar-flow airfoil concept using active flow control through boundary-layer suction.

1.1 Laminar Flow Technology and Challenges in a Transonic Flow Field

The idea of natural-laminar-flow (NLF) airfoils has been widely studied for low-speed configurations and recently has gained interest for applications to transonic aircraft [1, 2, 13, 14]. However, studies have shown that the implementation of an NLF transonic wing poses a substantial challenge for conventional commercial transport aircraft due to the associated high leading edge sweep angles and high operating Reynolds numbers [15]. Historically, the application of NLF airfoils has been constrained to low sweep, low-Reynolds number conditions, as both of these parameters have a direct influence on the growth of modal instabilities, such as the natural growth of Tollmien-Schlichting (T-S) waves and cross-flow modes that promote early transition [3, 4]. However, there have been attempts to achieve NLF at transonic conditions with limited success.

An example of an NLF transonic airfoil was the HSNLF(1)-0213 designed to operate at $M = 0.7$, $C_l = 0.25$, and $Re = 11 \text{ x } 10^6$ [16]. The application of this airfoil was intended for a single engine business jet with no sweep. The constraint on the sweep already poses a limitation on the maximum achievable Mach number of an aircraft due to the inability of NLF designs to sustain laminar flow under cross-flow instabilities. Due to compressibility effects, at higher C_l values the flow across the upper surface of the airfoil continues to accelerate, increasing the extent of the favorable pressure gradient region rather than achieving high suction peaks near the leading edge as is common in an incompressible-flow condition. It was found during the development of the airfoil that this favorable pressure gradient region which terminated in a shock led to a steep aft pressure recovery which was very susceptible to separation. The final geometry was tailored for a

shock-free design with favorable pressure gradients extending to 55%c on the upper surface and 65%c on the lower surface. Also, the turbulent pressure recovery across the upper surface of the airfoil was optimized to prevent separation [16]. Even though this case study demonstrates the capabilities of obtaining laminar flow at very high speeds, it does not technically qualify as a transonic application since the final geometry was tailored to not have shocks and therefore no local supersonic region.

Another concept that has recently been studied is the slotted, natural-laminar-flow airfoil (SNLF) [1, 2, 13, 14]. The SNLF concept involves a two-element airfoil which is able to extend the laminar flow capabilities beyond the limits of current airfoils. By introducing an aft element, the pressure is no longer required to recover to freestream conditions at the trailing edge of the fore element, allowing the favorable pressure gradient to be extended across a significantly larger portion of the chord. In addition, since the wake of the fore element does not impinge on the aft element, laminar flow across this smaller aft element of the airfoil could also be achieved [13]. The aft element is then responsible for recovering the pressure over a shorter distance as momentum is added to the boundary layer through the slot, allowing the boundary layer to sustain a larger recovery pressure gradient without separating. The concept shows potential to significantly increase the extent of laminar flow regions when compared to conventional airfoil designs, experimentally shown to be transition free at low-Reynolds number and low-speed conditions at a notable angle-of-attack range [13]. However, the airfoil's ability to retain laminar flow under moderate sweep, at off-design conditions, at higher Reynolds numbers, and in the presence of transonic shocks across the surface of the airfoil should be considered. Additionally, special treatment should be given to the design of the slot considering the possibility of choking at higher transonic Mach numbers.

Laminar-flow airfoils with active boundary-layer control could potentially be used as an alternative to natural-laminar-flow approaches. These airfoils are designed with some form of actuation to actively control the boundary layer, extending the region of laminar flow across the surface. For example, active transition control can be performed through means of pressure gradient control, mean wall-temperature control, wall suction, and recently by using dielectric barrier discharge (DBD) plasma actuators. These approaches inhibit the growth of T-S waves, and in some cases crossflow instabilities, in order to prevent or delay boundary-layer transition [17–19]. The application of Griffith's airfoil concept, which uses active boundary-layer control through suction, is explored in this study as a method of achieving laminar flow in transonic conditions.

1.2 Griffith's Laminar-Flow Airfoil Concept

The concept of suction-enabled laminar flow airfoils was first introduced by Griffith in the early 1940's [20, 21]. Griffith's airfoil was designed to have a favorable pressure gradient across most of the upper surface. However, as the streamwise portion of the airfoil designed with a favorable pressure gradient region is increased, the pressure must recover across shorter distances and stronger adverse pressure gradients which may lead to detrimental characteristics such as boundary-layer separation. To overcome the performance penalties associated with such traits, the pressure recovery was aided through a suction slot located near the airfoil trailing edge. Given that the suction system allowed the pressure to be recovered to freestream values across short distances without separating, the airfoil experienced extensive laminar flow runs across the upper surface as a result of the extended favorable pressure gradient region dictated by the airfoil geometry. This feature resulted in significant skin friction drag reductions relative to conventional airfoil designs at the time [21].

Similar design methods were also used by Goldschmied [22]. One of his most noteworthy designs was the thick-wing spanloader which incorporated a centrifugal blower to provide boundary-layer suction. This approach enabled a Griffith-type, laminar-flow airfoil concept to be used, where the blower exhaust was then routed out the trailing edge of the airfoil [22]. This mass ejection out of the trailing edge in the design provided an extra source of thrust, which also contributed to offsetting the skin friction drag component of the airfoil.

It has been shown through many studies that large lift coefficients and drag performance benefits can be obtained from these types of suction-enabled airfoils [23]; however, as previously mentioned laminar-flow airfoils have typically been designed for low speeds, making them incompatible for transonic applications. For example, Griffith's airfoil t/c of 0.30 limits its M_{crit} to a very low value, leading to significant compressibility losses at transonic Mach numbers of transport-class aircraft. In the case of HALE aircraft which have larger t/c to achieve lofty C_l requirements, consideration should be given to the tradeoff between compressibility losses and the effects of laminar separation bubbles which are typical at their low-operating Reynolds numbers. Nevertheless, the use of Griffith's pressure recovery across a limited region assisted by suction upstream of the trailing edge can be implemented in the design of laminar-flow airfoils for transonic applications.

1.3 Research Motivation

As new and improved aircraft designs are developed, it can be seen that focus has been given to engine efficiency, lowering fossil-fuel consumption, and reducing the emission-based carbon footprint of aviation. These considerations are all targeted to the power generating aspect of the aircraft that produces the required thrust to sustain flight. With the exception of a number of new clean-sheet aircraft designs, little importance has been given to improving the efficiency of an aircraft from an aerodynamic design perspective as new aircraft being developed are mostly based from existing designs with modifications that only improve engine efficiency and add novel capabilities. Therefore, innovative aerodynamic concepts that push the limits of existing performance boundaries should be implemented in the development of next generation aircraft. In particular, laminar-flow technology should be considered for transonic wing designs as skin friction drag is a major contributor of the overall drag of an aircraft at high speeds. This technology displays the ability to provide substantial reductions in drag increasing the aerodynamic efficiency of wings, which in turn will lead to reduced fuel consumption. However, to develop adequate wing concepts able to significantly increase current laminar flow capabilities in a transonic flow field, there first needs to be suitable airfoil designs capable of achieving and maintaining laminar flow in the same flow conditions. This initially requires extensive wind tunnel testing to evaluate airfoil performance and identify characteristics not captured in simulations to facilitate further advancement of airfoil concepts.

1.4 Research Objectives

The purpose of this investigation is to assess the ability of Griffith's airfoil concept to provide laminar flow and improve aerodynamic efficiency in a transonic flow field. For this study a transonic, laminar-flow airfoil developed by Perry et al. [21] and Kerho et al. [24] using Griffith's method of suction for pressure recovery was used. The the magnitude of increased aerodynamic efficiency that can be obtained from this airfoil is considered by comparing its performance to that of the same geometry without suction applied as well as to another transonic airfoil. In addition, the study aims to identify important characteristics of the airfoil that are relevant to operation in a transonic flow field. This approach could be used to further improve the airfoil design considering tradeoffs between aerodynamic benefits obtained and compressibility losses in the transonic regime. These goals were attained through the collection of pressure data that allowed

the aerodynamic performance of the airfoil to be characterized, as well as the use of other experimental diagnostics tools such as PIV, surface-oil flow visualization, and Schlieren imaging to identify relevant wake effects, transitions characteristics, and shock behavior. In general, the specific objectives of the experimental investigation on the Griffith-type transonic, laminar-flow airfoil are outlined as follows:

- Understand the boundary-layer suction influence on the C_p distributions of the airfoil and the effect on the pressure recovery
- Characterize the aerodynamic performance across a range of angles of attack and Mach numbers as well as determine the magnitude of profile drag reduction and improved lift-to-drag performance that can be achieved
- Analyze the influence in the laminar flow capabilities and transition characteristics of the airfoil under the influence of boundary-layer suction
- Identify the effect of suction on the development, stability, and strength of the resultant transonic shock across the upper surface of the airfoil

Chapter 2

Experimental Methodology

This chapter introduces the different methods and experimental techniques used during the investigation performed at the University of Illinois at Urbana-Champaign (UIUC). Detailed descriptions of the test facility, data acquisition equipment and execution, calculation of aerodynamic parameters, and test setup and configurations are provided within.

2.1 Transonic Wind Tunnel Experimental Facility

The experimental campaign for this investigation was conducted in the newly-developed Transonic Wind Tunnel Facility at UIUC. The test facility is housed in the dedicated laboratory room 131 in the Aerodynamics Research Laboratory. This transonic wind tunnel is a suction-type, open-return wind tunnel featuring a test section with a cross-sectional area measuring 6" by 9" and running 18" in the streamwise direction. Figure 2.1 shows the transonic wind tunnel used.

In order to condition the flow going into the test section, the tunnel houses a settling chamber in the inlet section with an initial layer of honeycomb followed by three layers of turbulence-reducing screens. Essentially, the honeycomb acts as a flow straightener initially reducing large-scale turbulence associated with swirling of the flow during entry, while the subsequent screens reduce the overall turbulence intensity of the flow (some of which is generated by shear layer instabilities and Reynolds stresses associated with the honeycomb) improving angularity and velocity uniformity [25–28]. The ratio between the inlet and test section of the tunnel is 27.88. This configuration resulted in turbulence intensities of less than 0.04% at all Mach number conditions determined through Particle Image Velocimetry (PIV) experimentation.

In transonic wind tunnel testing, porous or slotted test-section wall bondaries are generally incorporated in test sections to help mitigate compressibility effects such as shock reflections from the walls and artificial curvature of streamlines at high dynamic pressures [29]. Consequently, this wind tunnel was designed with

6% open-area ratio top and bottom walls with 0.25” thickness and a hole diameter-to-thickness ratio of 1. The holes were also machined at an angle of 60° relative to the surface. This feature allows a desired pressure difference between the test section and plenum chamber to be achieved with a lower open-area ratio. In turn, it also helps the flow from reentering into the test section when the pressure in the plenum chamber is higher than that of the test section due to the extra pressure head the flow must overcome [29]. Both upper and lower sides of the porous test section have a 2” plenum chamber that serves as a bypass region to the flow coming out of the test section. The pressure in this plenum can be controlled to some extent using suction flaps located downstream of the test section, which control the amount of air that exits the plenum into the diffuser. Initially, a sensitivity study was performed to verify the influence of the suction flap locations. It was observed that after some small extent of the flap opening, no further significant change was observed in the C_p distribution of the model. Furthermore, setting them fully open did not have a detrimental effect on the wind tunnel performance. For these reasons, the plenum flaps were set at 90° relative to the wall orientation throughout this investigation. The top porous wall and plenum were also fitted with a 6.0” × 0.07874” slot to allow for the passage of a laser sheet in order to perform PIV experiments.

The test section was also fitted with removable sidewalls in order to install and remove airfoil models. These walls were designed with an acrylic insert of 9.30” × 7.15”. The set of windows provided a means to observe the aerodynamic model during testing for any abnormalities as well as allowed for optical access required in certain experimental techniques. The acrylic inserts were drilled with holes for support spars to pass through at a 5” location in the streamwise direction and at a half test-section height location. This approached allowed for the installation of aerodynamic models with spars having a diameter of up to approximately 0.5”. The left spar of the models installed was passed through an Accu-CoderPro™ Programmable Incremental Encoder Model 58TP manufactured by Encoder Products Company with a rated accuracy of ±0.015° from true position. This encoder has a 0.5” thru-bore fitting which was fixed to the shaft of the model to track the angle-of-attack position. The encoder was programmed with 36,000 counts per revolution, which provided a resolution of 0.01°. The encoder index location (which indicated the 0° angle-of-attack position) was also programmed during the installation using a stencil of the airfoil alongside a level. The angle-of-attack readings were then observed and recorded using a US Digital® ED3 Digital Encoder Display which converted the differential quadrature signals into degree measurements through an internal firmware.

Once fitted through the encoder, the model was connected through a shaft-coupling linkage mechanism to an Anaheim Autonation 34 MDSI214S stepper motor. This stepper motor had a 1,200 oz-in maximum holding torque and a 0.225° resolution using microsteps. The same stepper motor model was used for control of the suction plenum flaps in the plenum chamber.

The wind tunnel was powered via an ABB ACS880 variable frequency drive (VFD). This VFD was used to control the power to a Baldor-Reliance 255 HP motor which was responsible for driving the AirPro model 420 centrifugal blower at the diffuser end of the wind tunnel. The reason this tunnel is operated via a centrifugal blower rather than a conventional fan is because a centrifugal blower is able to accommodate larger pressure losses inside of the test section which are inherent to transonic conditions. The maximum motor operating setting of approximately 2,120 RPM resulted in a maximum Mach number of 0.85 for an empty test section. However, when an experimental airfoil model with chord of 6" is introduced, the maximum Mach number reached is approximately 0.725. The maximum Mach number also varied with variations in angle of attack as the blockage introduced by the model changed.

The operating Mach number and freestream velocity were determined based on the stagnation pressure, static pressure in the test section, and ambient temperature in the laboratory. The pressures were measured using two OMEGA® PX409-030A5V-EH pressure transducers which had a rated accuracy of ±0.05%. The stagnation pressure measurement was taken downstream of the settling chamber where the flow velocity was considered to be negligible compared to that in the test section; hence, the static pressure measured was assumed to be same as the stagnation pressure in this region. The static pressure measurement under a non-zero dynamic pressure was taken through a pressure tap located in the upstream end of the test section ceiling. The freestream Mach number (M_∞) was then calculated using the following isentropic relationship:

$$\frac{P}{P_0} = \left(1 + \frac{\gamma - 1}{2} {M_\infty}^2\right)^{\frac{-\gamma}{\gamma-1}} \tag{2.1}$$

where P is the static pressure, P_0 is the stagnation pressure, and γ is the ratio of specific heats.

In order to also determine the actual freestream velocity in the test section, stagnation temperature measurements of the laboratory conditions were taken using a National Instruments USB-TC01 J-type thermocouple. The static temperature was then calculated using the following relationship:

$$\frac{P}{P_0} = \left(\frac{T}{T_0}\right)^{\frac{-\gamma}{\gamma-1}} \tag{2.2}$$

where T is the static temperature and T_0 is the stagnation temperature.

Using the static temperature calculated for the test section, the speed of sound (a) and freestream velocity (V_∞) were calculated using:

$$a = \sqrt{\gamma RT} \tag{2.3}$$

$$V_\infty = M_\infty a \tag{2.4}$$

where R is the ideal gas constant.

2.2 Airfoil Models

2.2.1 Griffith-Type Transonic, Laminar-Flow Airfoil

The airfoil used for this experimental investigation was the Griffith-type transonic, laminar-flow airfoil developed by Perry et al. [21] and Kerho et al. [24] for application in a commercial-transport aircraft. An in-depth analysis of the development of the airfoil can be found in References [21] and [24]; however, a general overview of the design criteria and resulting airfoil characteristics are discussed.

The objective of the Griffith airfoil is to achieve extensive regions of laminar flow across the airfoil surface. This is done by tailoring the airfoil geometry to have regions of favorable pressure gradient across most of the upper surface which promote laminar flow. The pressure is then recovered rapidly across a short recovery region by means of boundary-layer suction through a slot located near the trailing edge, which helps maintain attached flow in the presence of a strong adverse pressure gradient [20]. Early experimental work from Richards et al. [20] at low-Reynolds numbers and low-subsonic conditions demonstrated that an effective suction location for such an airfoil concept was located near the trailing edge pressure recovery region, around $x/c = 0.70$. The effect of the slot width and mass flow suction was also part of the aforementioned investigation [20]. It was found that the proportion of the boundary-layer volume removed did not increase when varying the slot width size in the chordwise direction for a fixed suction amplitude for slot widths greater than approximately 70% of the boundary-layer thickness. In a similar way, the required proportion of the boundary-layer volume that had to be removed in order to prevent separation did not in-

crease as the slot width was increased up to the thickness of the boundary layer at the suction chordwise location [20].

In order to design a transonic, laminar-flow airfoil incorporating the Griffith concept, a number of design constraints were set considering desired performance objectives. Commercial aircraft that operate at transonic speeds have airfoil thicknesses that typically range from t/c of 9%-12%. In order to produce a reasonable M_{crit} for the candidate airfoil, a design constraint of t/c_{max} = 15% was set. The design Mach number was set to 0.7, also representative of operational speeds of airfoil sections for modern commercial and business aircraft. While this operational Mach number is lower than the vehicle cruise speed used in modern transonic air transport vehicles, this design condition could be utilized with a limited extent of sweep to mitigate adverse compressibility effects at higher vehicle cruise Mach numbers.

An inverse airfoil design code, Profoil, was used to generate the airfoil geometry based on desired C_p distribution characteristics of a nominal laminar-flow airfoil. An example of a notional, transonic laminar-flow C_p distribution is presented in Fig. 2.2, after Cella et al. [30] at three different flight configurations. Validation of the designed airfoil shape was performed using OVERFLOW CFD to obtain predictions of the airfoil performance which are included in Reference [21]. The final airfoil presented by Perry et al. [21] and Kerho et al. [24] has a t/c of 12.48% and was designed to produce extensive laminar flow at a freestream Mach number of 0.7 and angle of attack of 0°. Transition across the upper and lower surfaces was predicted to occur at $0.57c$ and $0.45c$, respectively, at the design Re of 16.2 million. The suction slot has a location between $0.825c$ and $0.875c$, with a design suction V_s/V_∞ = 6.5% or C_μ = 0.00014 [21, 24]. A rendering of the transonic airfoil design is presented in Fig. 2.3.

A small-scale model of this airfoil was designed and built in order to measure its aerodynamic performance at the full-scale Mach number and a transitional Reynolds number range. The chord and span were selected to be 6", allowing the airfoil to occupy the entire test section in the spanwise direction when mounted horizontally to help mitigate three-dimensional effects during testing. An array of 41 pressure taps with outer diameter of 0.045" were incorporated into the model and routed internally through the left spar of the model to obtain static pressure measurements across the upper and lower surfaces of the airfoil. The taps were manufactured with a 12° sweep angle in the streamwise direction to reduce the influence of disturbances and possible boundary-layer transition induced by upstream pressure taps in the acquired measurements. The model was designed in a two piece assembly, such that the internal cavity served as a

suction plenum with an opening at the desired suction location on the airfoil. Originally, the leading edge portion of the airfoil model was manufactured from polished aluminum while the trailing edge portion was 3D printed using stereolithography (SLA). The SLA trailing-edge part featured internally routed pressure taps and was only used during the acquisition of the surface pressure data and for PIV experiments. An identical trailing-edge piece constructed of polished aluminum was substituted when wake pressure data were taken and when performing Schlieren experiments. The main body of the model consisting of the leading-edge and trailing-edge parts described spanned 5.2". Two aluminum side plates, having the same airfoil geometry and thickness of 0.25", were fastened to the main body to serve as an interface with the spar support. Lastly, two Teflon® covers also with the same airfoil geometry and thickness of 0.15" were fixed to each side to avoid scratching between the experimental model and the sidewall.

In order to provide suction to the airfoil, a pneumatic shaft was attached to the right side of the model. This shaft also served as a structural spar to support the model at the quarter-chord point. The suction slot was fitted with interchangeable cover plates, one with the $0.05c$ slot open area across the span and the other completely covered to allow for testing of the baseline airfoil without any suction applied. Due to size constraints and experimental limitations, mass ejection out the trailing edge could not be implemented in the experimental model as was used by Goldschmied [22] and also considered in the development of the original airfoil design [21, 24]. A photograph of the experimental model is presented in Fig. 2.4, mounted inside the test section of the wind tunnel.

Suction to the airfoil model was applied across the slot on the airfoil by means of a Venturi suction pump, which was connected through pneumatic lines at the end of the pipe internally routed to the suction plenum inside of the model. The Venturi pump used was a VACCON Model VDF750-ST16C. The pneumatic line from the suction pump was routed through a mass flow meter in order to record the suction being applied at the slot during different test configurations. For this an Alicat Scientific M-Series Model M-3000SLPM-D/5M mass flow meter configured for air was used having a rated accuracy of ±0.8% of the measurement reading. The varied suction requirements through the different test configurations were controlled through a pressure regulator located prior to the air supply of the Venturi pump.

2.2.2 RAE 2822 Transonic Airfoil

In order to directly compare the performance benefit of the boundary-layer, suction-enabled design of the Griffith-type airfoil, aerodynamic data from other airfoil geometries designed to operate in the same regime are beneficial. Furthermore, due to the inherent limitations of the transonic test facility, data for transonic airfoils at the low Reynolds numbers achieved during experimental runs are hard to obtain. For this, an RAE 2822 model was fabricated and tested at the same flow conditions in order to provide a means of comparison.

The RAE 2822 airfoil, developed by the Royal Aircraft Establishment, was selected for its well-known transonic characteristics. This airfoil is also frequently used as a canonical case for numerical and experimental studies, as well as for CFD validation. In addition, there are historical data at similar low Reynolds number conditions (2.7 million) to those achievable in the transonic test facility, providing an additional source of validation for the RAE 2822 data and ensuring reliability of the acquired measurements. Therefore, it was fitting to select this model as a basis of comparison.

The original geometry of the RAE 2822 has a sharp trailing edge which poses difficulties in its manufacturing and internal pressure tap routing. A modification to the original RAE 2822 airfoil geometry was used to incorporate a discrete-finite trailing edge. This modification was performed using XFOIL's built-in function TGAP. This function allows the user to define the gap between upper and lower surfaces of the trailing edge along with a blending distance defined from the leading edge which controls the degree of blending between the newly-defined trailing edge to the original airfoil geometry [31]. For the modified RAE 2822 geometry, a trailing-edge gap thickness of 0.066" was set alongside a blending distance of $0.25c$. The resultant geometry can be seen in Fig. 2.5.

An experimental model was built using the modified RAE 2822 airfoil with the same chord and span lengths of 6", resulting in an aspect ratio of 1. The span extending the width of the test section limited three-dimensional influences that would be caused at the tips of the model, while the 6" chord ensured that the same chordwise Reynolds numbers would be achieved at the different Mach numbers being tested. Similarly to the Griffith experimental model, the main body of the airfoil extended 5.2" inches in span. Two sideplates with the same airfoil geometry, each with a width of 0.25", were fastened to both sides of the main body to interface with the structural supports. Two shafts with 0.5" diameter were welded to the sideplates at the quarter-chord location of the airfoil. These shafts served as structural spars to appropriately set the angle-of-attack conditions as well as support the model during testing. Additionally, two Teflon® covers

with the same airfoil geometry and thickness of 0.15" were fixed to the ends of the sideplates to avoid any possible scratching on the sidewalls. This design having the main airfoil body as a single shell facilitated the installation of internal pressure taps. Similarly, an array of 40 pressure taps were incorporated along the upper and lower surfaces of the airfoil. These taps were used to record static pressure measurements that would then be utilized to calculate integral aerodynamic coefficients of lift and moment. The taps were also manufactured with a 12° sweep angle in the streamwise direction. This feature helped to ensure that the boundary-layer region over a pressure tap would not be artificially contaminated (transitioned) by the influence of upstream taps. The RAE 2822 experimental airfoil model can be seen mounted inside the wind tunnel in Fig. 2.6.

2.3 Aerodynamic Wind Tunnel Tests

To characterize the aerodynamic performance of the airfoils being tested, integral aerodynamic coefficients were calculated using a combination of airfoil-surface pressure measurements as well as wake pressure measurements. The following subsections outline the data acquisition and calculation processes as well as the wind tunnel corrections applied.

2.3.1 Airfoil-Surface Pressure Measurements

Airfoil-static pressure measurements were taken through the pressure taps internally routed through the airfoil model as previously described in Sections 2.2.1 and 2.2.2. The metal tubing of the pressure taps, which were accessed through the left spar of the model outside of the test section, were connected via polyurethane tubing with inner diameter of 0.045" to interface with the pressure measurement system. The pressure readings for the Griffith airfoil-surface pressures as well as all wake pressures (for both airfoil models) were acquired using a Pressure Systems Incorporated (PSI) NetScanner Pneumatic Intelligent Pressure Scanner system, Model 9116. A new DTC Initium Data Acquisition System with a PSI 64-channel 15 PSID ESP Miniature Pressure Scanner system was also acquired and used for the surface pressure measurements of the RAE 2822. However, both systems were manufactured by the same supplier and had the same basic performance and precision characteristics mostly differing by the number of available channels.

The PSI NetScanner system featured 16 channels, 12 of which were rated at 15 PSID. These channels were the only ones used to ensure the best resolution in the data. The rated accuracy of the system was

given to be ±0.05% of the full-scale reading. The system also had a supply port incorporated for inert gas in order to provide pressure when operating an internal valve mechanism for calibration of the pressure ports. For this, high-purity nitrogen was used and supplied at a pressure of 100 PSI as recommended by the manufacturer. The system was recalibrated before each experimental run. Since the individual pressure transducers measure a pressure differential relative to a reference value, the system has a dedicated port for a reference pressure to be supplied which was referenced by each of the individual transducer channels. During testing, this reference pressure port was connected to the freestream static pressure in the test section. This allowed the difference between the local surface pressure and the freestream conditions to be directly measured, making it easier to directly compute local C_p values. The pressure data were acquired at a sampling rate of 30 Hz for 10 seconds and subsequently averaged for each test case.

The PSI 64-channel 15 PSID Miniature ESP Pressure Scanner system coupled with the DTC Initium Data Acquisition system worked in a similar way, varying mostly in the additional total number of channels that could be sampled at a given time. The accuracy rating was also ±0.05% of the full scale reading. Similarly, the system was calibrated by supplying nitrogen at 100 PSI, and the pressure differential was based on a reference pressure port which was connected to the freestream static pressure. Sampling was performed at a frequency of 50 Hz for 5 seconds for which data were then averaged.

Pressure Coefficient Calculation

In order to calculate the pressure coefficient distribution about the airfoil, the freestream dynamic pressure had to be determined. Since operating in the transonic regime where incompressible assumptions do not hold and no direct measurement of the freestream density in the test condition was available, the dynamic pressure was determined by subtracting the stagnation pressure and test-section static pressure measurements using the pressure transducers described in Section 2.1. Equation 2.5 shows the calculation for dynamic pressure which was performed through the data acquisition software described in Section 2.3.3. In Eq. 2.5, P_0 is the stagnation pressure and P is the static pressure, both assumed to be at freestream or test-section conditions.

$$q_\infty = P_0 - P \tag{2.5}$$

The C_p was then calculated using the following relationship:

$$C_p = \frac{P - P_\infty}{q_\infty} \tag{2.6}$$

where $P - P_\infty$ is the difference between the surface-static pressure at a particular airfoil location and the freestream static pressure. This value was directly recorded which allowed the C_p values to be calculated and recorded through the data acquisition program.

Lift and Moment Coefficients Calculation

The two-dimensional lift and moment coefficients were obtained by integrating the pressure distributions obtained from the airfoil. It is known that all aerodynamic forces and moments produced on an airfoil shape result from pressure and shear-stress distributions. Hence, the following expressions for the normal force (perpendicular to the chordline), the axial force (parallel to the chordline), and the moment about the leading edge can be derived for an airfoil only considering pressure and shear stress in nondimensional coefficient form as follows:

$$c_n = \frac{1}{c}\left[\int_0^c \left(C_{p,l} - C_{p,u}\right) dx + \int_0^c \left(C_{f,u}\frac{dy_u}{dx} + C_{f,l}\frac{dy_l}{dx}\right) dx\right] \tag{2.7}$$

$$c_a = \frac{1}{c}\left[\int_0^c \left(C_{p,u}\frac{dy_u}{dx} - C_{p,l}\frac{dy_l}{dx}\right) dx + \int_0^c \left(C_{f,u} + C_{f,l}\right) dx\right] \tag{2.8}$$

$$\begin{aligned} c_{m_{LE}} = \frac{1}{c^2}\Bigg[&\int_0^c \left(C_{p,u} - C_{p,l}\right) x dx - \int_0^c \left(C_{f,u}\frac{dy_u}{dx} + C_{f,l}\frac{dy_l}{dx}\right) x dx \\ &+ \int_0^c \left(C_{p,u}\frac{dy_u}{dx} + C_{f,u}\right) y_u dx + \int_0^c \left(-C_{p,l}\frac{dy_l}{dx} + C_{f,l}\right) y_l dx\Bigg] \end{aligned} \tag{2.9}$$

where the subscripts u and l indicate upper and lower surfaces of the airfoil respectively, C_f is the skin friction coefficient, and $\frac{dy}{dx}$ is the local slope of the airfoil surface. As can be seen from Eqns. 2.7 and 2.8, it can be noticed that the contribution of the skin friction component acts primarily on the axial component of the force and has a negligible effect on the normal component as it is being multiplied by the local airfoil slope which is generally very small. Since the lift coefficient (Eq. 2.13) depends primarily on the normal component of the force, particularly at low angles of attack which happens to be the case in this investigation, the skin friction terms can be ignored and the coefficients become:

$$C_n = \frac{1}{c} \int_0^c \left(C_{p,l} - C_{p,u}\right) dx \tag{2.10}$$

$$C_a = \frac{1}{c} \int_0^c \left(C_{p,u} \frac{dy_u}{dx} - C_{p,l} \frac{dy_l}{dx}\right) dx \tag{2.11}$$

$$C_{m_{LE}} = \frac{1}{c^2} \left[\int_0^c \left(C_{p,u} - C_{p,l}\right) x dx + \int_0^c C_{p,u} \frac{dy_u}{dx}\, y_u dx - \int_0^c C_{p,l} \frac{dy_l}{dx}\, y_l dx\right] \tag{2.12}$$

This assumption, however, does limit the parameters that we can obtain from surface-pressure data to C_l and C_m, since C_d is highly dependent on the axial component of the force.

The upper surface of the airfoil was fitted with 24 pressure taps and the lower surface with 17 pressure taps that were spanned across the chord at locations of interest. Therefore, to calculate the integral parameters from Eqs. (2.10) to (2.12), the trapezoidal rule was implemented, where the mean pressure values between two adjacent pressure taps were assumed to define the pressure distributions across the upper and lower surfaces. The final coefficients were obtained by taking the difference between the upper and lower surface contributions as indicated by each respective equation.

With the C_n, C_a, and $C_{m_{LE}}$, the lift and moment coefficients were calculated using the following relationships:

$$C_l = c_n \cos(\alpha) - c_a \sin(\alpha) \tag{2.13}$$

$$C_m = C_{m_{LE}} + \frac{1}{4} C_l \tag{2.14}$$

where C_l is the lift coefficient, α is the angle of attack, and C_m is the moment coefficient about the quarter-chord location.

2.3.2 Pitot-Static Wake Survey Traverse

As was discussed in Section 2.3.1, the drag generated by an airfoil is highly dependent on shear-stress influences that were neglected in the formulation of the axial force coefficient. Therefore, a pitot-static wake survey traverse was installed in the test section to capture the pressure deficits in the wake generated by the

airfoil under different test conditions. The wake survey traverse featured a single pitot-static probe with a single stagnation pressure orifice measuring 0.015", four static pressure orifices measuring 0.0265", and an external diameter of 0.125". The probe was located at the center of the test section and 3.8" behind the airfoil model and was traversed vertically at 0.05" intervals using a ZABER Model T-LSR450B motorized linear traverse installed outside of the plenum chamber. Pressure data were obtained across a 2" region in order to ensure that the entirety of the wake was captured. This traversing region was determined during initial experimental runs where the stagnation pressure was observed to be constant and the wake tails could be identified. On average, the wake occupied a 0.5" linear region. The pressure measurements were obtained using the same PSI NetScanner system introduced in Section 2.3.1. Pressure data were taken for 5 seconds at a frequency of 30 Hz at each traverse location. An image of the pitot-static wake survey traverse system installed in the transonic wind tunnel can be seen in Fig. 2.7.

Drag Coefficient Calculation

Drag coefficients were obtained using the stagnation and pressure measurements obtained across the wake region using Betz's method found in Reference [32]. This method is advantageous for the current study, as it allows for the survey to be performed at a location where the pressure and velocity have not yet recovered to freestream conditions, while taking into account compressibility effects. The method utilizes a momentum conservation approach for which the following relationship is obtained for each location along the wake:

$$C_d{}' = 2\left(\frac{P_{0,1}}{P_{0,\infty}}\right)^{\frac{\gamma-1}{\gamma}}\left(\frac{P_1}{P_\infty}\right)^{\frac{1}{\gamma}}\left\{\frac{1-\left(\frac{P_1}{P_{0,1}}\right)^{\frac{\gamma-1}{\gamma}}}{1-\left(\frac{P_\infty}{P_{0,\infty}}\right)^{\frac{\gamma-1}{\gamma}}}\right\}^{\frac{1}{2}}\left[1-\left\{\frac{1-\left(\frac{P_\infty}{P_{0,1}}\right)^{\frac{\gamma-1}{\gamma}}}{1-\left(\frac{P_\infty}{P_{0,\infty}}\right)^{\frac{\gamma-1}{\gamma}}}\right\}^{\frac{1}{2}}\right] \tag{2.15}$$

Once the distribution of $C_d{}'$ values are calculated for each location surveyed in the wake region, they can be integrated to obtain the two-dimensional drag coefficient (C_d) in the following way:

$$C_d = \int_0^{y_w} C_d{}' dy \tag{2.16}$$

where y_w is the height or length of the wake. Through the data obtained, total pressure losses were observed particularly at higher Mach numbers as was expected due to compressibility effects. Hence, the difference between the stagnation pressure measurements obtained outside of the wake region were averaged and the

difference was found between the averaged freestream stagnation pressure recorded for the wind tunnel. This difference was then added to each total pressure value to offset the averaged total pressure loss. The integration was then performed from one wake-tail end to the other. The wake tails were determined by the point where the ratio between the local stagnation pressure and the freestream stagnation pressure decreased to a value lower than 1. Once the wake region was identified, the integration was performed using the trapezoidal rule at the midpoints between two adjacent data points.

2.3.3 Data Acquisition System

The data for the tunnel conditions, airfoil-static pressure measurements, and wake pressure measurements were taken using a custom software written in the National Instruments 2016 LabView programming environment. This software was run on an HP Z230 Workstation with an Intel® Xeon® CPU E3-1240 v3, measuring clock speed of 3.4 GHz, 8 GB of RAM, and a Windows 10 Pro 64-bit operating system. This software provided the user with a graphical interface to calibrate, tare, or initialize different data acquisition components, and take data points individually or simultaneously.

Acquisition of experimental values was divided into three main components. The first component included acquisition of the general tunnel parameters including total, stagnation, and dynamic pressures, total and static temperatures, speed of sound, freestream velocity, and Mach number of the freestream flow recorded at a frequency of 2 Hz. The pressure values were obtained using the pressure transducers discussed in Section 2.1 interfaced with the software through a National Instruments NI USB-6009 Multifunction I/O Device using analog channels which was connected to the computer using a USB cable. The pressure transducers were properly calibrated based on curves provided by the manufacturer. The total temperature measurements obtained through the thermocouple, also described in Section 2.1, which interfaced directly with the software through a USB connection. The second data acquisition component consisted of the pressure measurements. Two variants of the code existed depending on if data were taken for surface or wake pressure measurements. The devices used for obtaining these data values interfaced with the computer via an Ethernet connection using Protocol Version 4 (TCP/IPv4). Their operation and acquisition rates are discussed in Section 2.3.1. The third acquisition component was the mass flow system for the suction cases of the Griffith airfoil. These data values were obtained via an RS-232 communication protocol between the mass flow meter and the computer using an RS-232-to-USB adapter. Volumetric flow rates were then

obtained at a frequency of 35 Hz. The software provided the option to record measurement sets individually or all together for surface-pressure and wake-pressure runs separately. When performing PIV, Schlieren, and flow visualization experiments, only tunnel conditions and mass flow (if necessary) data were obtained.

In addition, the stepper motors discussed in Section 2.1 used to set the position of the suction plenum flaps and model angle of attack were controlled via this software. For this, an RS-232 communication protocol was used with the motors interfacing with the computer via an RS-232-to-USB adapter. The software allowed for their initialization when initially turned on to set the holding torque as well as to send position commands in degrees relative to their previous position. All commands to set specific angles in the suction flaps and the angle of attack of the airfoil model were executed before commencing operation of the wind tunnel during experimental runs.

2.3.4 Wind Tunnel Corrections

Test sections in wind tunnels are constrained by physical and finite boundaries which inherently prevent absolute atmospheric conditions to be replicated. Furthermore, the solid boundaries impose three-dimensional influences in the flow, which become more predominant when the test article's aspect ratio is small. This influence poses a constraint when considering airfoils, since their performance is representative of a two-dimensional flow. In addition, test sections in transonic wind tunnels are further exposed to artificial flow influences due to compressibility effects. For example, in order to mitigate shock reflections from the tunnel walls, test sections are usually fitted with porous wall boundaries as discussed in Section 2.1. Depending on the local pressure gradient across the porous wall boundary, flow might be entering or leaving the test section. This artificial velocity component, depending on its strength, could significantly affect the local streamline curvature as has been observed during experiments. Therefore, wind tunnel corrections are used to compensate for the effects introduced by the physical constraints present in wind tunnels.

Wind tunnel corrections were applied to all acquired data to account individually for the influence of top and bottom porous walls, sidewall interference, and displacement of the effective Pitot center in the wake traverse. The top and bottom porous wall corrections were based on the formulation presented by Mokry et al. [33] for two-dimensional transonic wind tunnel sections using empirically-based wall interference factors. This approach accounted for corrections in the airfoil C_p distributions, aerodynamic coefficients, freestream Mach number, and aerodynamic angle of attack. The sidewall interference correction was per-

formed based on Sewall's transonic correction for Barnwell's method, which only affects the freestream Mach number [34]. Finally, the C_d was corrected for the displacement of the effective Pitot center in the wake traverse using an empirical integral factor approach presented by Pankhurst [32].

Corrections considering the factors discussed above were executed in the following way. The correction considering C_d was performed individually and independent of the other corrections. The other aerodynamic coefficients (C_l and C_m) as well as the Mach number and angle of attack were first corrected considering the porous-wall interference. The sidewall influence was then considered, with it only affecting the Mach number. With the new Mach number and known speed of sound, the local C_p was updated along with corrected values of C_l and C_m. Since the corrections for porous walls and sidewall interferences considered the aerodynamic coefficients, the updated C_l and C_m values were used again to obtain final versions of C_l, C_m, M, and α. The following subsections describe in brief detail the formulation of each correction.

Porous-Wall Influence Correction

For an in-depth analysis of the theoretical formulation of the classical porous-slotted wall theory from which the corrections are derived, the interested reader is referred to Reference [33] after Mokry et al. However, a brief overview of the correction formulation, considerations, and important wind-tunnel-dependent parameters are presented within this section. The porous-wall correction is based on a theoretical formulation of an infinite test section between two parallel walls on which a porous wall boundary condition is enforced alongside Prandtl's concept of wall interference [33].

It is stated that in most practical cases for two-dimensional airfoils, consideration of velocity (blockage), incidence, velocity gradient, and streamline curvature corrections is sufficient [33]. Hence, the following expressions are given for each respective interference factor for perforated walls to be evaluated at the leading-edge location of the airfoil model. The wake blockage factor ϵ_w is defined as:

$$\epsilon_W = \frac{1}{2}\frac{\sigma}{\beta^2 h}\Omega_w \tag{2.17}$$

where σ is defined as the source strength, β is the Prandtl-Glauert compresssibility correction factor, h is the wind tunnel test-section height, and Ω_W is the wake blockage ratio. These parameters are defined in the following equations:

$$\sigma = \frac{1}{2}\, cC_{d_w} \tag{2.18}$$

$$\beta = \sqrt{1 - {M_\infty}^2} \tag{2.19}$$

$$\Omega_W = 2B_1\left(\frac{\tau}{2}\right) \tag{2.20}$$

where c is the airfoil model chord length, C_{d_w} is the wake drag coefficient, and M_∞ is the freestream Mach number. In Eq. 2.20, the first Bernoulli polynomial B_1 and τ are defined as:

$$B_1\left(T^*\right) = T^* - \frac{1}{2} \tag{2.21}$$

$$\tau = \frac{2}{\pi}\,\mathrm{atan}\left(\frac{P^*}{\beta}\right) \tag{2.22}$$

In Eq. 2.21, T^* holds the place of a variable, and in Eq. 2.22 is a porosity factor for perforated walls defined as:

$$P^* = \beta \tan\left(\frac{\pi}{2}\, OAR\right) \tag{2.23}$$

where OAR is the open-area ratio of the test section porous walls. The solid blockage factor ϵ_S is defined as:

$$\epsilon_S = \frac{1}{6}\,\frac{\mu\pi}{\beta^3 h^2}\Omega_S \tag{2.24}$$

where μ is a doublet strength and Ω_S is the solid blockage ratio defined in the following way:

$$\mu = c^2 A \tag{2.25}$$

$$\Omega_S = 6B_2\left(\frac{\tau}{2}\right) \tag{2.26}$$

The term A in Eq. 2.25 is the cross-sectional area of the airfoil nondimensionalized by c^2, and B_2 is the second Bernoulli polynomial defined as:

$$B_2\left(T^*\right) = T^{*^2} - T^* + \frac{1}{6} \tag{2.27}$$

The upwash factor δ_0 and streamline factor δ_1 were defined as follows:

$$\delta_0 = -\frac{1}{2} B_1\left(\frac{1+\tau}{2}\right) \tag{2.28}$$

$$\delta_1 = -\frac{\pi}{2} B_2\left(\frac{1+\tau}{2}\right) \tag{2.29}$$

The following nondimensional parameters were defined for velocity u_W and incidence v_W corrections which were evaluated at the leading-edge location of the model:

$$u_W = \epsilon_W + \epsilon_S \tag{2.30}$$

$$v_W = \frac{2\gamma}{h}\delta_0 + \frac{2\omega}{\beta h^2}\delta_1 \tag{2.31}$$

where ω is the doublet strength in the y direction (vertical) defined as:

$$\omega = \frac{1}{2} c^2 C_{m_{LE}} \tag{2.32}$$

where in Eq. 2.32, $C_{m_{LE}}$ is the airfoil pitching moment coefficient about the leading-edge location.

The angle-of-attack correction $\Delta\alpha$ (given in radians) and Mach number correction ΔM_∞ due to the influence of the porous wall boundaries were then calculated using the following relationships.

$$\Delta\alpha = v_W \tag{2.33}$$

$$\Delta M_\infty = \left(1 + \frac{\kappa - 1}{2} {M_\infty}^2\right) M_\infty u_W \tag{2.34}$$

Sidewall Influence Correction

The influence of sidewall interference has a superior impact in most transonic experiments for two main reasons. First, due to the non-linear characteristics in transonic flows, the sidewall influence on the airfoil model results more intricate to characterize and correct. Furthermore, due to the general nature of smaller test sections, as happens to be the case, airfoil models are typically designed with higher chords in order to reach higher Reynolds numbers [35]. For a fixed span, these longer chords result in lower aspect ratios for which sidewall influences become predominant, affecting the two-dimensionality of the flow seen by the airfoil.

The method used in this study to correct for sidewall influences is based on Sewall's transonic correction for Barnwell's method, which affects only the freestream Mach number. For a detailed overview of the formulation of the correction method the reader is referred to Reference [34] after Sewall. However, a general overview is presented herein. The formulation is derived from an isentropic steady flow assumption considering small perturbation theory. An expression for the corrected Mach number ($M_{\infty c}$) after a first-order Taylor series approximation is given by:

$$M_{\infty c} = M_\infty - \left[\frac{3M_\infty}{2 + {M_\infty}^2} \left(2 + \frac{1}{H} - {M_\infty}^2 \right) \frac{\delta^*}{b_0} \right] \tag{2.35}$$

where M_∞ is the freestream Mach number, H is the shape factor of the sidewall boundary layer, δ^* is the displacement thickness of the boundary layer on the sidewall, and b_0 is the airfoil semi span. The following equations show the calculation for displacement thickness and shape factor of the boundary layer for a flat plate which would be the case of the side wall:

$$\delta^* = \frac{1.7208x}{\sqrt{Re_x}} \tag{2.36}$$

$$H = \frac{\delta^*}{\theta} \tag{2.37}$$

where x is the location of the model in the freestream direction, Re_x is the Reynolds number at the corresponding x location, and θ is the boundary-layer momentum thickness defined in Eq. (2.38) for a flat plate.

$$\theta = \frac{0.664x}{\sqrt{Re_x}} \tag{2.38}$$

Displacement of Effective Pitot Center Correction

To calculate C_d, pressure measurements were obtained using a Pitot-static wake traverse as discussed in Section 2.3.2 at the same geometric conditions for which aerodynamic coefficients and flow parameters have been corrected for porous walls and sidewall influences. However, C_d values were only corrected for the local displacement of the effective Pitot center dependent on Mach number which results from the transverse velocity gradient across the wake. Since the Pitot-static probe was located in the center line of the test section and far away from the top and bottom walls where wall influences were observed to be dominant, no further correction was applied to C_d.

The C_d correction presented by Pankhurst is defined as follows [32]:

$$\Delta C_d = 0.36\frac{\delta}{c}\, {C_{d_{max}}}' \tag{2.39}$$

where δ is the external thickness of the Pitot-static probe, c is the chord of the airfoil model, and ${C_{d_{max}}}'$ is the maximum $C_d{}'$ obtained when using Eq. (2.15) for the calculation of C_d.

2.4 Particle Image Velocimetry (PIV) Tests

Particle Image Velocimetry, or PIV, is a non-intrusive experimental technique that is used to determine the instantaneous velocity fields by measuring the velocity of small tracer particles that accurately track the motion of the fluid [36]. These velocity measurements are acquired by artificially seeding the flow with particles, such as smoke, illuminating the field of view with a high-intensity light source, and imaging the displacement of these particles across two frames during a small time interval. The displacement of these particles are then correlated to instantaneous velocity vectors in the flow field.

In order to characterize the effect of suction in the momentum deficit across the wake, PIV experiments were performed to obtain the mean velocity flow field for each of the different test conditions in the wake region. In order to seed the flow, a ViCount Compact 1300 Standard Variant (1.1kW) smoke generator manufactured by Concept Systems, LTD was used. This system outputs smoke particles with a mass median

size of 0.2 – 0.3 micron, which was found ideal given the small area of interest of the experiment. A laser sheet was produced using a dual-pulsed Quantel Evergreen 200 mJ Nd:YAG PIV laser coupled to a set of beamforming optics. The camera used to obtain the images was an LaVision Imager sCMOS camera in conjunction with a Nikon AF MICRO NIKKOR 60mm lens. The camera was placed perpendicular to the plane of interest aproximately 10" away from the center of the model. The image frame had the trailing edge of the airfoil centered near the middle of the frame, capturing approximately 30% of the entire airfoil (including the suction slot) as well as majority of the wake. In order to prevent reflections from the laser, the airfoil model was covered with matte-black contact paper. After application of the contact paper, the model was inspected to ensure the surface remained smooth and free of bubbles inside the adhesive or other external contamination. An image of the PIV setup in the transonic wind tunnel can be seen in Fig. 2.8.

The data acquisition was performed using the LaVision DaVis 8.3 software installed in a RedBarn HPC. This computer had an Intel® Xeon® CPU ES-1650 v3, measuring clock speed of 3.5 GHz, 32 GB of RAM, and was run using a Windows 7 Professional 64-bit operating system. The images pairs were acquired at a frequency 10Hz and the resolution of the camera was set to 2560×2160 pixels. The time step between image pairs was changed for each Mach number and set to 2.4, 1.7, 1.4, 1.1, and 0.95 μs at corresponding Mach numbers of 0.3, 0.4, 0.5, 0.6, and 0.7. This approached allowed the reliability of the cross-correlation process used in the calculation of the vector fields to be retained across all Mach numbers. A total of 300 image pairs were acquired for each test condition.

Processing was later performed also using the LaVision DaVis software version 8.3 to calculate vector fields from the acquired particle images. A total of 5 passes were performed to each raw image pair; the first two with a window size of 128×128 pixels with 50% overlap and the remaining 3 with a window size of 24×24 pixels with 75% overlap.

2.5 Schlieren Imaging Tests

Schlieren imaging is an optical diagnostic technique widely used during high-speed wind tunnel tests to observe flow field details associated with density gradients, such as boundary layers, shock waves, flow expansions, flow disturbances, and interactions thereof [37]. This technique relies on the physical principle that light rays are refracted upon encountering a density gradient in a continuous medium. These refracted light rays are then observed as a change in the color gradient of the focused monochromatic image. Tradi-

tionally, a Schlieren experimental setup consist of two parabolic mirrors. A light source, commonly an LED emitter, is oriented towards one of the mirrors at a distance of its focal length. The reflected light then results in a collimated light source that is intended to pass through the medium and object of interest. The refracted light rays due to density gradients will then reflect across the second mirror. What distinguishes Schlieren from Shadowgraph imaging is the placement of a knife edge or slit at the focal point of the second mirror to block a certain amount of light [38]. This allows a more noticeable color gradient to be created between the refracted and non-refracted light rays by capturing the first derivative of the density gradient whereas shadowgraphy only captures the second derivative [38]. This approach renders the Schlieren technique to be more sensitive to weaker disturbances at a cost of greater illumination based on the application [38]. For instance, regions in the image will appear darker or brighter depending on whether the original light rays were refracted towards or away from the knife edge. Hence, depending on the location of the knife edge on a fixed setup, shocks will appear darker or brighter than the rest of the undisturbed flow field.

Due to the inherent limitations posed by the test facility in which the experimental investigation was being conducted, a two-mirror Schlieren setup could not be implemented. Hence, a one-mirror approach was used under the following considerations. For this setup, the light source was placed at a location of two focal lengths from the mirror, passing through the test section. The two-focal lengths offset allowed for the reflected light rays to focus again at the location of the light source, where the knife edge would be placed. Since the actual reflected light rays would have to be focused at a slight offset from the light source, interference in the Schlieren image from overlaying rays would occur. This interference was noticed by the double presence of shock structures which were offset by approximately the sine of the angle at the focused location in the test section. To avoid this, a beam splitter was incorporated in the setup used as seen in Fig. 2.9. With this configuration, the light source travels through the beam-splitter cube and then through the test section. The light rays then get reflected at the mirror and are turned 90° where the knife edge was located at the two-focal length location, followed by a subsequent high-speed camera to capture the images.

The camera used to acquire the Schlieren images was a Photron Mini AX200 high-speed camera coupled with a Nikon AF NIKKOR 70-300mm zoom lens. Data acquisition was performed at a rate of 6 kHz with resolution of 1024x592 pixels. The image window captured approximately 32% of the airfoil from the trailing edge. It was ensured that the location where the pressure recovery would exceed that of the critical C_p calculated in Section 3.3 was within the field of view across all test conditions to appropriately capture

the resulting shock structures. The Schlieren experimental setup in the transonic wind tunnel is seen in Fig. 2.10

Acquisition of the Schlieren images was performed using the computer used for PIV data acquisition discussed in Section 2.4. The FASTCAM Viewer (PFV) software version 3.6.9.1 was used to interface with the Photron camera. This approach allowed to directly control the settings such as window size and acquisition rate, as well as to collect data.

Characterization of the oscillatory behavior in the transonic shocks was performed using a power spectral density (PSD) analysis. This approach considers the distribution of energy in the frequency domain to determine the relevant frequency scales of a periodic measurement or signal [39]. It represents the rate of change of mean square value with frequency for a stationary data set; hence, the integrated amplitude under the PSD function over all frequencies will be the total mean square value of the data. Similarly, the partial area under the PSD function between two frequencies represents the mean square value of the data set associated with a frequency range [40]. A fast Fourier transform (FFT) method was used to obtain the discrete Fourier transform (DFT), which was then used to compute the PSD, as discussed by Bendat and Piersol [40].

For the PSD to have an acceptable resolution in order to better determine the dominant frequencies in the oscillatory process, enough data points should be provided when performing the FFT. For this, an ensemble of 5 data sets each containing 18,886 images were obtained for each test condition of interest described in Section 2.7. Pixel intensities were tracked at two vertical locations at the averaged shock location above the upper surface of the airfoil. PSDs were performed on each individual pixel-location data ensembles for which excellent agreement was found. Hence, only the location closes to the airfoil surface located at $y = 0.1c$ above the airfoil chordline at the $x = 0.82c$ location of the airfoil was used for analysis. Finally, the FFT was performed using 5 realizations for each data ensemble average. This realizations parameter determines the frequency resolution of the spectrum based on the sampling frequency and total number of samples. Appendix A shows the general formulation used in the calculation of the PSDs for this study.

2.6 Flow Visualization Tests

Since boundary-layer transition is of immense concern in the study of laminar flow airfoils, fluorescent, surface-oil flow visualization diagnostics were performed to determine the laminar, transitional, and tur-

bulent regions of the boundary layer. This commonly used experimental technique in experimental aerodynamics, which has been applied in transonic flow conditions [41, 42], allows the transition behavior in airfoils to be qualitatively characterized through the different shear patterns of laminar and turbulent boundary layers. For instance, a turbulent boundary layer is characterized by having greater shear than a laminar boundary layer and as such will produce larger displacements of oil which can be observed by a fluorescent intensity difference on the airfoil surface.

In preparation for the flow visualization experiments, the airfoil test model was painted in a matte-black finish which allowed the gradients in the fluorescent light intensity to be better observed. A thin coat of 10W-30 motor oil was initially applied using a precision cloth to fill imperfections and gaps in the paint finish. This ensured that the fluorescent oil would flow smoothly over the surface and not transition prematurely due to surface impurities. The oil mixture for flow visualization consisted of a 1:1 mixing ratio of STP high-viscosity oil additive combined with 85W-140 motor oil. This higher viscosity ensured that the oil would not flow away from the model which would prevent the observation of relevant features in the presence of high dynamic pressures and Mach numbers. A few drops of Kent-Moore 28431-1 fluorescent dye were added to this oil mixture which was then applied to the top surface of the airfoil model using a fine brush. To excite and visualize the fluorescent oil, the test section was fitted with two arrays of ultraviolet 400 nm wavelength LED lights manufactured by PlashLights. An image of the airfoil test model in the test section configured for for flow visualization experiments is seen in Fig. 2.11 prior to an experimental run.

After the fluorescent-oil mixture had been applied, the wind tunnel was set to the appropriate Mach number. The oil was allowed to displace for approximately 3 minutes, at which the flow patterns were observed to remain consistent. Images of the airfoil surface were taken from the right side of the test section using a Nikon D100 digital SLR camera mounted on a tripod as can be seen in Fig. 2.12. The exposure time for this camera was adjusted accordingly to ensure that all relevant surface-flow features were captured in the images. After each experimental run, excess oil was removed and the surface was recoated for testing under different conditions. Since the images were taken from the right side of the test section, the surface of the airfoil could not be directly analyzed in a two-dimensional plane. This required further processing of the images using Adobe Photoshop to extract the planar representation of the airfoil. It was ensured through different reference points that the dimensions of the modified planar surface images were consistent with that of the airfoil to properly identify important locations regarding the flow behavior.

2.7 Test Conditions

The aerodynamic performance aspect of the investigation encompassed a Mach number range from 0.3 to 0.7 varying by 0.1 intervals, and an angle-of-attack range varying from -2° to 2° varying by 1° degree intervals. This summed up to a total of 25 test cases of interest based on the angle-of-attack and Mach number combinations for each airfoil configuration (50 cases for the Griffith airfoil considering suction and no-suction configurations and 25 cases for the RAE 2822 airfoil). Mach numbers for all test conditions were controlled to within 4.5%. The Reynolds number (Re) for each test condition considering the mean laboratory temperature of 70°F and 6" chord of both experimental models was calculated using the following equation:

$$Re = \frac{\rho_\infty V_\infty c}{\mu_{air}} \tag{2.40}$$

where ρ_∞ is the freestream density, V_∞ is the freestream velocity, c the airfoil model chord, and μ_{air} is the dynamic viscosity of air. The dynamic viscosity term for air was calculated based on the ambient temperature using Sutherland's law which is defined as follows:

$$\mu_{air} = \mu_0 \left(\frac{T_1{}^*}{T_0{}^*}\right)^{3/2} \left(\frac{T_0{}^* + S}{T_1{}^* + S}\right) \tag{2.41}$$

where T^* is total temperature, S is a constant given to be 110.4 K, and the subscripts 0 and 1 indicate conditions at a reference pressure and temperature (dependent on S) and the actual test conditions, respectively. The Re values calculated are tabulated for each corresponding Mach number in Table 2.1.

Suction requirements for the Griffith airfoil were determined based on the recommended suction parameter of V_s/V_∞ = 6.5% in Reference [21]. Initially, a sensitivity study was performed in order to understand the influence of the suction amplitude on the pressure distribution about the airfoil for values above the recommended parameter. Suction was varied from V_s/V_∞ = 6.5% to 8.5% in increments of 0.5% of the suction parameter at Mach numbers of 0.3 and 0.7. No significant difference or trend was observed as the suction was varied for both cases. The observations of this study were found to be in agreement with References [21] and [24], where the suction velocity of 6.5% of the freestream was established based on the minimum suction requirement for which no further substantial drag reduction was found during the airfoil design process. Based on the recommended 6.5% suction parameter, the target suction requirements

based on the Mach number were calculated in terms of volumetric flow rate using the area of the slot, isentropic flow relations, and standard temperature conditions in the laboratory. These suction requirements are tabulated as well in Table 2.1. The volumetric flow rates recorded for all test cases were controlled to within 3.65% of the target suction flow rate and within 3.55% of the actual suction requirement considering temperature variations.

Table 2.1: *Re* and volumetric flow rate for the Griffith airfoil based on corresponding Mach number.

Mach Number (M)	$Re(10^6)$	Flow Rate (LPM)
0.3	1.02	467.2
0.4	1.32	622.9
0.5	1.58	778.6
0.6	1.80	934.3
0.7	1.98	1090.0

PIV, Schlieren, and flow visualization data were only taken for the Griffith airfoil and not the RAE 2822. PIV images in the trailing edge wake region were taken for all Mach numbers and angles of attack for both suction and no-suction conditions. Schlieren and flow visualization data acquisition were only performed at the design Mach number of $M = 0.7$ at all angles of attack, again for both suction and no-suction conditions.

2.8 Figures

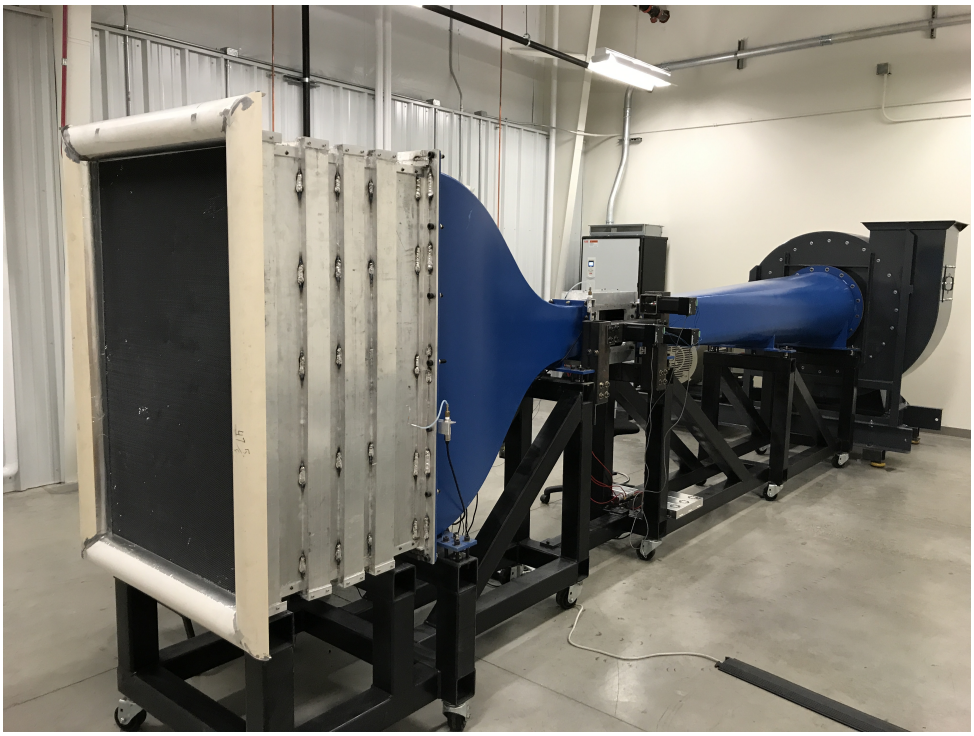

Figure 2.1: Transonic Wind Tunnel Facility at UIUC.

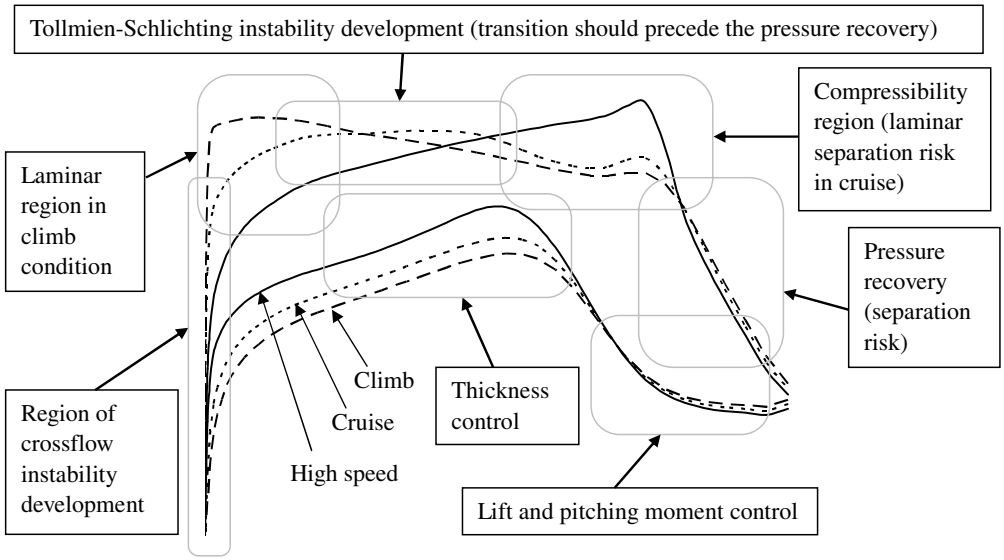

Figure 2.2: Notional C_p distribution for a transonic airfoil at three different design conditions [30].

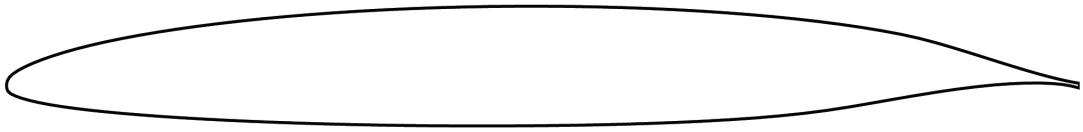

Figure 2.3: Griffith-type transonic, laminar-flow airfoil profile.

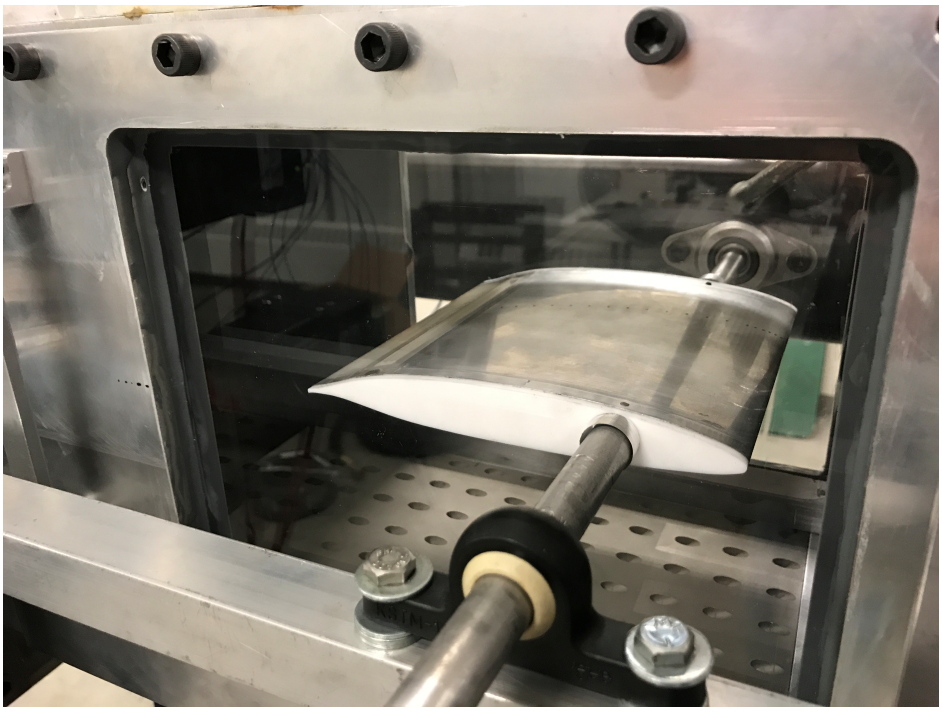

Figure 2.4: Griffith-type transonic, laminar-flow airfoil seen inside the wind tunnel test section.

Figure 2.5: RAE 2822 airfoil profile modified with finite trailing edge.

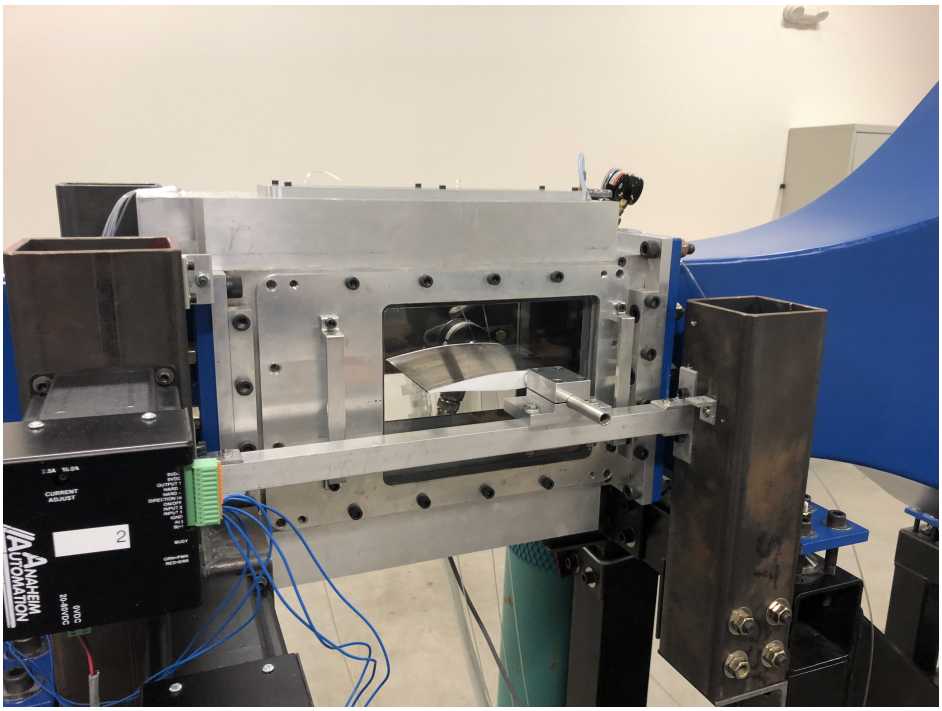

Figure 2.6: RAE 2822 airfoil seen inside the wind tunnel test section.

Figure 2.7: Wake traverse system mounted in wind tunnel for wake pressure acquisition.

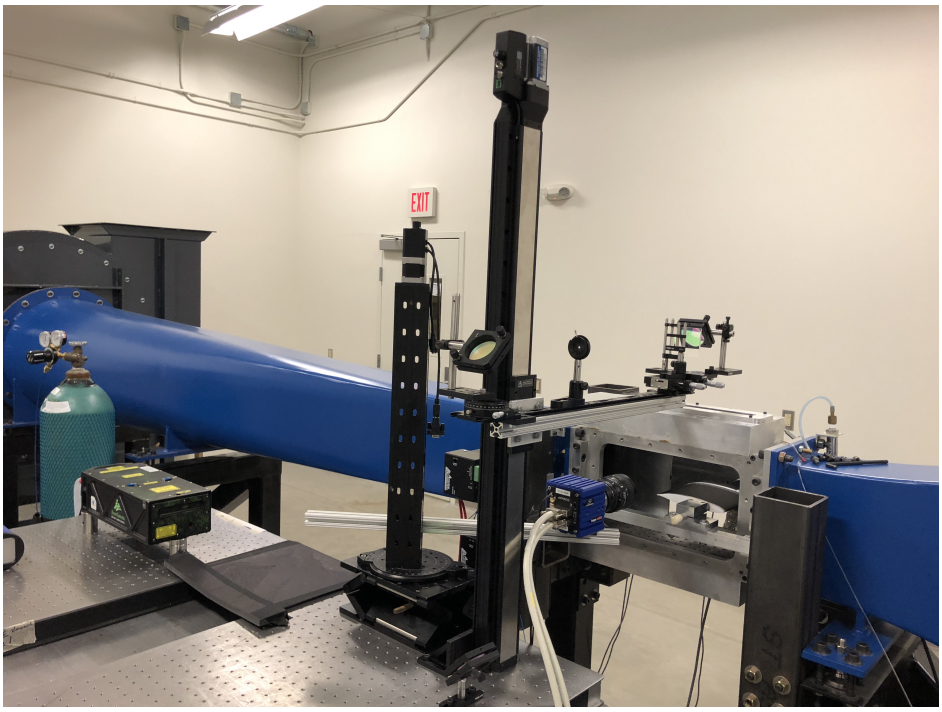

Figure 2.8: PIV setup in transonic wind tunnel.

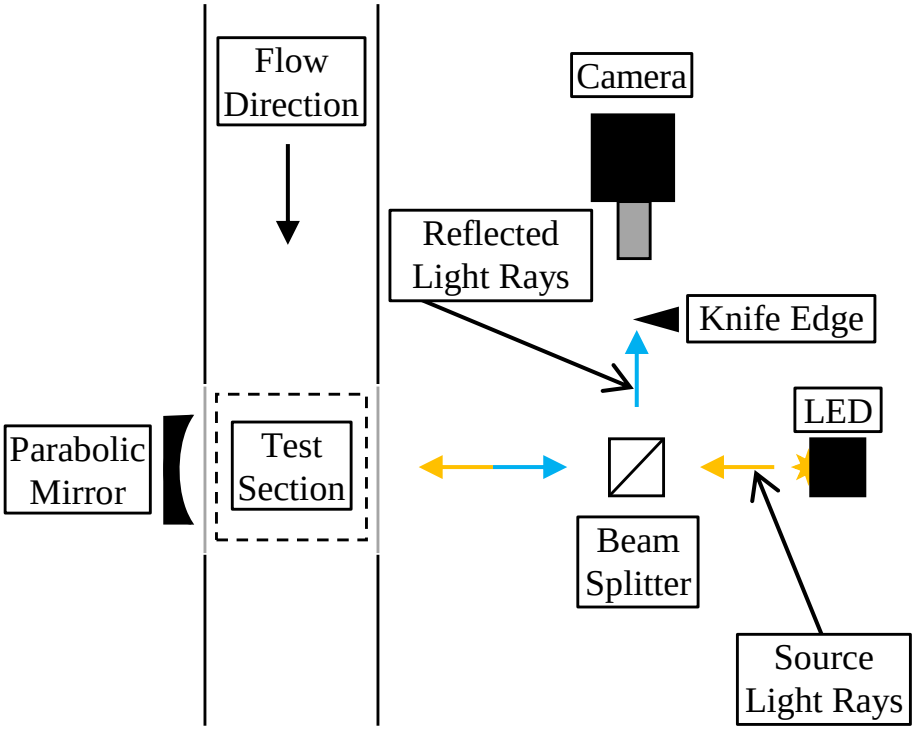

Figure 2.9: One-mirror Schlieren setup schematic.

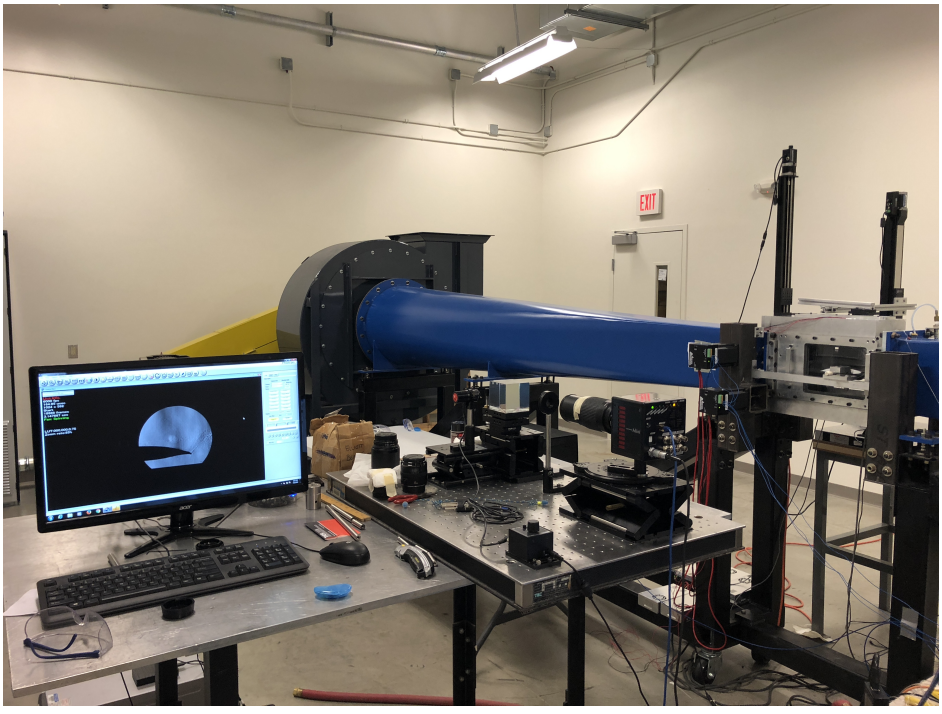

Figure 2.10: Experimental Schlieren imaging setup in the transonic wind tunnel.

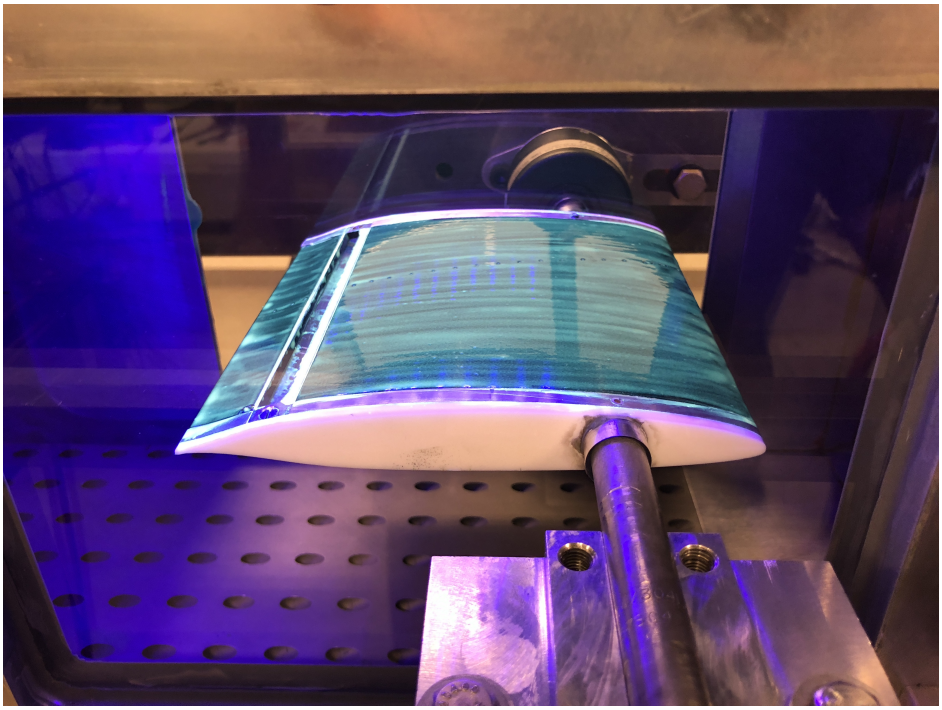

Figure 2.11: Griffith airfoil in suction configuration setup prior to a flow visualization run.

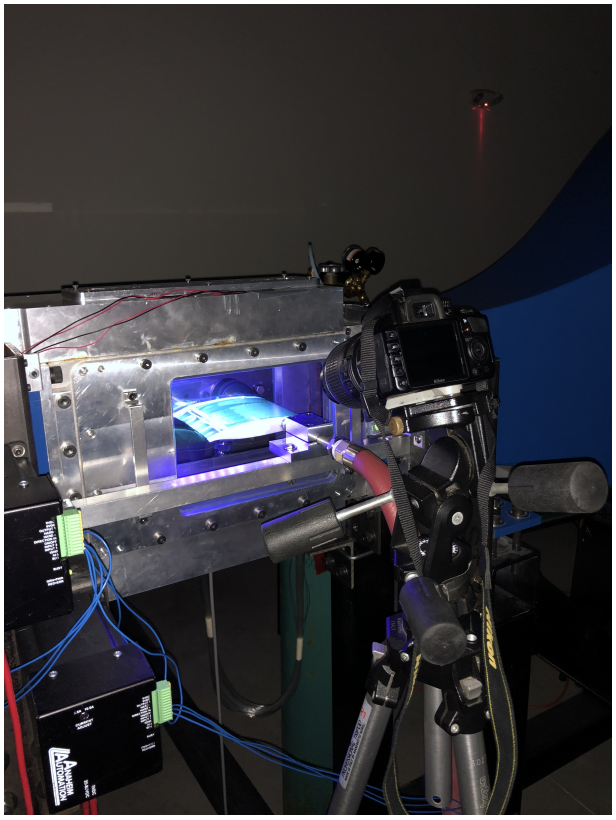

Figure 2.12: Flow visualization image recording setup in transonic wind tunnel.

Chapter 3

Results and Discussion

This section presents the data obtained through a variety of experimental techniques for the Griffith-type transonic, laminar-flow airfoil used in this investigation. The data is consistently presented for both suction and no-suction conditions to highlight the effect of boundary-layer suction on the airfoil's performance. Furthermore, aerodynamic performance data for an RAE 2822 transonic airfoil is presented in an effort to show performance benefits that can be obtained from the Griffith-type airfoil concept by comparing it to a well-known canonical case at the same freestream conditions.

Airfoil C_p distributions are presented for all Mach numbers across an angle-of-attack range from -2° to 2°, individually considering the suction and no-suction conditions. The distributions are also plotted together for all Mach numbers at each angle of attack to allow for direct comparison. In addition, a plot containing all angles of attack at the design Mach number of $M = 0.7$ is presented to assist in identifying angle-of-attack influences in the pressure distributions at the design Mach number. The pressure distributions were then used to calculate aerodynamic performance parameters which include aerodynamic polars in the form of C_l vs. C_d, C_l vs. α, and C_m vs. α curves. Contour plots obtained from the PIV data, showing the averaged velocity flow field near the trailing-edge region of the airfoil under suction and no-suction conditions are also presented for all angle-of-attack conditions at freestream Mach numbers of 0.3, 0.4, 0.5, 0.6, and 0.7, which further support the momentum loss alleviation produced by boundary-layer suction. Particular interest is given to the design condition of $\alpha = 0°$ and $M = 0.7$ for which an analysis in the wake velocity variation is provided. Schlieren and surface-oil flow visualization data are also presented, which when compared to trends observed in the C_p distributions, provide insights into the transonic shock and boundary-layer transition behavior in the presence of suction.

3.1 Pressure Distribution

The pressure distributions about the Griffith airfoil were obtained for both suction and no-suction conditions. For the no-suction conditions, the slot in the airfoil model was fitted with a cover plate having the same contour of the airfoil over the slot section. This was done to avoid air being pulled out from the plenum chamber in the absence of suction due to the lower pressures present across the upper surface of the airfoil, therefore providing an accurate representation of the airfoil geometry without suction being applied. For the suction conditions, a slot containing the $5\%c$ opening was fitted into the model to allow for suction to be applied across the boundary layer. Figures 3.1 to 3.30 show the C_p for both suction and no-suction conditions for individual Mach number and angle-of-attack configurations, as well as all Mach numbers for each angle-of-attack condition plotted together for comparison purposes. Figure 3.31 shows the C_p distributions for all angles of attack at the design Mach number of $M = 0.7$.

When considering all angle-of-attack and Mach number variations in the C_p distributions, a suction benefit can be observed across every test condition being predominant across the aft region of the upper surface of the airfoil. At the design angle of attack of $\alpha = 0°$ for Mach numbers of $0.3-0.6$ (Figs. 3.13 to 3.16 and 3.18), the suction-induced reductions in C_p can be identified beginning around the $x/c = 0.35 - 0.40$ location, while for the $M = 0.7$ case (Figs. 3.17 and 3.18), the difference in pressure from the no-suction case occurs further downstream near the $x/c = 0.55$ location. It is also noted in the C_p data set that for every angle-of-attack and Mach number condition tested that all suction conditions show a more aggressive pressure recovery. For the suction cases, the pressure values recorded immediately downstream of the x/c = 0.90 location after the suction slot are observed to be higher when compared to those for the no-suction cases. As a result, the overall pressure recovery at the trailing edge location is also higher for every test condition when compared to the no-suction cases. For the Mach 0.7 cases (Fig. 3.31), the difference between the suction and no-suction cases in the recovered trailing edge pressure coefficient is the greatest. This recovery is an indication of the performance benefit provided by the suction. By decreasing the momentum thickness in the boundary layer at the slot location the pressure is able to recover to a higher value over the same distance. In essence the suction moves the location of the unforced adverse pressure gradient recovery region farther downstream and reduces it, causing the aforementioned alleviation in momentum deficit and producing a viscous drag benefit [43].

The C_p distribution difference between suction and no-suction cases for each angle of attack is consistent

across Mach numbers between 0.3 to 0.6, and as previously mentioned influence in the pressure distribution is noticed well upstream of the slot location. The $M = 0.7$ cases (Fig. 3.31) are an exception where a more dramatic decrease in pressure is observed for the suction cases between approximately the $x/c = 0.60 - 0.90$ location and no influence in the C_p is observed upstream of this region. This behavior could be related to a transonic circulation effect. Due to the presence of a local supersonic region, local flow influences near the trailing edge cannot propagate upstream at the same velocity as in an incompressible flow, and hence do not have a first-order influence in the pressure characteristics of the airfoil upstream of the local shock. This limits the influence of suction for the $M = 0.7$ cases (where local supersonic regions were identified as discussed in Sections 3.3 and 3.4) to a smaller chordwise region further downstream when compared to the other Mach numbers tested. The magnitude of the C_p difference being greatest at the higher angles of attack is due to the fact that at these conditions the boundary layer over the upper surface of the airfoil experiences the strongest adverse pressure gradients across the pressure recovery region. As a result, suction has the most significant effect in reducing the boundary layer thickness and helping it recover across a stronger adverse pressure gradient. This could also be related to the behavior observed in Figs. 3.23 and 3.29 corresponding to α = -1° and α = -2° respectively at $M = 0.7$. At these low angle-of-attack conditions, the boundary layer over the upper surface is not subject to such strong adverse pressure gradients as those at the higher angles of attack. Consequently, the C_p magnitude differences observed are not as high and only influence approximately the $x/c = 0.75 - 0.90$ region. However, this shorter, yet stronger influence in the C_p as a result of suction results in a further-aft loading of the airfoil and a delay in the transonic shock location with a lower pressure rise across. The movement of the shock further downstream across the chord allows for the extension of laminar runs limited by shock-induced laminar separation bubbles for most test conditions, as was later confirmed through flow visualization and Schlieren experiments which are discussed in Sections 3.3 and 3.4, respectively.

Pressure distributions for the design Mach number of $M = 0.7$ with angle-of-attack variations are presented in Fig. 3.31. It can be seen from the angle-of-attack change that as α increases the airfoil becomes more evenly loaded across the chord and the initial pressure recovery location moves upstream, varying by approximately $5\%c$ between α = 2° and -2°. The pressure distribution plots also show consistency in the higher trailing-edge recovery C_p obtained for the suction cases when compared to the no-suction cases across all angles of attack for $M = 0.7$. As was previously mentioned, transonic shocks were found at M =

0.7 for all angle-of-attack cases; however, stronger shocks at the higher angles of attack can be identified in Fig. 3.31 where larger gradients are visible in the pressure recovery region across the upper surface near the airfoil trailing edge. For the no-suction pressure distributions at $\alpha = 1^\circ$ and 2°, the influence of transonic shocks can be seen as the static pressure increases abruptly starting near the $75\%c$ and $70\%c$ locations, respectively. For the $\alpha = 2^\circ$ case with suction applied the shock appears to be weaker than the no-suction case and moves farther downstream to $74\%c$. There is not a distinct shock-indicative pressure gradient that can be identified from the pressure distribution for the $\alpha = 1^\circ$ case with suction applied; in fact, the pressure distribution achieves a larger magnitude in the minimum C_p value than that of the $\alpha = 2^\circ$ case with a subsequent adverse pressure gradient region further downstream. Based on these observations, suction appears to have a beneficial effect in shock alleviation, in addition to the improved pressure recovery previously described. This observed decrease in pressure rise across the shock could imply possible wave drag reductions associated with the use of suction at local sonic regions of the airfoil when operating in the transonic regime.

3.2 Aerodynamic Performance

The performance of the Griffith airfoil was characterized through the calculation of aerodynamic coefficients using the airfoil-surface pressure measurements as well as the wake pressure measurements recorded for all test cases. The coefficients are plotted for all angle-of-attack conditions at every Mach number for both suction and no-suction cases. These plots allow the influence of suction to be identified in the performance characteristics of the airfoil directly. However, since this airfoil was not designed to operate without suction, the performance gain obtained through the comparison of suction and no-suction cases might not be entirely representative of benefits that could be achieved when compared to a canonical transonic airfoil. For this reason, drag polars obtained for an RAE 2822 transonic airfoil at the same test facility and experimental conditions are also presented as highlighted in Section 2.2.2. This comparison allows the reductions in the drag coefficient at similar lift coefficients to be compared between the airfoil of interest and a representative transonic airfoil commonly used in research investigations of this type.

In addition, the influence of suction in the momentum deficit alleviation in the wake region was characterized through PIV experiments as described in Section 2.4. Contour plots of the velocity flow field in the wake region produced by the airfoil were obtained for all suction and no-suction conditions to provide fur-

ther observations of flow-field influences associated with the drag reductions and lift-to-drag performance gains observed in the aerodynamic polars. Importance is given to the design condition of $\alpha = 0^\circ$ and $M = 0.7$ for which the direct relationship in the velocity difference in the wake due to the presence of suction is analyzed.

3.2.1 Aerodynamic Polars

The aerodynamic performance results produced by the airfoil at each condition are presented in Figs. 3.32 to 3.36 based on each particular Mach number. The difference in the lift-curve slope introduced between the suction and no-suction cases for each of the Mach numbers is negligible, meaning that the curve basically shifts by a constant difference in C_l while leaving the slope unchanged, based on qualitative observation in the data trend. Only does the lift-curve slope increase slightly as the Mach number increases as was expected due to compressibility factors. For all freestream Mach numbers, an increase in the airfoil C_l can be observed when suction is applied. The moment about the quarter-chord location also shows a consistent increase in magnitude across every Mach number condition under the influence of applied suction. This observation is produced due to the increased aft loading of the airfoil with suction as can be seen in the C_p distributions and is predominant for the $M = 0.7$ cases as discussed in Section 3.1.

Unlike the constant shift in lift coefficient observed between the suction and no-suction cases, the drag benefits when suction is applied are seen predominantly at the higher angles of attack. The case of $M = 0.3$ is an exception, as the magnitude of the drag benefit appears to be consistent across the entire angle-of-attack range. At the $\alpha = 0^\circ$ test conditions the drag decreases by 31.8%, 27.1%, 20.3%, 3.7%, and 10.7% at Mach numbers of 0.3, 0.4, 0.5, 0.6, and 0.7 respectively between the suction and no-suction conditions. Drag polars for an RAE 2822 canonical transonic airfoil model of the same chord and tested at the same wind tunnel facility and freestream conditions have been included in Figs. 3.32 to 3.36 as a means of comparison with the airfoil of interest. It is seen in Figs. 3.32 to 3.36 that at the design condition of $\alpha = 0^\circ$, the suction cases of the Griffith airfoil provide notable drag reductions which result in increases in the lift-to-drag ratio across all Mach numbers tested when compared to the no-suction and RAE 2822 cases.

An interesting case is seen at $M = 0.6$ in Fig. 3.35 where a maximum drag reduction of 20 counts is observed between the RAE 2822 and the suction condition at $\alpha = 2^\circ$ while concurrently displaying a net profile drag increase of 2 counts at $\alpha = -2^\circ$. However, the L/D ratio for this $\alpha = -2^\circ$ condition still sees

an increase of 13.09% providing an indication of improved aerodynamic performance due to suction even when the drag value is not substantially reduced at the higher Mach numbers. A similar trend is seen in Fig. 3.36 for M = 0.7 at α = -1° and -2° where the net profile drag increases of 3 and 2 counts respectively between suction and no-suction cases, and 7 and 4 counts respectively between suction and the RAE 2822 data are observed. However, when comparing the L/D, the suction conditions result in an increase of 1.96% for α = -1° and 37.39% for α = -2° when compared to no-suction. No benefits were obtained for α = -1° and -2° at M = 0.7 when compared to the RAE 2822 data, resulting in lower lift-to-drag ratios. This local drag increase is produced for these cases due to the fact that at the lower angles of attack the boundary layer on the lower surface experiences stronger pressure gradients when compared to higher angles of attack. Hence, the benefit of the suction being provided across the upper surface is not substantial enough to provide a net profile drag reduction.

3.2.2 Wake Velocity Flow Field

PIV data were acquired near the trailing edge of the airfoil in order to characterize the wake and survey the effect of suction across this region. Figures 3.37 to 3.46 display the averaged flow-field velocity in the wake region at the design angle of attack of 0° at the different Mach numbers tested for both suction and no-suction cases. Across every Mach number case, it can be observed that when suction is applied the wake region is associated with an increase in velocity magnitude. Figure 3.47 shows the wake velocity profile for the design condition of M = 0.7 and α = 0°, where a consistent increase in magnitude can be observed for the three chordwise locations shown, being greatest near the x/c = 1.10 region. Figure 3.48 presents the contour of the wake velocity difference between the suction and no-suction cases normalized by the freestream velocity for the same design Mach number and angle of attack. The normalized velocity difference in this contour plot is seen to be primarily constrained to the wake region, being strongest near the trailing edge and dissipating in intensity as it progresses downstream agreeing well with the observations in Fig. 3.47. A maximum velocity-difference ratio between the suction and no-suction conditions is observed at approximately 16% of V_∞ very near the the trailing edge. Based on observations from the wake measurements used to obtain the drag values in Section 3.2.1, suction does not have an effect in reducing the size of the wake but rather achieves higher stagnation pressure ratios (when compared to freestream conditions) which result in the higher velocities observed. This velocity increase in the wake is indicative of a reduced momentum deficit,

which can be related to the reductions in profile drag for every $\alpha = 0^\circ$ case, as observed in Figs. 3.32 to 3.36. Goldstein explains that this variation imposed on the wake due to suction occurs because the parts of the boundary layer that have lost the most momentum before the suction location area drawn inside the slot and do not appear in the wake with this loss of momentum [44]. When observing the aft upper surface region near the slot location in Figs. 3.37 to 3.46, it can also be seen that for the suction cases the velocity gradients have a more rapid and distinct change with streamwise distance, corresponding to the more aggressive recovery characteristics in the adverse pressure gradient regions from Fig. 3.18. This behavior, which can also be observed in Fig. 3.48 near the $x/c = 0.76$ location of the airfoil for the velocity difference contour plot at the design condition of $\alpha = 0^\circ$ and $M = 0.7$, is found to be predominant at higher Mach numbers based on qualitative observations from the PIV data.

3.3 Transition Characteristics

Understanding the transition characteristics of the airfoil-surface boundary layer is of high importance in the study of laminar flow airfoils since it is desirable to extend the laminar flow runs as far as possible across the surface with the intention of reducing the viscous drag component. Therefore, flow visualization diagnostics were performed on this airfoil at the design Mach number of 0.7 at varying angles of attack. Figures 3.49 to 3.58 present the no-suction and suction cases for all angles of attack tested.

As was mentioned before in Section 3.1, based on the C_p distributions it was identified that the suction did not have a significant influence on the airfoil pressure distributions farther upstream than approximately x/c = 0.35-0.55 at the design angle of attack of $\alpha = 0^\circ$. From Fig. 3.51, corresponding to $\alpha = 0^\circ$ with no-suction, a laminar flow run indicated in region "I" is observed to extend to around $0.685c$ followed by a shock-induced laminar separation bubble indicated by region "II" which then reattaches as a turbulent boundary layer in region "III". Designation of these three regions was confirmed by experimental observation of the surface-oil flow patterns, where the presence of stagnant flow in region "II" was recognized in a similar way that has been presented in References [41, 42]. This extensive region of laminar flow is produced even in the absence of suction due to the low-Reynolds number constraint in the experimental facility, and it persists across region "I" until interacting with the shock. A similar trend is also observed at every other angle of attack for the no-suction condition (Figs. 3.49, 3.50, 3.52 and 3.53) where the laminar flow in this low-Reynolds number test condition is shock limited. At higher Reynolds numbers, similar to those

of commercial transport aircraft where the boundary layer is foreseen to transition well upstream before the transonic shock, the increase in the magnitude and extent of the favorable pressure gradient could aid in the elongation of the laminar boundary layer region further downstream while still transitioning before the shock. As a secondary effect, this would eliminate the undesirable shock-induced laminar separation bubble which could further augment the drag benefit.

It is observed that for every case in Figs. 3.49 to 3.58 the presence of a shock is indicated by a discrete line of oil accumulation on the airfoil surface. A $C_{p,crit}$ value of -0.78 was calculated using isentropic flow relations at a freestream Mach number of 0.7 in order to identify the local sonic regions in the flow. Every case in the C_p distributions presented in Fig. 3.31 corresponding to a Mach number of 0.7 has sonic regions that precede the suction location, where laminar flow runs are still visible in the flow visualization images (Figs. 3.49 to 3.58). Hence, the laminar boundary layer does not carry enough momentum at the onset of pressure recovery to remain attached, leading to the shock-induced laminar separation at the end of the supersonic region, as identified by Cella et al [30] and highlighted in Fig. 2.2. It is identified by Cella that transition should precede the pressure recovery region during the T-S instability development in order to avoid laminar separation [30]. As seen also for every angle-of-attack case in Fig. 3.31, there is a significant favorable pressure gradient across the upper surface of the airfoil up to the pressure recovery point leading to increased stability of the boundary layer [45]. This effect prevents transition prior to the visible separation location on the airfoil model. Nevertheless, it is noticed that for the no-suction cases in Figs. 3.49 to 3.53, the onset of the laminar separation bubble moves further downstream by approximately $0.02c$ as the angle of attack is decreased by increments of 1° followed by a turbulent transition and reattachment region at approximately $0.77c$. The streamwise length of the laminar separation bubble region, however, is reduced with the turbulent reattachment region being fairly consistent. The laminar flow runs being limited by the shock-induced laminar separation bubble provides insight on the importance that transition before the shock can have in preventing laminar separation at transonic speeds, which can otherwise significantly degrade drag benefits.

Figures 3.54 to 3.58 show the flow visualization images for the same aforementioned cases with suction applied. It is observed that the effect of suction delays the shock location initially at the higher angles of attack as seen in Fig. 3.59, which displays a summary of shock positions observed in the flow visualization experiments with and without suction applied. The shock location remains fairly constant for the suction

cases, being further upstream than the no-suction condition at the lower angles of attack. This consistent shock location across the different angles of attack is related to an increase in the stability of the shock with suction applied, as discussed in Section 3.4. The size of the stagnant-flow region corresponding to the laminar shock-induced separation bubbles in Figs. 3.54 to 3.56 is fairly consistent with those in Figs. 3.49 to 3.51 for each corresponding angle of attack ranging between $\alpha = 2^\circ - 0^\circ$. Only does the laminar separation bubble move downstream with suction applied, as the suction application is unable to reattach the flow sooner. The laminar separation bubble produces a shear-layer interaction between the separated laminar boundary layer and the external flow, which through the propagation of vortical structures originating from Kelvin-Helmholtz (K-H) instabilities, transition occurs and the flow reattaches due to the additional momentum in the now turbulent boundary layer [46, 47]. Since the amplification of the K-H instabilities is dependent on Reynolds number, which does not vary across the suction and no-suction test cases, the size of the laminar separation bubble is expected to be consistent.

An interesting behavior is observed for the α = -1° and -2° flow visualization images with suction applied presented in Figs. 3.57 and 3.58. For these two cases, a distinct laminar separation bubble similar to those observed in all no-suction conditions and for suction conditions at angles of attack between $\alpha = 2^\circ - 0^\circ$ (Figs. 3.49 to 3.56) could not be identified. Instead, a low-shear region (characterized by small displacement of oil observed while performing the experiments) leading all the way to the slot location was observed for these two cases, with the region downstream of the slot (attached turbulent flow) being fairly consistent with the observations corresponding to the other angles of attack for both the suction and no-suction conditions. It is believed that since at these low angles of attack the boundary layer is not subject to significantly strong pressure gradients across the upper surface when compared to higher angles of attack, the flow is able to transition and remain attached across the shock with the additional aid of suction being applied across region "II" outlined in these images. However, since these images present a time-averaged representation of an unsteady shock oscillation process as well as a qualitative indication of shear patterns near the surface of the airfoil, a conclusive statement cannot be made regarding the transition process for these two angles of attack characterized rather by a lower-shear region based solely on the data available.

3.4 Transonic Shock Characteristics

As occurs to airfoils operating in the transonic regime, when the $C_{p,crit}$ is exceeded, a local supersonic flow region is produced over the surface which is terminated by the formation of a shock. Hence, it is of relevant importance to understand the shock behavior of airfoils operating at transonic speeds since it could lead to undesirable phenomena such as shock buffet and drag divergence. Figures 3.60 and 3.61 display instantaneous Schlieren images of the observed shock behavior of the airfoil being studied at the design conditions of $M = 0.7$ and $\alpha = 0^\circ$ for both suction and no-suction cases. A low-frequency oscillatory process was observed in the shock structure while performing the experiments, with the shock build-up process occurring in three distinct stages. This process is produced due to a hysteresis feedback interaction often seen for operation of airfoils at low transonic freestream Mach numbers. As observed in Figs. 3.60a and 3.61a, Mach waves start to become visible on the upper surface of the airfoil. This then leads to the fully developed shock structure which can be observed in Figs. 3.60b and 3.61b. Lastly, as can be seen in Figs. 3.60c and 3.61c, the shock begins to weaken and dissipate towards the end of the oscillation. This process agrees well with the phenomena identified by Levy, where periodic oscillations in shock-wave location and intensity were observed at lower-transonic Mach numbers [48]. The build-up process is observed to be quite similar for both the suction and no-suction cases; however, some qualitative differences were inferred from experimental observation. By comparing Figs. 3.60b and 3.61b, the suction case appears to have a shock with a well-defined lambda structure. Also in Fig. 3.61b, the location of the fully developed shock appears further downstream on the airfoil upper surface as an effect of suction applied when compared to Fig. 3.60b. These differences outlined in the shock characteristics between the suction and no-suction cases at $\alpha = 0^\circ$ are also consistent among the other angles of attack.

In order to determine the characteristic frequencies in the shock oscillatory process and how suction affects it, a PSD analysis based on extracted pixel intensities was performed on the Schlieren data obtained. Sampling of the Schlieren images was done at a rate of 6 kHz, therefore the maximum frequency resolved in the PSD analysis was the Nyquist limit of 3 kHz. Hence, the full PSD for the design condition of $M = 0.7$ and $\alpha = 0^\circ$ is presented in Fig. 3.62 where the lower frequency modes appear to be dominant. Detailed views of this low-frequency region are shown for all angle-of-attack cases in Figs. 3.63 to 3.72, plotted individually for suction and no-suction conditions. When considering the PSD for the $\alpha = 0^\circ$ no-suction case in Fig. 3.67, a broadband peak corresponding to the oscillatory unsteady behavior of the shock is

observed with its highest peak recorded at a frequency of 22.38 Hz. When observing the PSD in Fig. 3.68 corresponding to the $\alpha = 0^\circ$ suction case, the amplitude of this broadband peak is significantly decreased. The application of suction appears to have a beneficial influence on the stability of the oscillatory motion of the shock. The shock build-up behavior still behaves in a fashion consistent with that of the no-suction case; however, the oscillation of the general shock structure is reduced, which also reduces the flow-field unsteadiness associated with it.

When considering the PSDs from the off-design angles of attack (Figs. 3.63 to 3.66 and 3.69 to 3.72) at $\alpha = 2^\circ$, 1°, -1°, and -2°, respective characteristics frequencies for the oscillatory broadband peaks for the no-suction conditions were observed to be 22.24 Hz, 22.87 Hz, 23.51 Hz, and 24.14 Hz for each corresponding angle of attack. The frequencies are in reasonable agreement with that at the design angle of attack of 22.38 Hz, behaving in a constant fashion or slightly decreasing in an insignificant linear form with increasing angle of attack. When considering the $\alpha = 2^\circ$, 1°, and 0° conditions (Figs. 3.63 to 3.68), a significant reduction in the oscillation amplitude is observed from the PSDs for the suction conditions, as compared to the no-suction case. The reduction in the amplitude is also observed to be greater as the angle of attack is increased. For the $\alpha = -1^\circ$ and -2° conditions, no significant influence is observed in the PSD amplitudes for the characteristic oscillation frequencies under the influence of suction. Hence, suction is shown to provide a significant reduction in the PSD amplitudes at the higher angles of attack resulting in more-stable shock structures across the upper surface of the airfoil. This observation shows excellent agreement with those in Sections 3.1 and 3.2.1, where influences in the pressure distributions and drag charactistics, respectively, were predominantly greater at the higher angles of attack cases where suction has the greatest influence in the performance of the airfoil. Frequency band peaks near the $40 - 50$ Hz range observed in the PSD plots are related to frequency noise introduced by the wind tunnel operation.

In addition to shock positions identified by surface-oil flow visualizations, Fig. 3.59 also shows the averaged shock locations obtained through Schlieren imaging for suction and no-suction cases which were observed to oscillate across an approximate distance of $6\%c$ at the design condition of $M = 0.7$. The flow visualization images are a time-averaged representation of an unsteady process; hence, when compared to the locations obtained from the Schlieren data acceptable agreement is found. As can be seen for the no-suction cases, the shock location shifts by approximately $8\%c$ while for the suction cases the location shifts approximately $3\%c$ across the angle-of-attack range. This agreement between the Schlieren and

flow visualization experiments again highlights the importance of boundary-layer transition prior to the shock location to prevent laminar shock-induced separation, as a turbulent boundary layer is able to remain attached to the airfoil surface when subject to much larger adverse pressure gradients across the pressure recovery region due to the added momentum from turbulent mixing [49].

3.5 Figures

3.5.1 Pressure Distributions

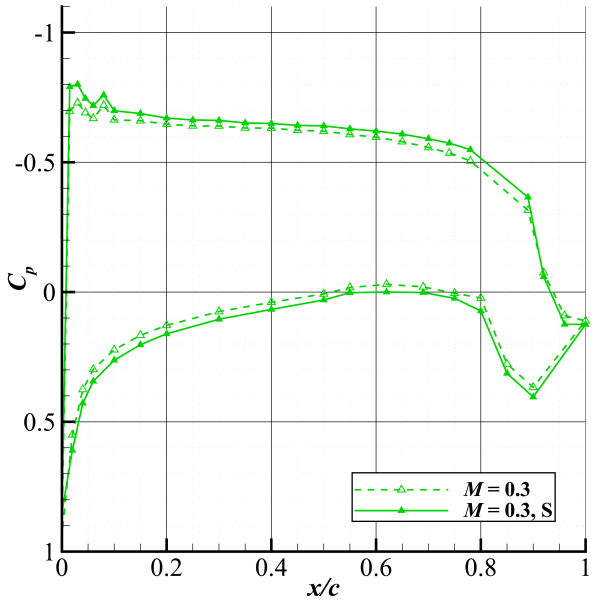

Figure 3.1: C_p distribution for $M = 0.3$ at $\alpha = 2°$.

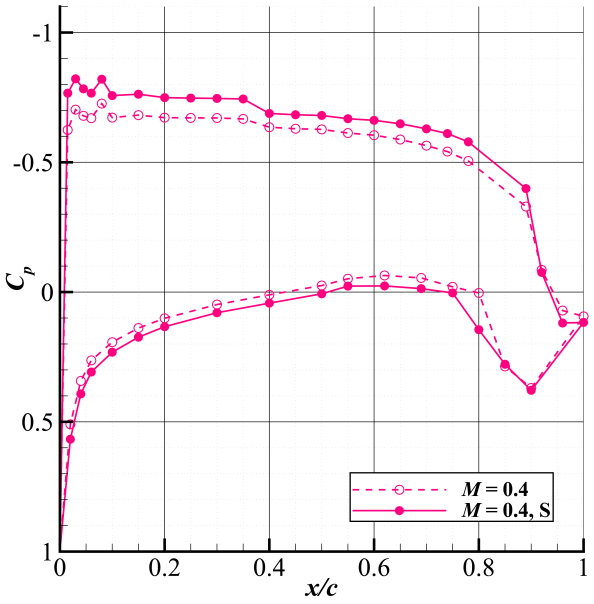

Figure 3.2: C_p distribution for $M = 0.4$ at $\alpha = 2°$.

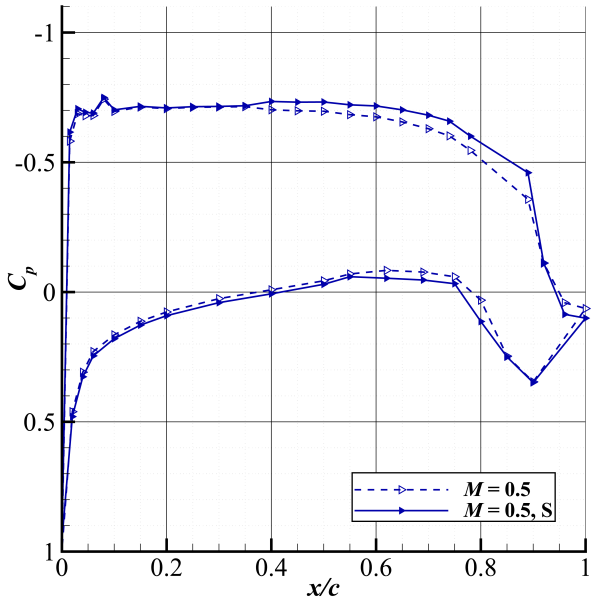

Figure 3.3: C_p distribution for $M = 0.5$ at $\alpha = 2°$.

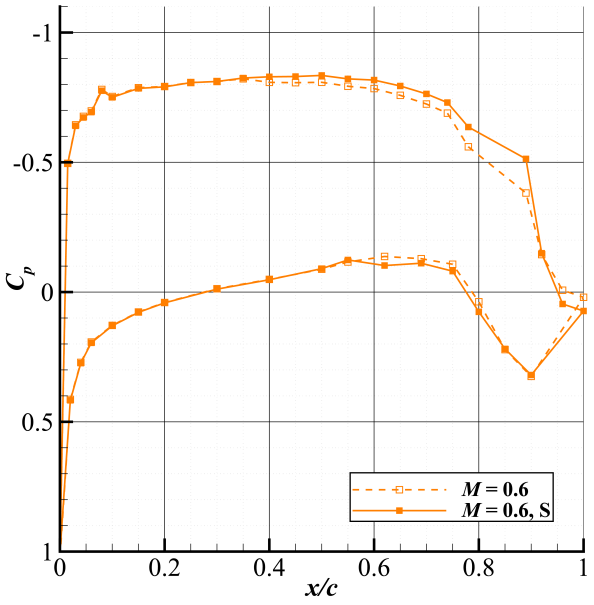

Figure 3.4: C_p distribution for $M = 0.6$ at $\alpha = 2°$.

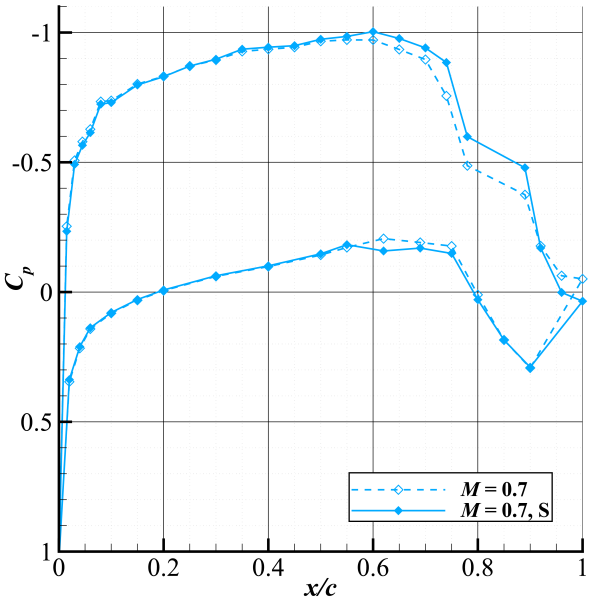

Figure 3.5: C_p distribution for $M = 0.7$ at $\alpha = 2°$.

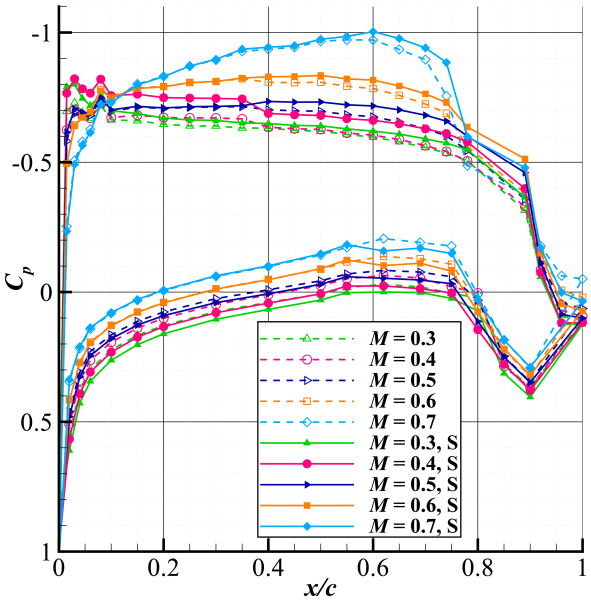

Figure 3.6: C_p distributions at $\alpha = 2°$.

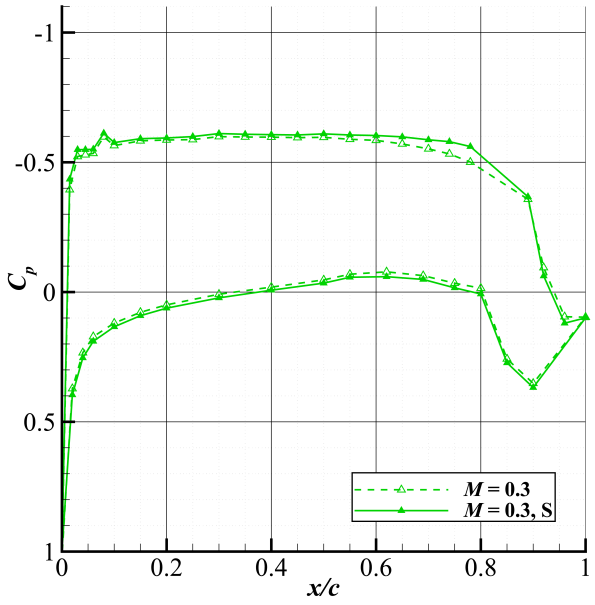

Figure 3.7: C_p distribution for $M = 0.3$ at $\alpha = 1°$.

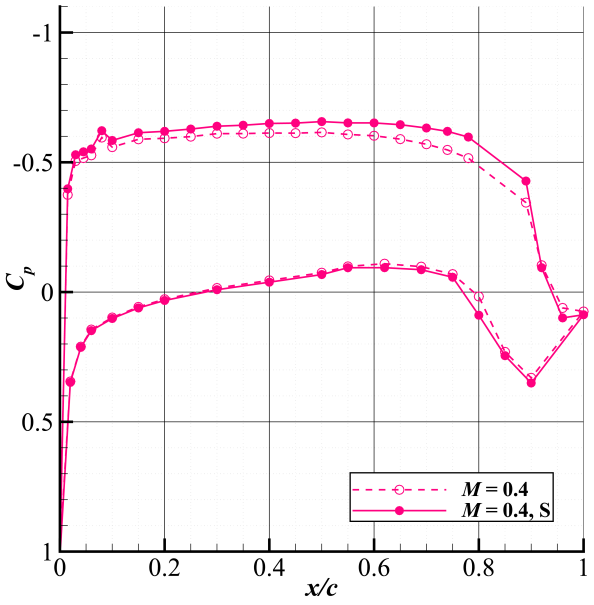

Figure 3.8: C_p distribution for $M = 0.4$ at $\alpha = 1°$.

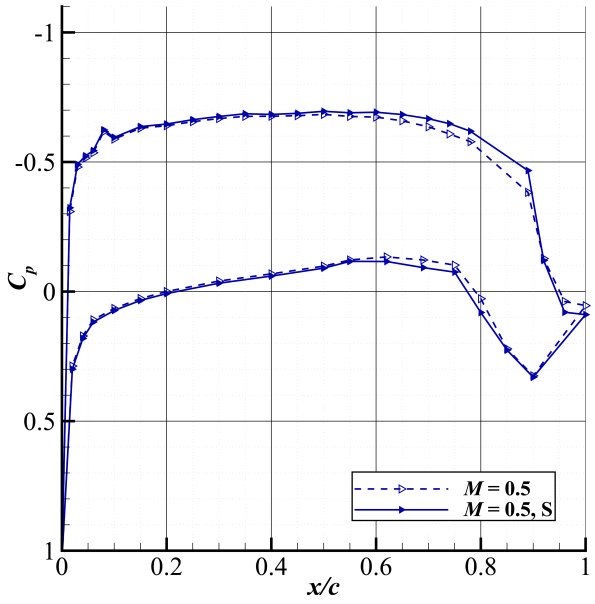

Figure 3.9: C_p distribution for $M = 0.5$ at $\alpha = 1°$.

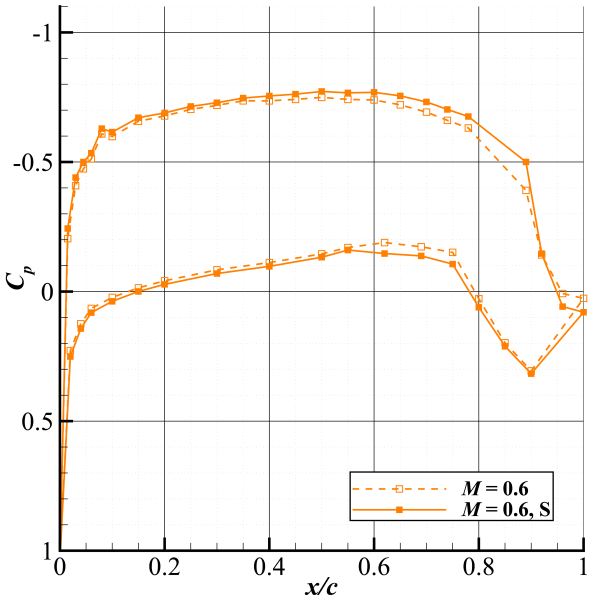

Figure 3.10: C_p distribution for $M = 0.6$ at $\alpha = 1°$.

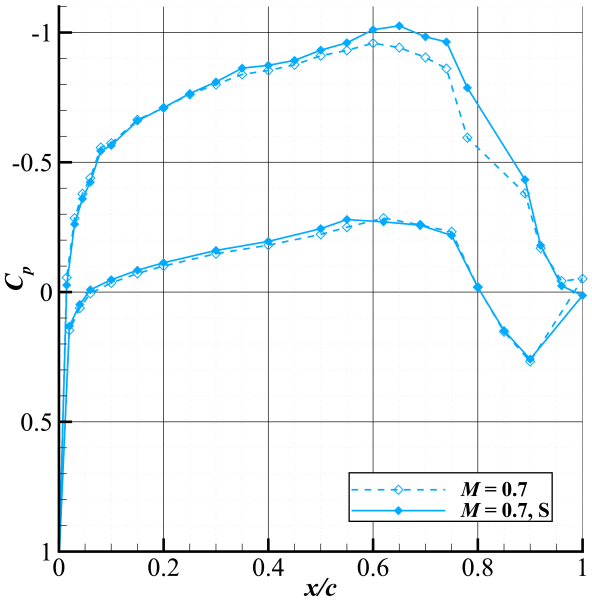

Figure 3.11: C_p distribution for $M = 0.7$ at $\alpha = 1°$.

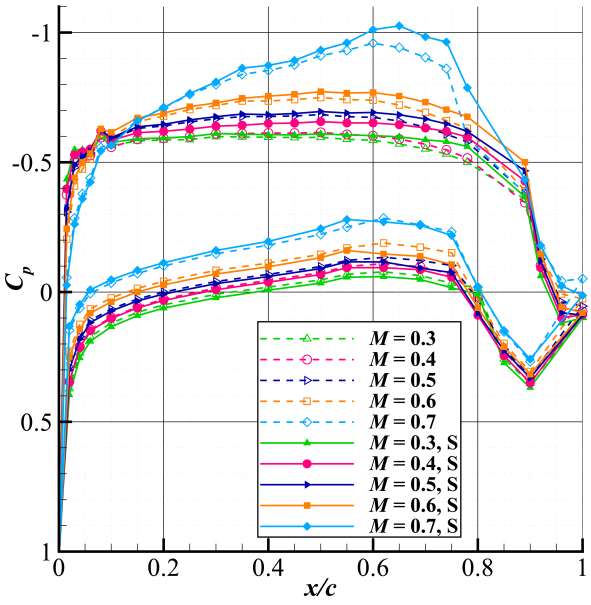

Figure 3.12: C_p distributions at $\alpha = 1°$.

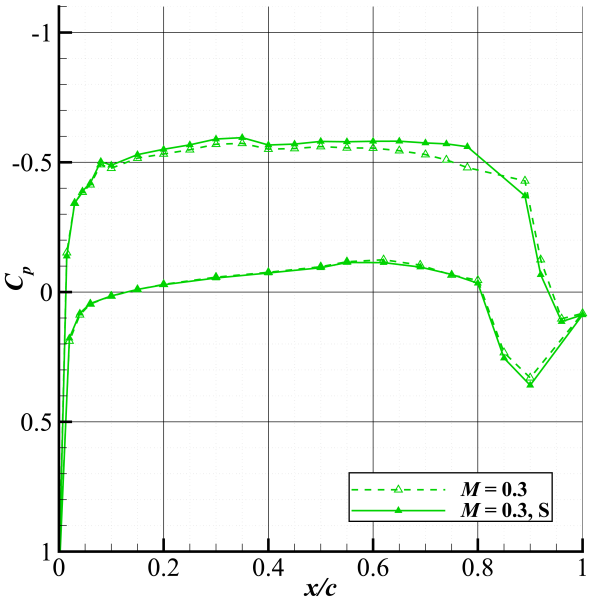

Figure 3.13: C_p distribution for $M = 0.3$ at $\alpha = 0°$.

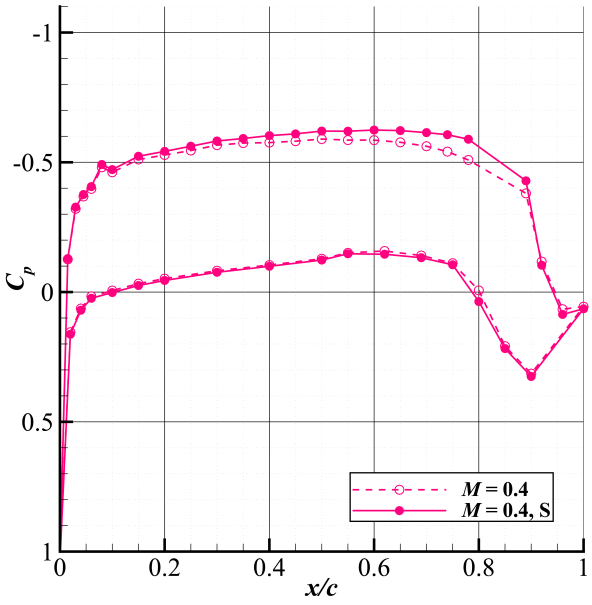

Figure 3.14: C_p distribution for $M = 0.4$ at $\alpha = 0°$.

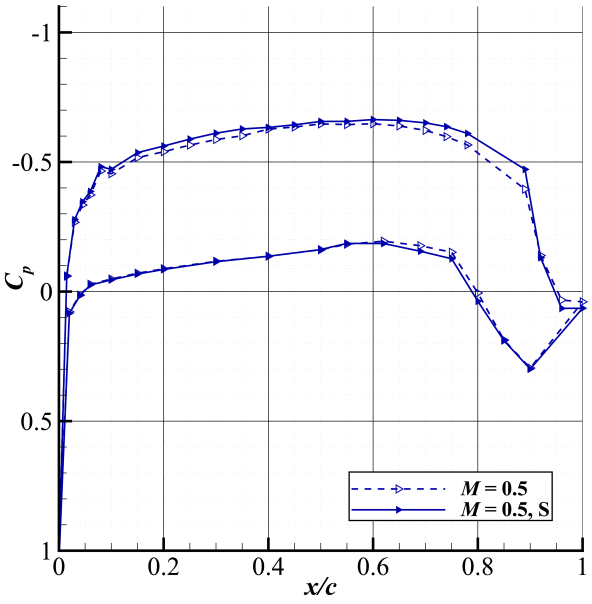

Figure 3.15: C_p distribution for $M = 0.5$ at $\alpha = 0°$.

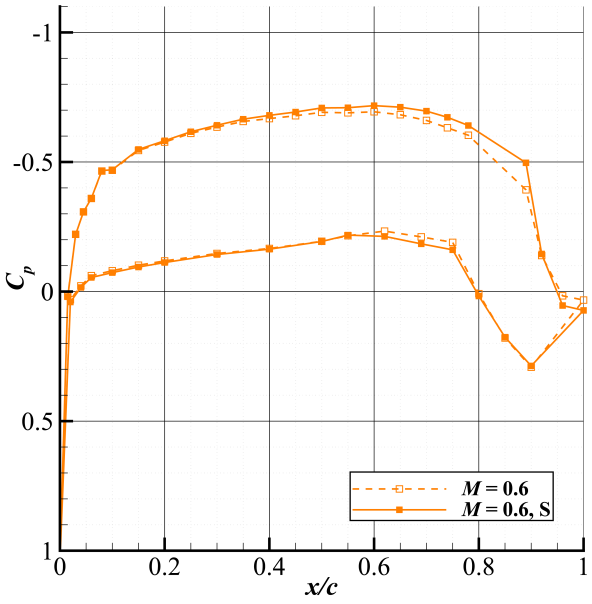

Figure 3.16: C_p distribution for $M = 0.6$ at $\alpha = 0°$.

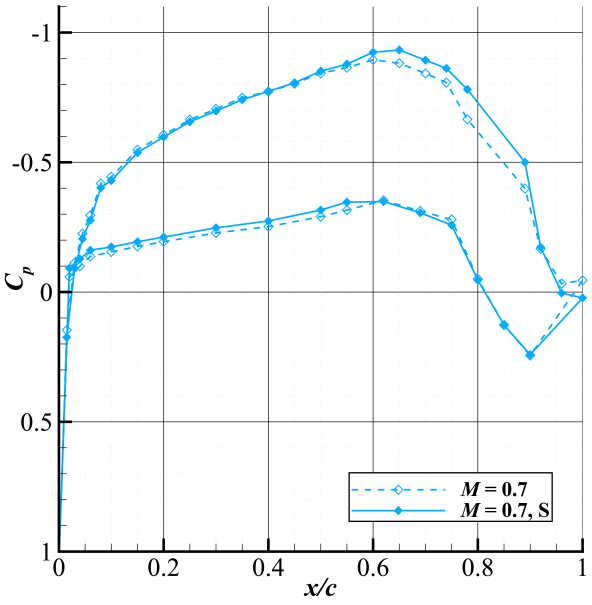

Figure 3.17: C_p distribution for $M = 0.7$ at $\alpha = 0°$.

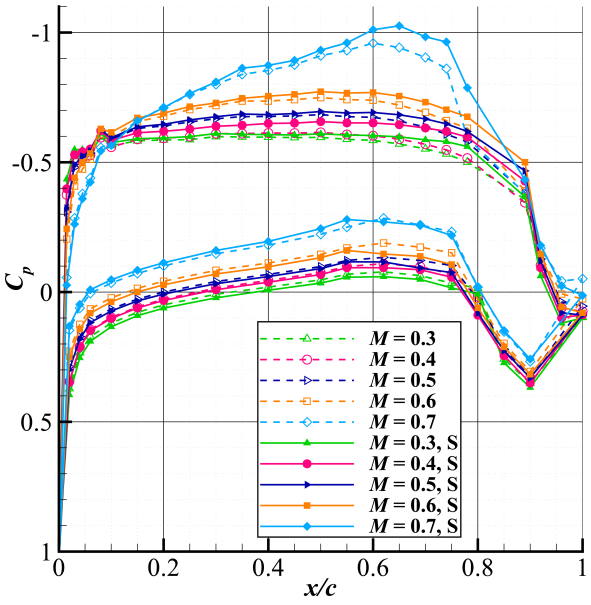

Figure 3.18: C_p distributions at $\alpha = 0°$.

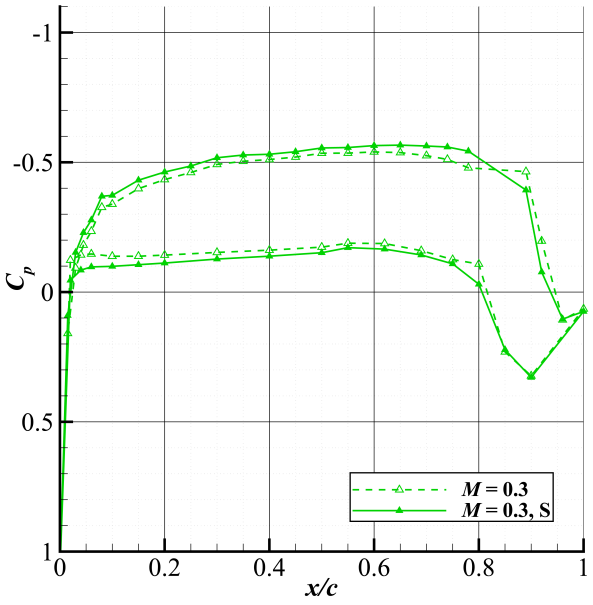

Figure 3.19: C_p distribution for $M = 0.3$ at $\alpha = -1°$.

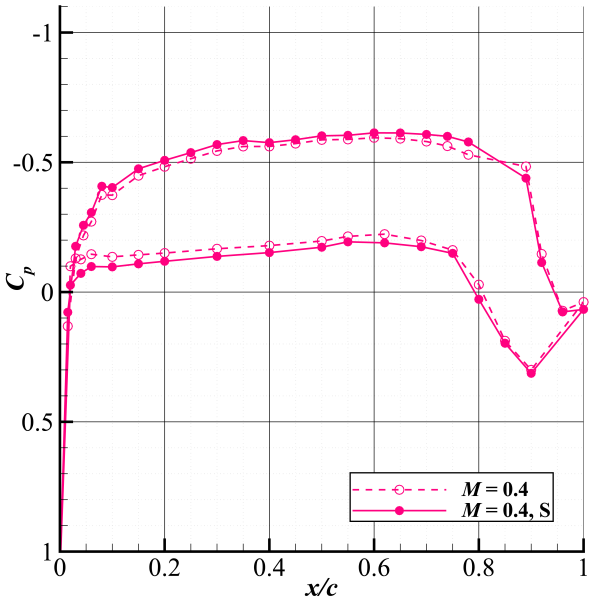

Figure 3.20: C_p distribution for $M = 0.4$ at $\alpha = -1°$.

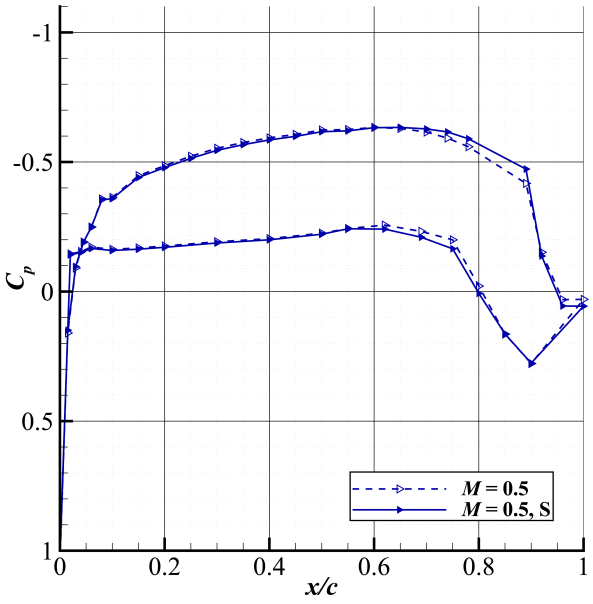

Figure 3.21: C_p distribution for $M = 0.5$ at $\alpha = -1°$.

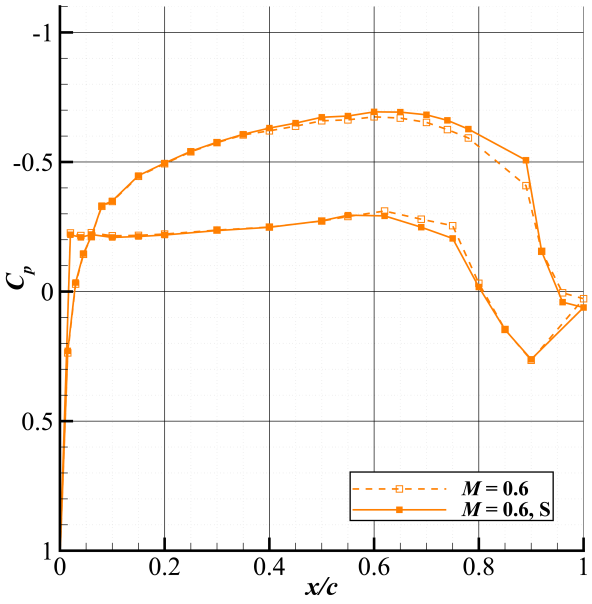

Figure 3.22: C_p distribution for $M = 0.6$ at $\alpha = -1°$.

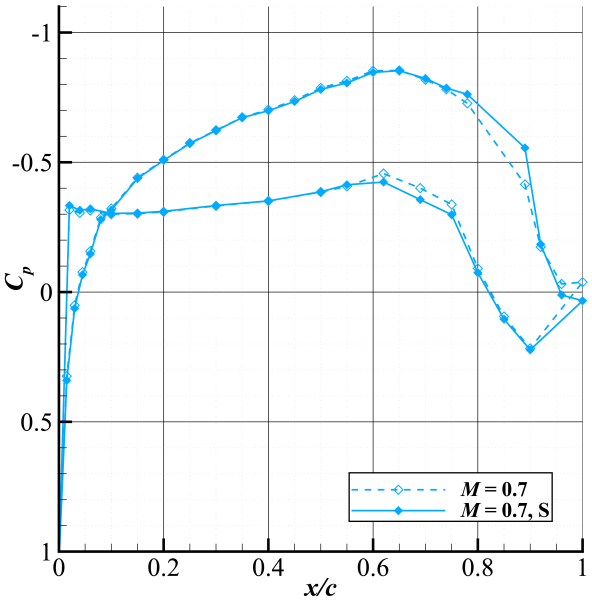

Figure 3.23: C_p distribution for $M = 0.7$ at $\alpha = -1°$.

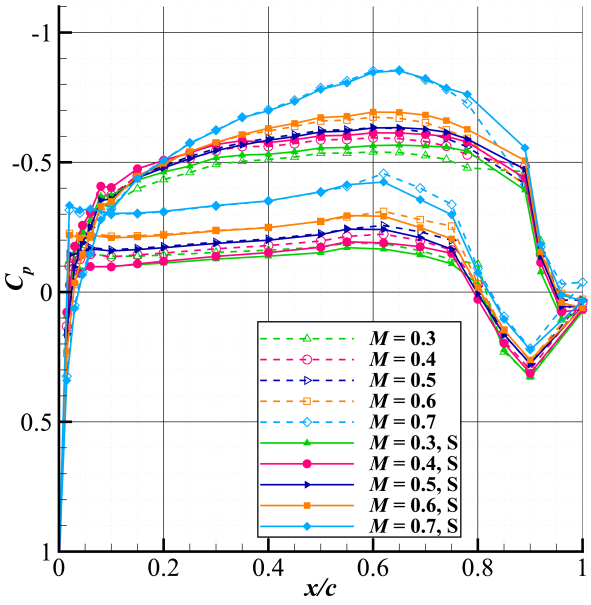

Figure 3.24: C_p distributions at $\alpha = -1°$.

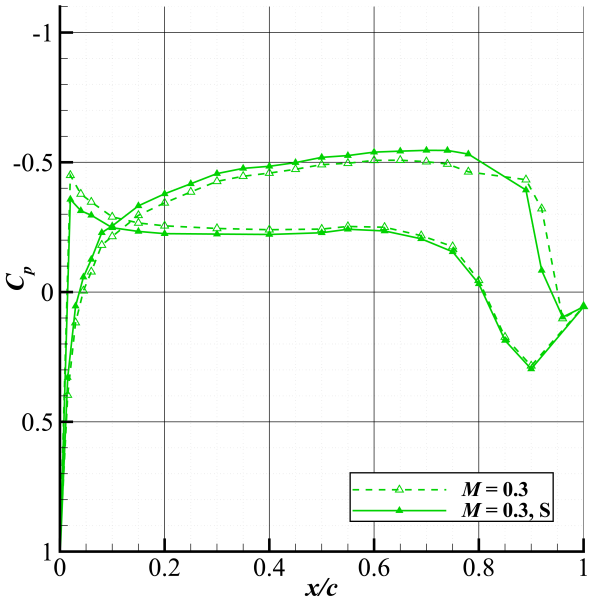

Figure 3.25: C_p distribution for $M = 0.3$ at α = -2°.

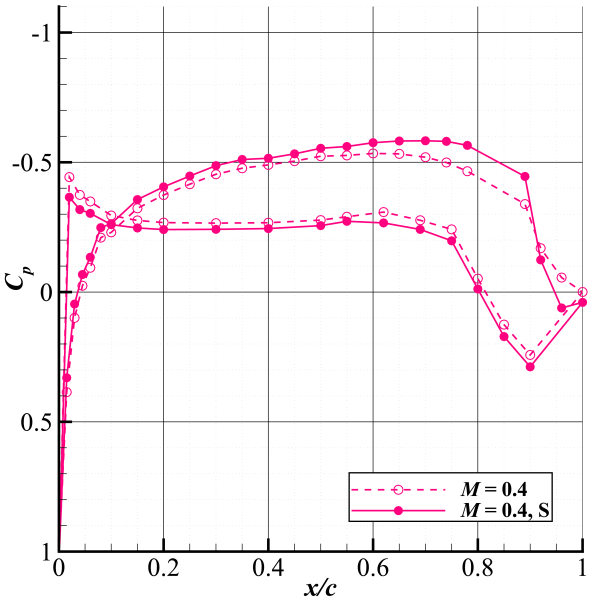

Figure 3.26: C_p distribution for $M = 0.4$ at α = -2°.

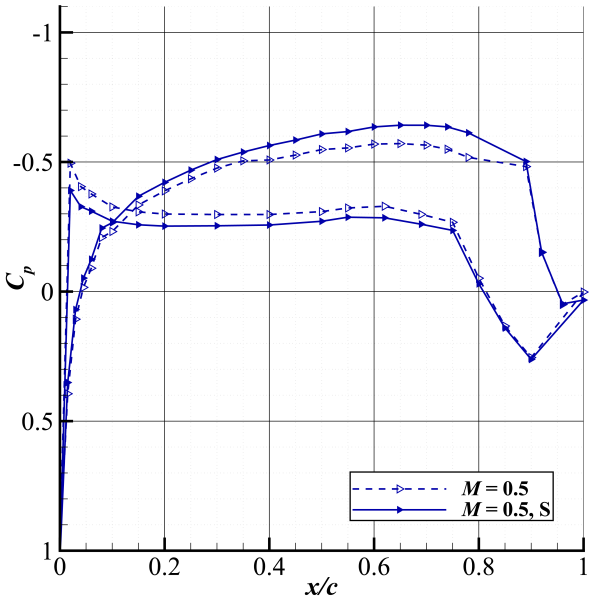

Figure 3.27: C_p distribution for $M = 0.5$ at α = -2°.

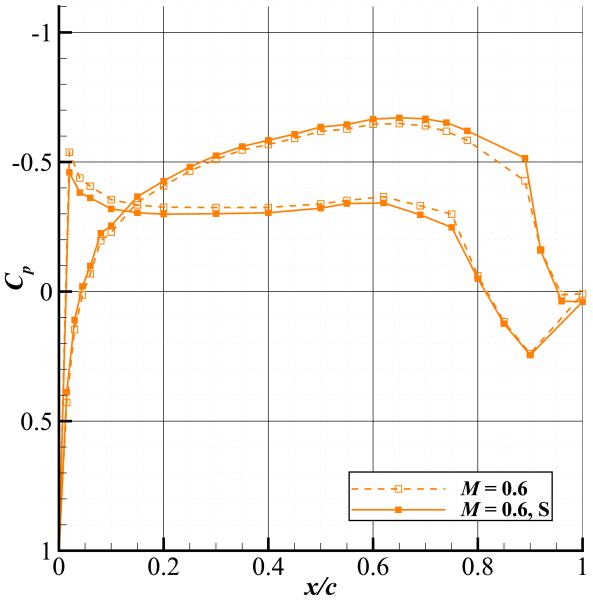

Figure 3.28: C_p distribution for $M = 0.6$ at α = -2°.

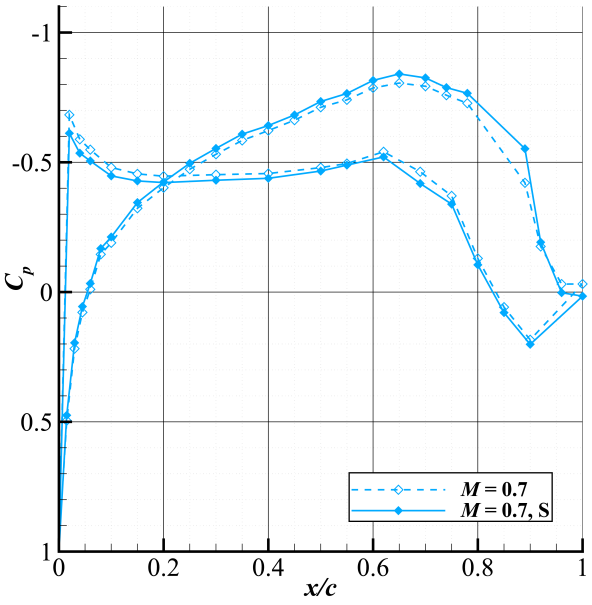

Figure 3.29: C_p distribution for M = 0.7 at α = -2°.

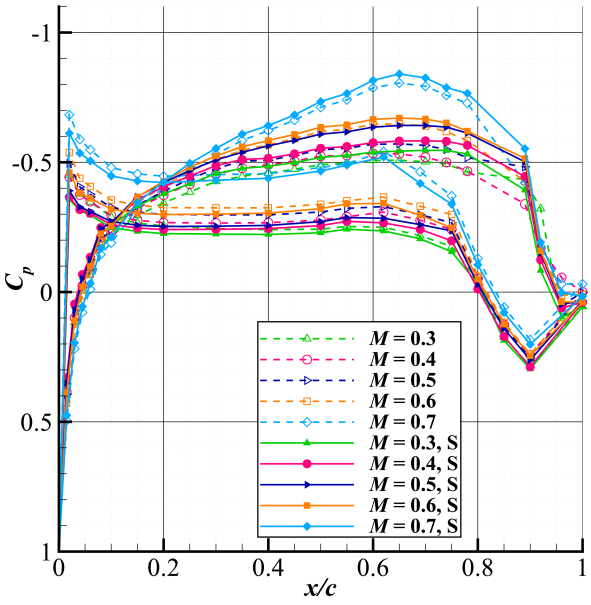

Figure 3.30: C_p distributions at α = -2°.

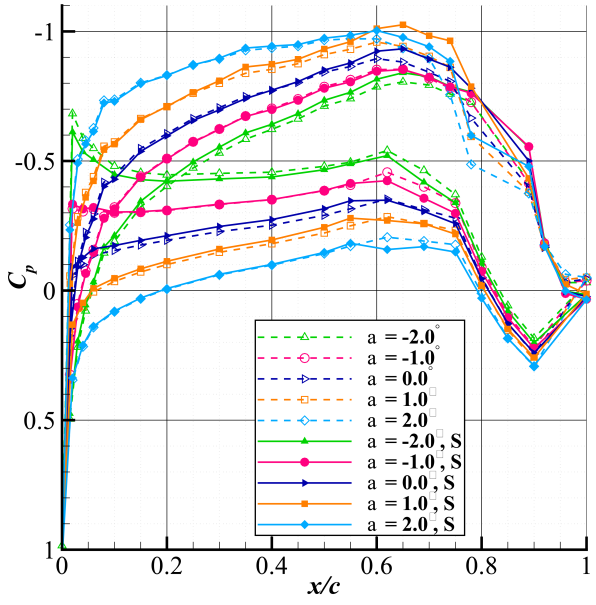

Figure 3.31: C_p distributions at M = 0.7.

3.5.2 Aerodynamic Polars

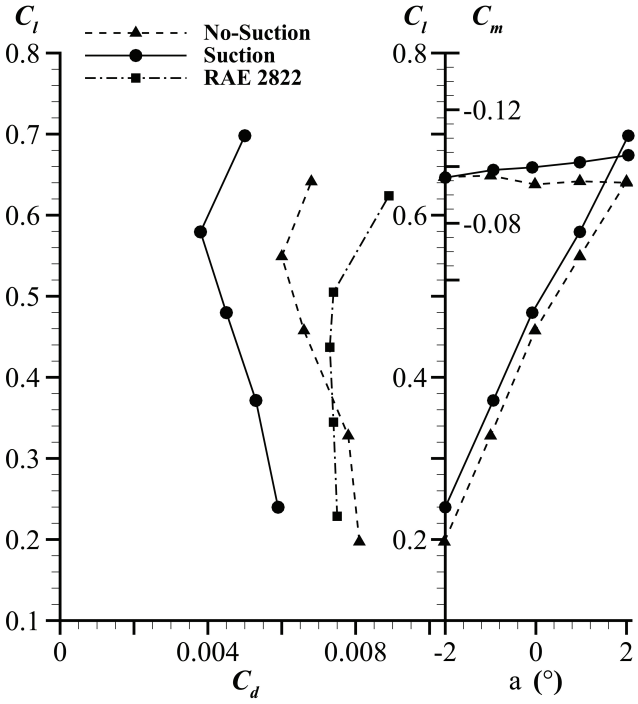

Figure 3.32: Aerodynamic polars for $M = 0.3$.

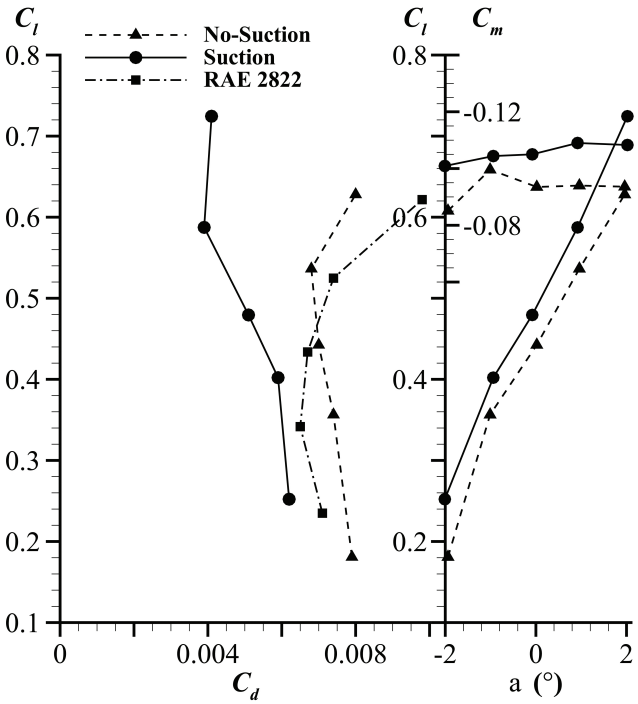

Figure 3.33: Aerodynamic polars for $M = 0.4$.

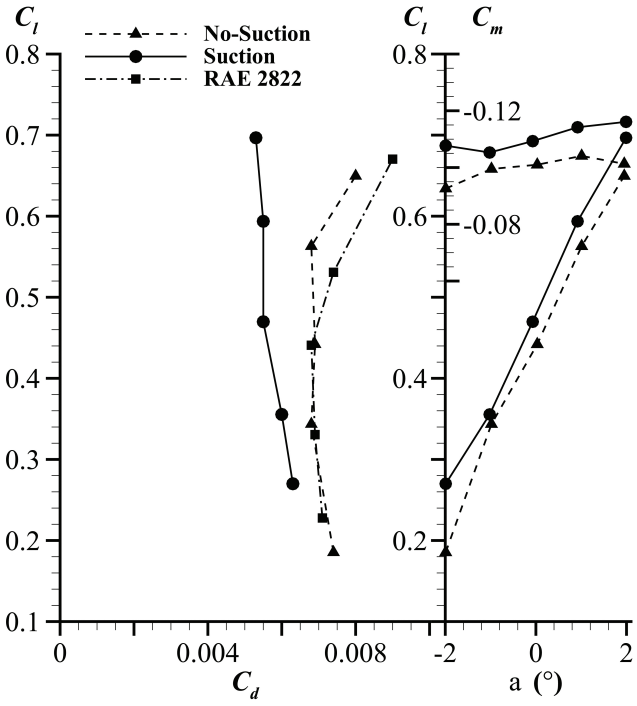

Figure 3.34: Aerodynamic polars for $M = 0.5$.

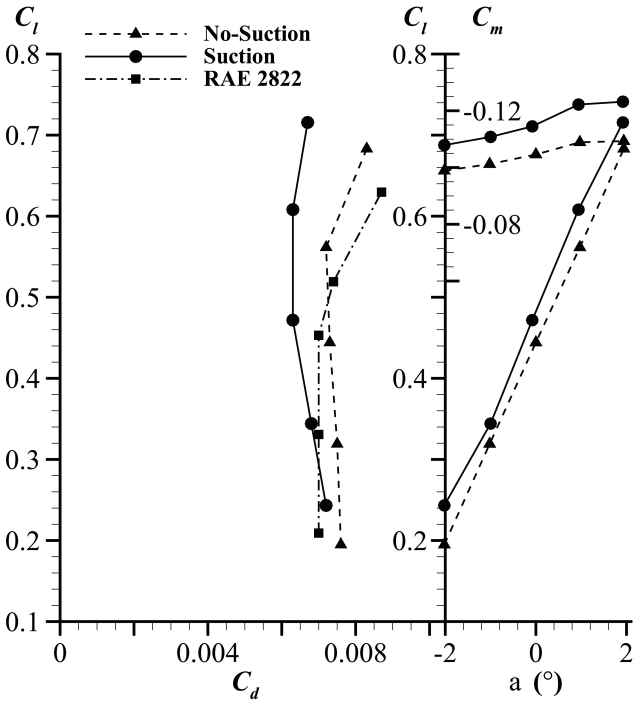

Figure 3.35: Aerodynamic polars for $M = 0.6$.

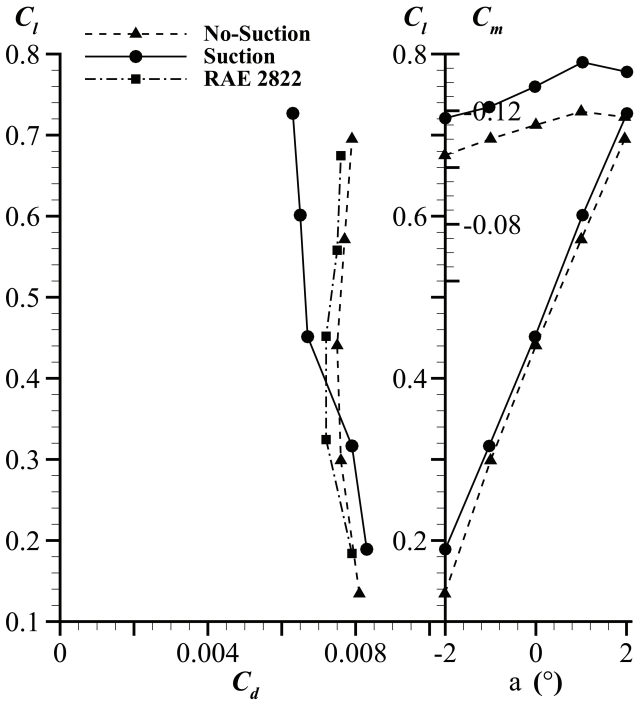

Figure 3.36: Aerodynamic polars for $M = 0.7$.

3.5.3 Wake Velocity Flow Field

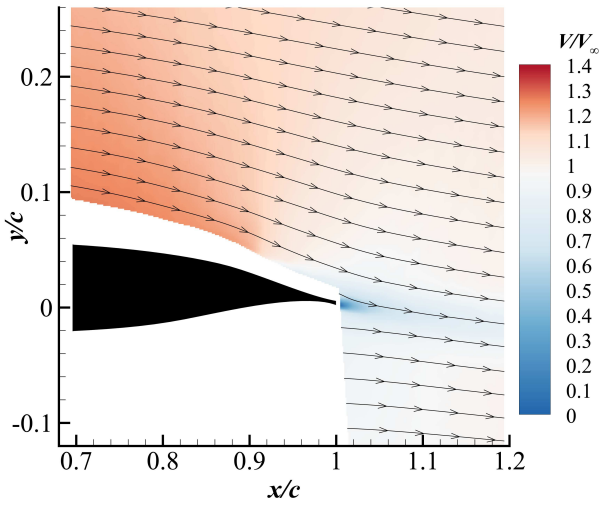

Figure 3.37: Flow field velocity contour at $M = 0.3$ at $\alpha = 0°$ no-suction condition.

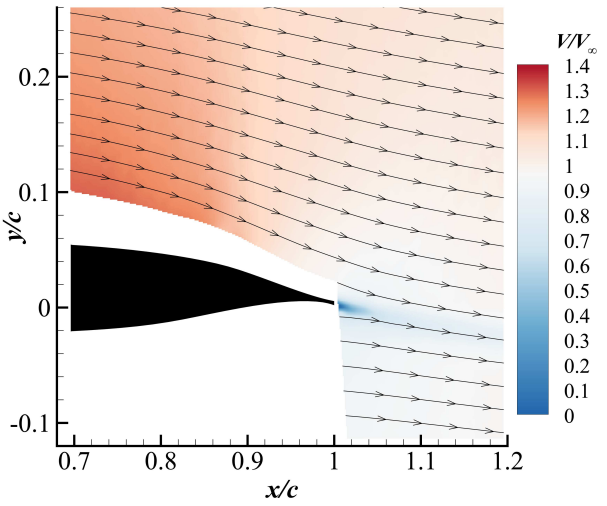

Figure 3.38: Flow field velocity contour at $M = 0.3$ at $\alpha = 0°$ suction condition.

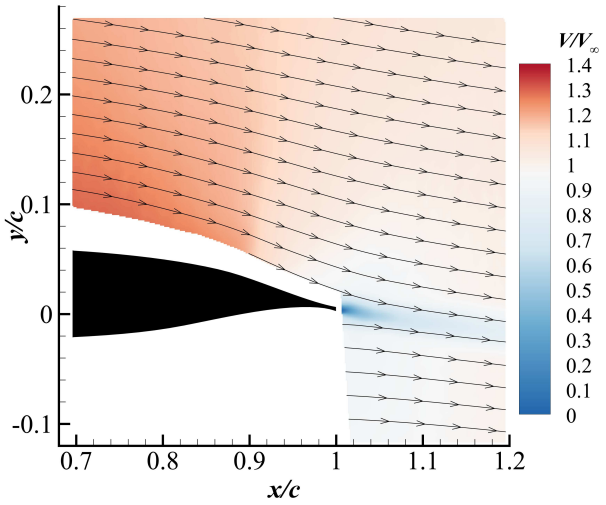

Figure 3.39: Flow field velocity contour at $M = 0.4$ at $\alpha = 0°$ no-suction condition.

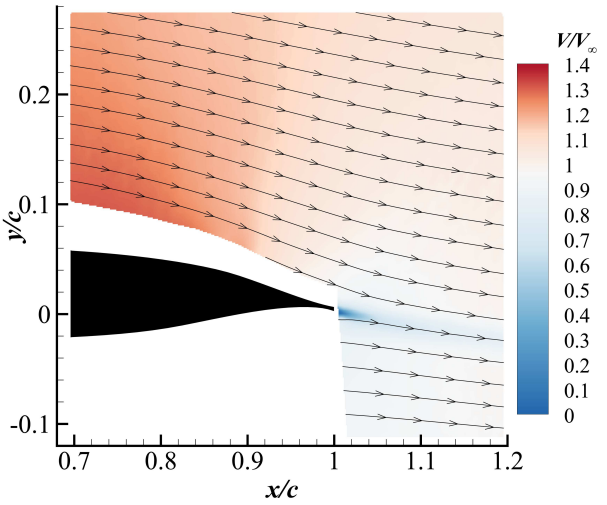

Figure 3.40: Flow field velocity contour at $M = 0.4$ at $\alpha = 0°$ suction condition.

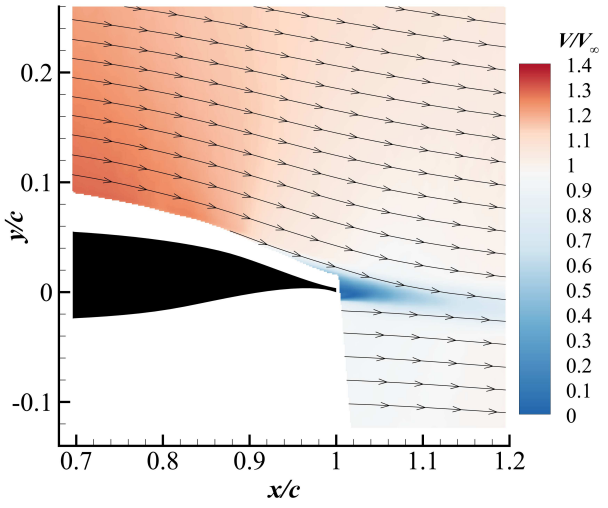

Figure 3.41: Flow field velocity contour at $M = 0.5$ at $\alpha = 0°$ no-suction condition.

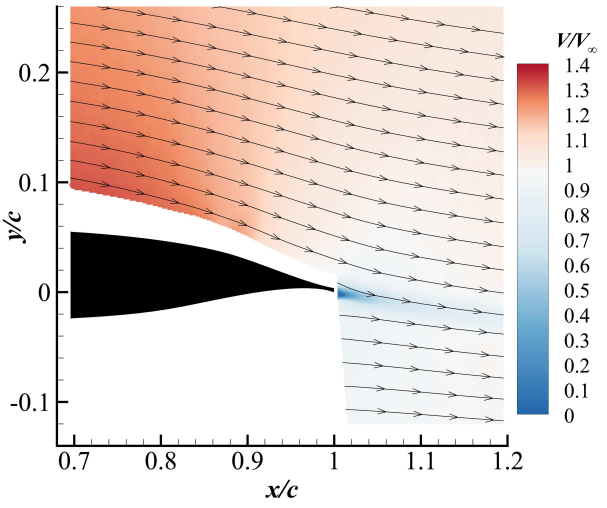

Figure 3.42: Flow field velocity contour at $M = 0.5$ at $\alpha = 0°$ suction condition.

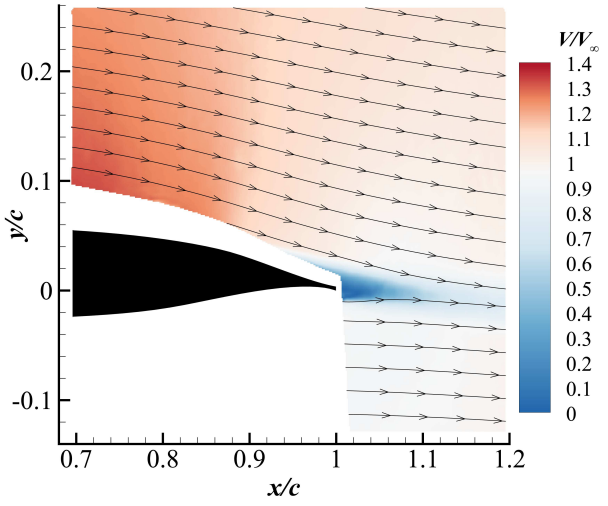

Figure 3.43: Flow field velocity contour at $M = 0.6$ at $\alpha = 0°$ no-suction condition.

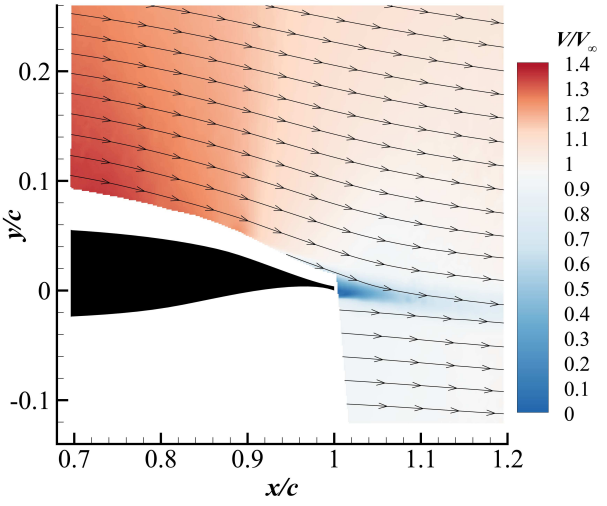

Figure 3.44: Flow field velocity contour at $M = 0.6$ at $\alpha = 0°$ suction condition.

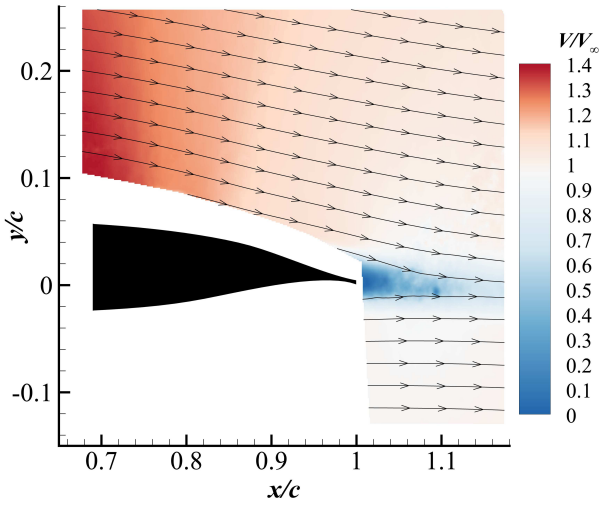

Figure 3.45: Flow field velocity contour at $M = 0.7$ at $\alpha = 0°$ no-suction condition.

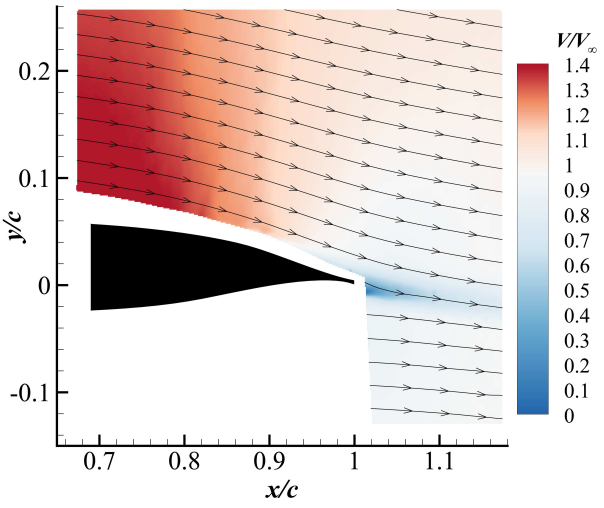

Figure 3.46: Flow field velocity contour at $M = 0.7$ at $\alpha = 0°$ suction condition.

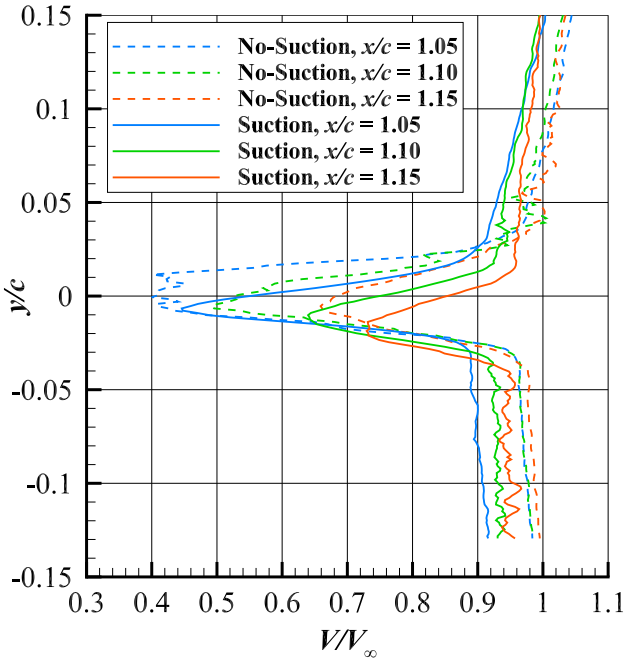

Figure 3.47: Wake velocity profile from PIV data for $M = 0.7$ and $\alpha = 0°$ at different chordwise locations.

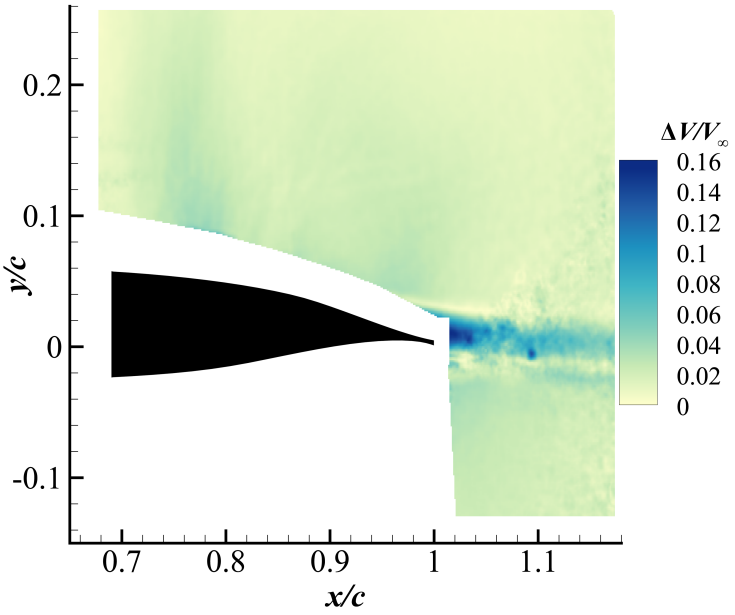

Figure 3.48: Contour of wake velocity difference between suction and no-suction cases normalized by freestream velocity for $M = 0.7$ and $\alpha = 0°$.

3.5.4 Flow Visualization Diagnostics

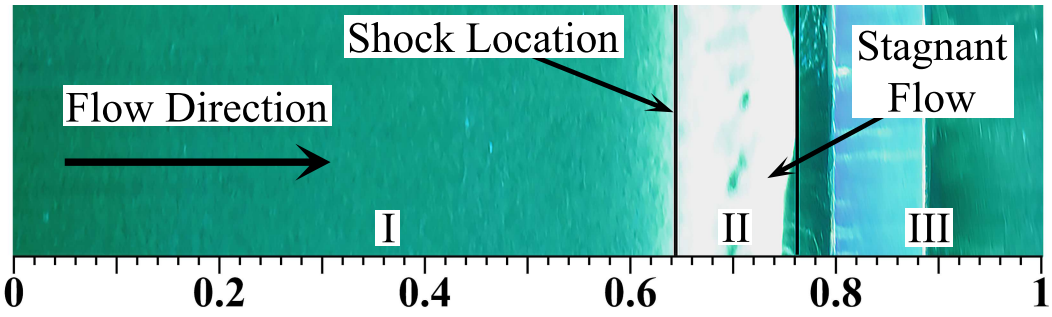

Figure 3.49: Airfoil-surface flow visualization for no-suction condition at $M = 0.7$ and $\alpha = 2°$.

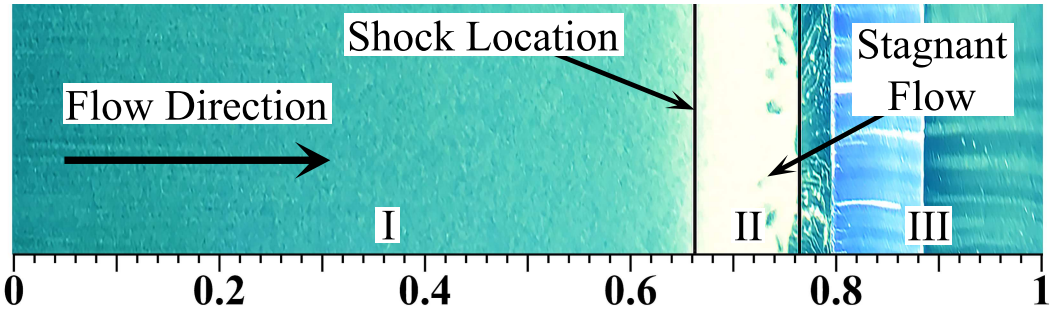

Figure 3.50: Airfoil-surface flow visualization for no-suction condition at $M = 0.7$ and $\alpha = 1°$.

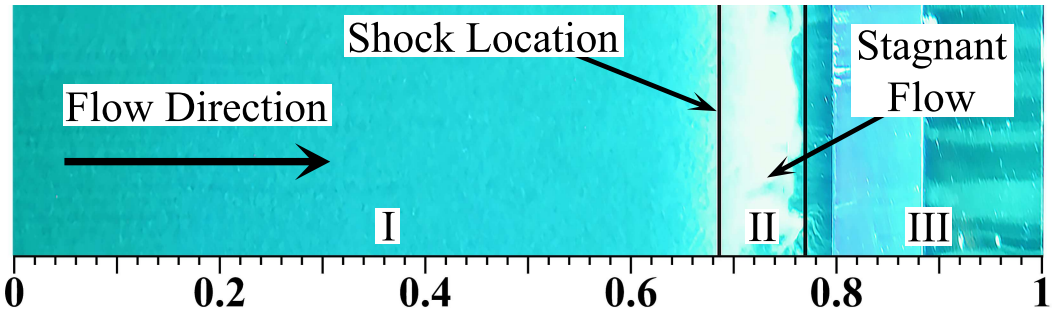

Figure 3.51: Airfoil-surface flow visualization for no-suction condition at $M = 0.7$ and $\alpha = 0°$.

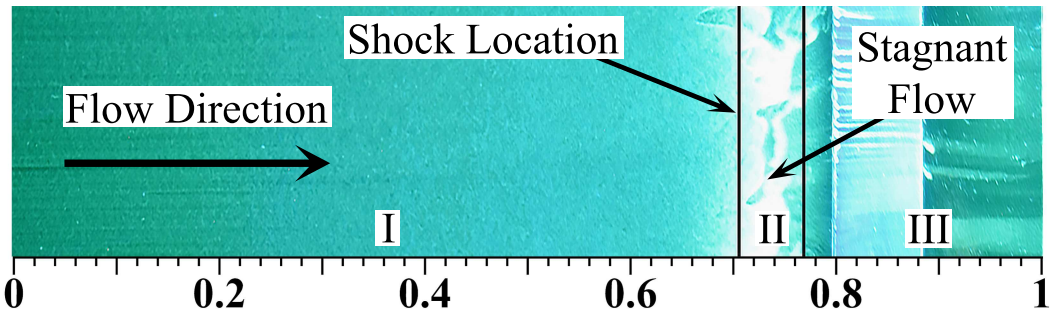

Figure 3.52: Airfoil-surface flow visualization for no-suction condition at M = 0.7 and α = -1°.

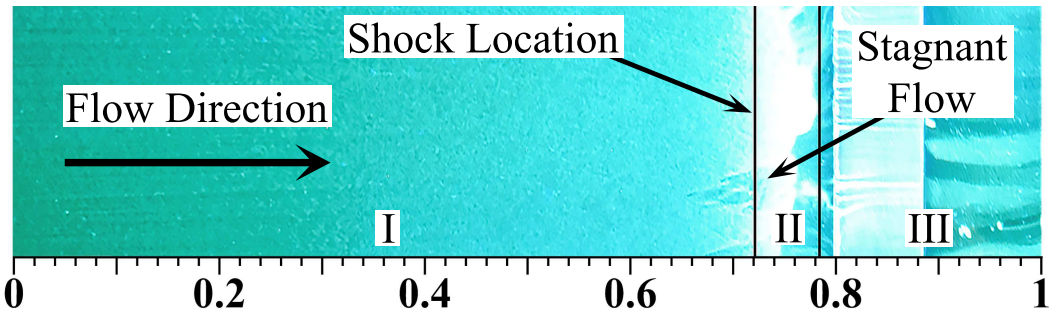

Figure 3.53: Airfoil-surface flow visualization for no-suction condition at M = 0.7 and α = -2°.

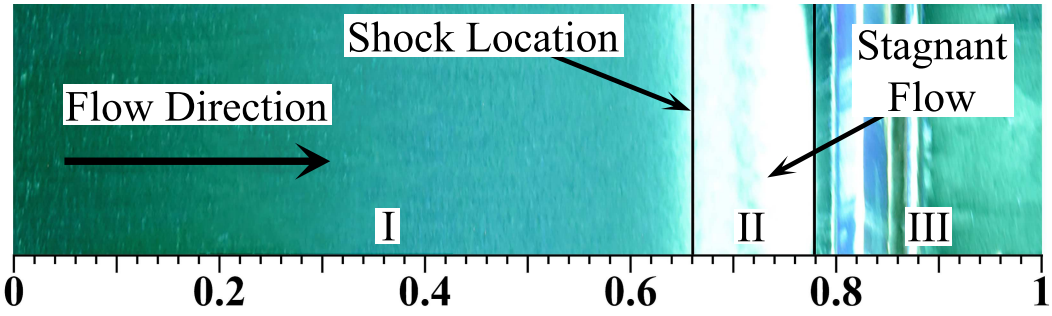

Figure 3.54: Airfoil-surface flow visualization for suction condition at $M = 0.7$ and $\alpha = 2°$.

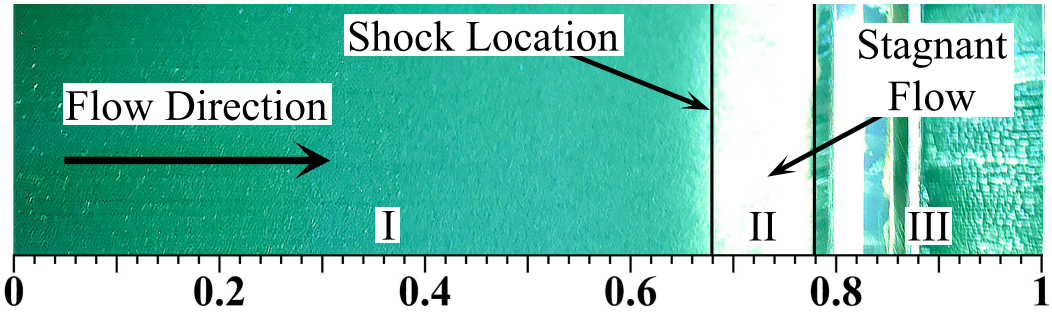

Figure 3.55: Airfoil-surface flow visualization for suction condition at $M = 0.7$ and $\alpha = 1°$.

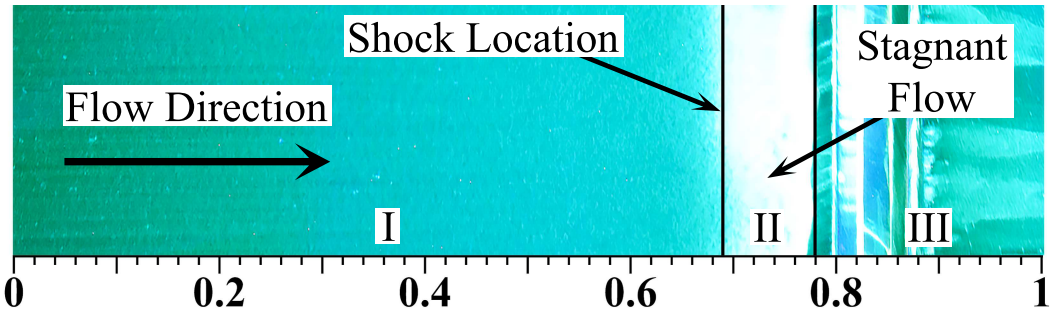

Figure 3.56: Airfoil-surface flow visualization for suction condition at $M = 0.7$ and $\alpha = 0°$.

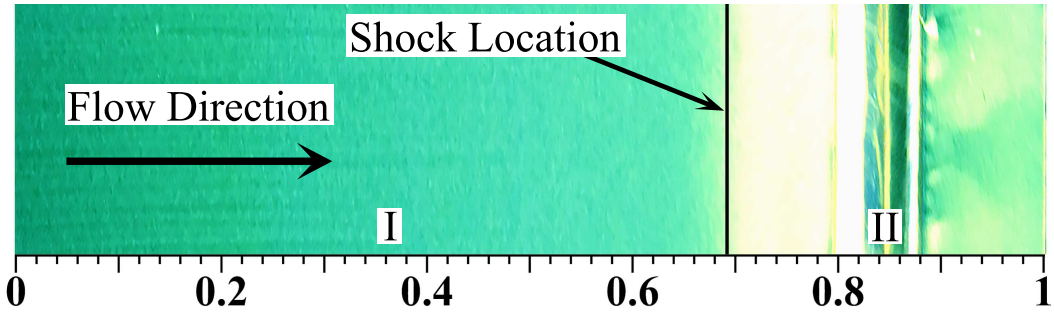

Figure 3.57: Airfoil-surface flow visualization for suction condition at M = 0.7 and α = -1°.

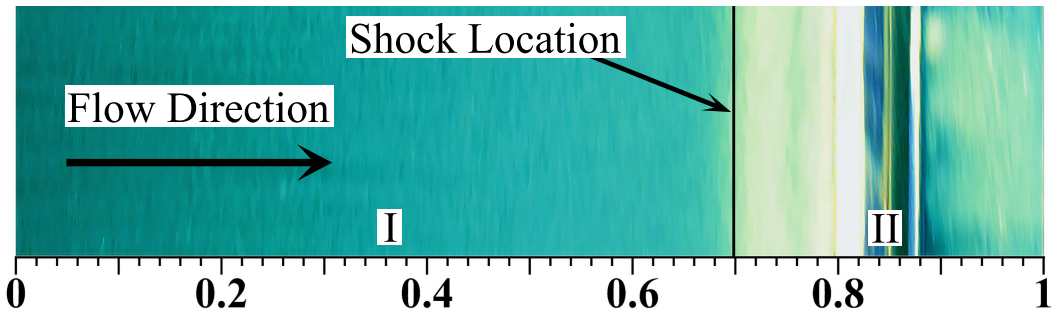

Figure 3.58: Airfoil-surface flow visualization for suction condition at M = 0.7 and α = -2°.

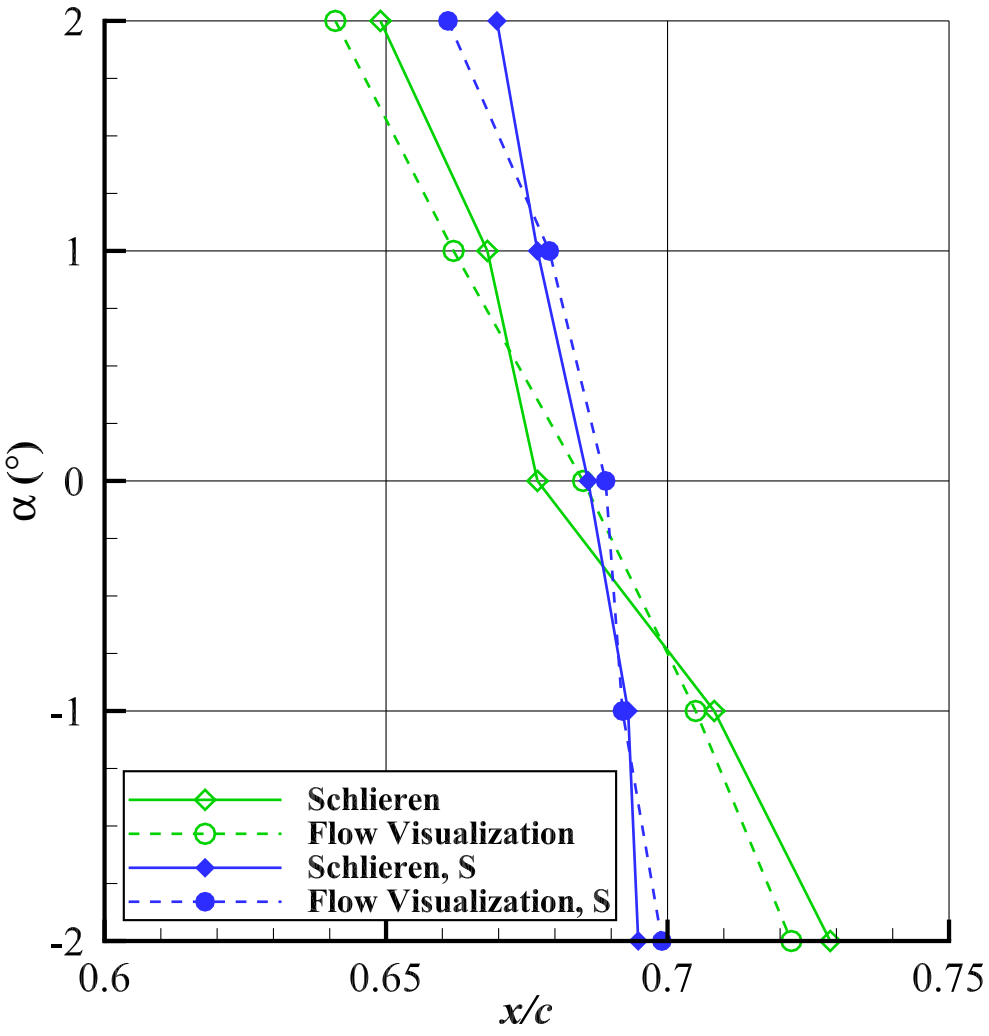

Figure 3.59: Averaged shock locations for each angle of attack, where “S” legend entries indicate suction.

3.5.5 Schlieren Imaging Diagnostics

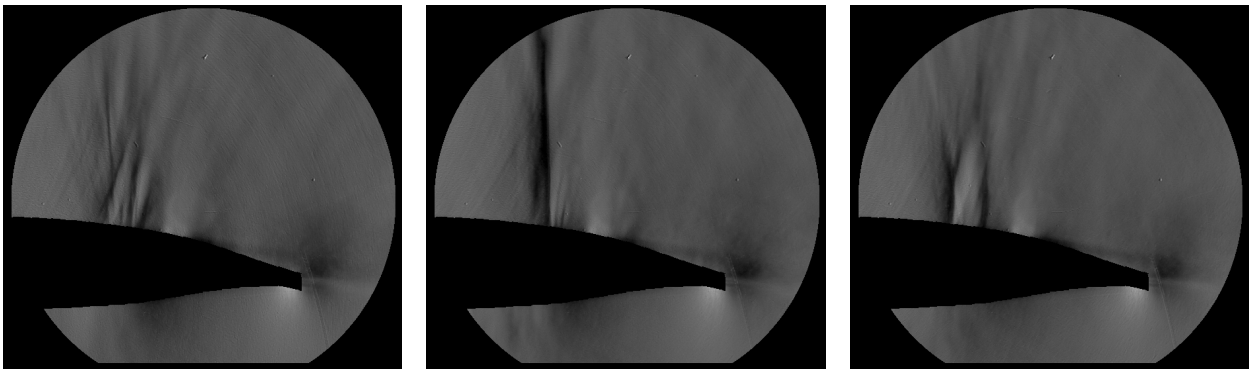

(a) Mach wave formation. (b) Shock wave fully formed. (c) Shock wave breakup.

Figure 3.60: Instantaneous Schlieren images of shock wave oscillation at $\alpha = 0^\circ$ and $M = 0.7$ for no-suction case.

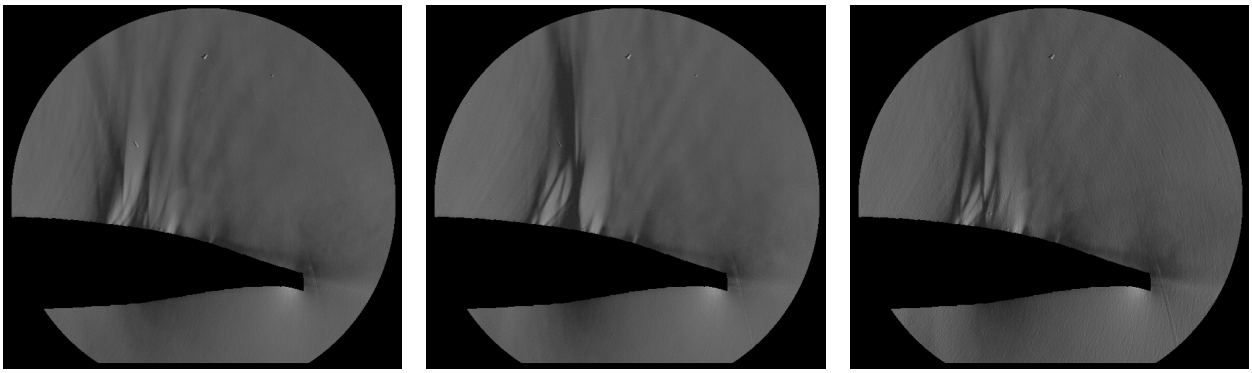

(a) Mach wave formation. (b) Shock wave fully formed. (c) Shock wave breakup.

Figure 3.61: Instantaneous Schlieren images of shock wave oscillation at $\alpha = 0^\circ$ and $M = 0.7$ for suction case.

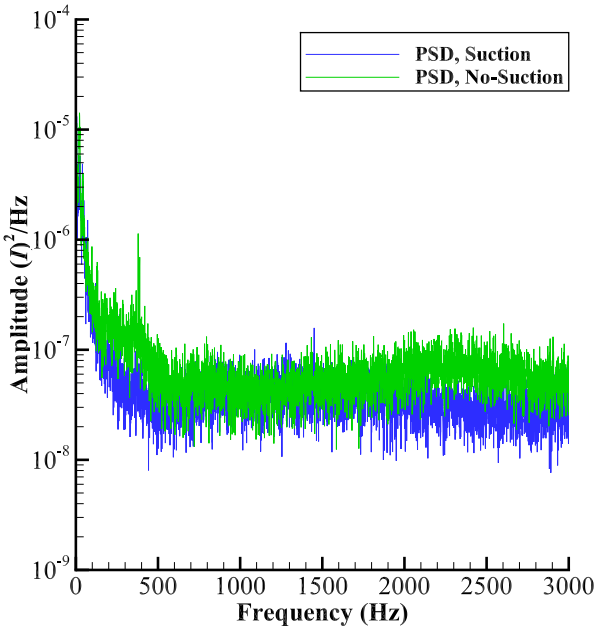

Figure 3.62: Entire resolved power spectral density of shock oscillation at $M = 0.7$ and $\alpha = 0°$ for both suction and no-suction cases.

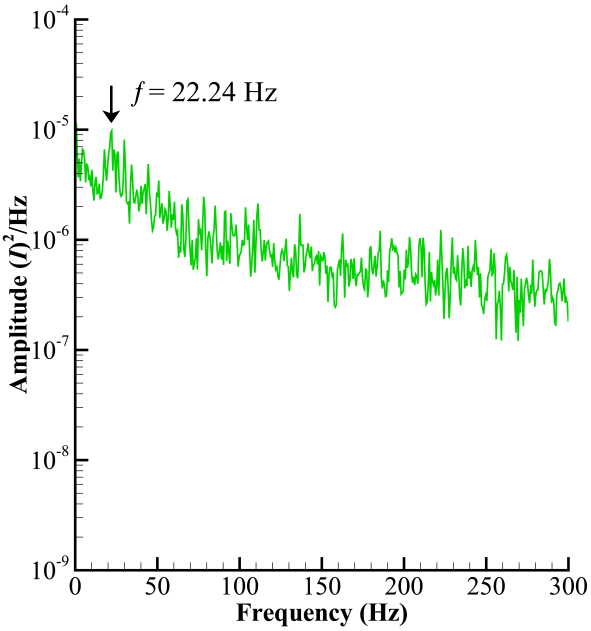

Figure 3.63: Power spectral density of shock oscillation up to 300 Hz for $M = 0.7$ and $\alpha = 2°$ no-suction case.

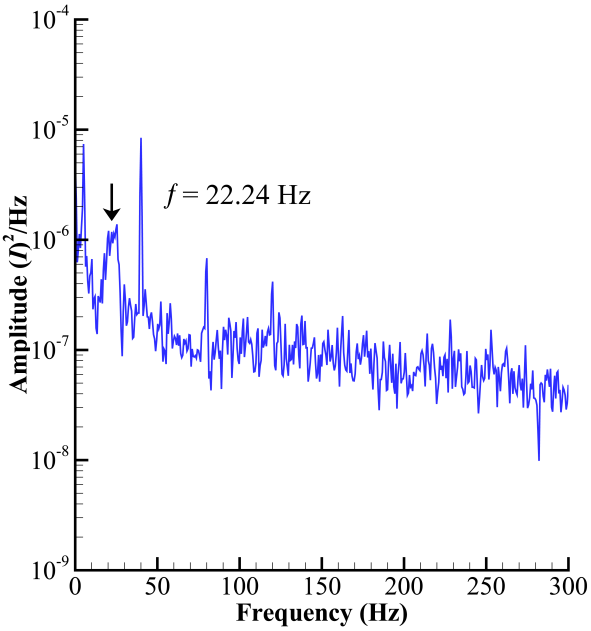

Figure 3.64: Power spectral density of shock oscillation up to 300 Hz for $M = 0.7$ and $\alpha = 2°$ suction case.

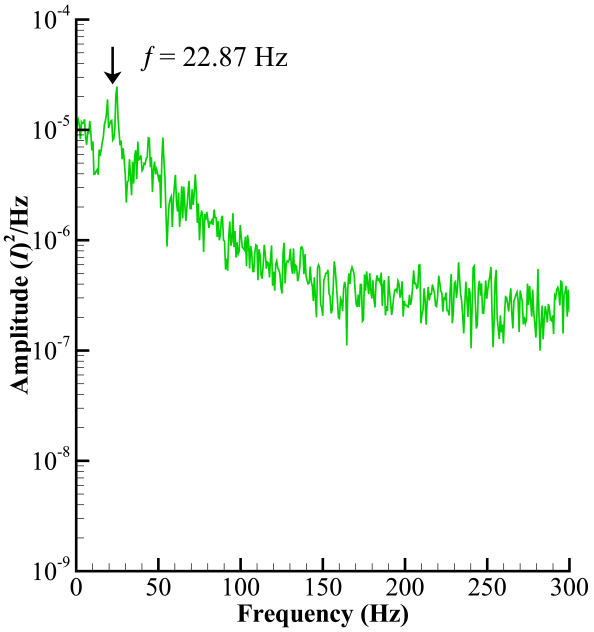

Figure 3.65: Power spectral density of shock oscillation up to 300 Hz for $M = 0.7$ and $\alpha = 1°$ no-suction case.

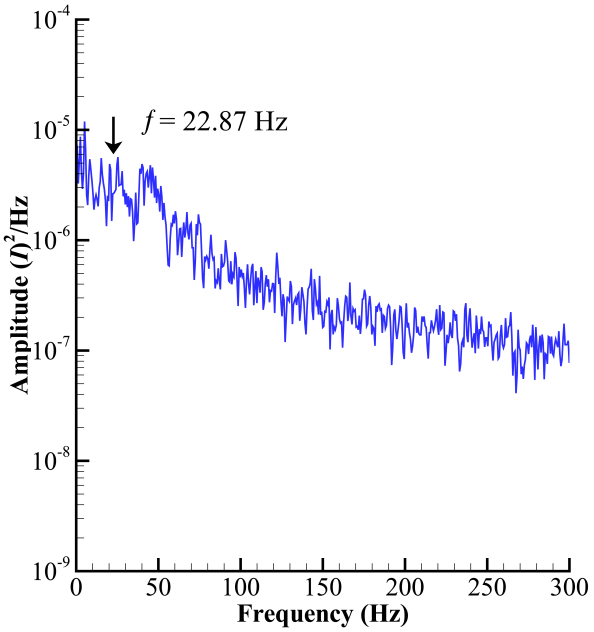

Figure 3.66: Power spectral density of shock oscillation up to 300 Hz for $M = 0.7$ and $\alpha = 1°$ suction case.

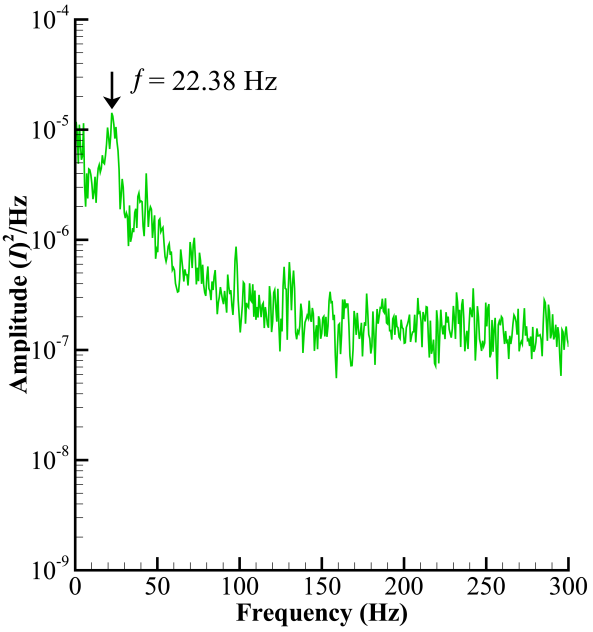

Figure 3.67: Power spectral density of shock oscillation up to 300 Hz for $M = 0.7$ and $\alpha = 0°$ no-suction case.

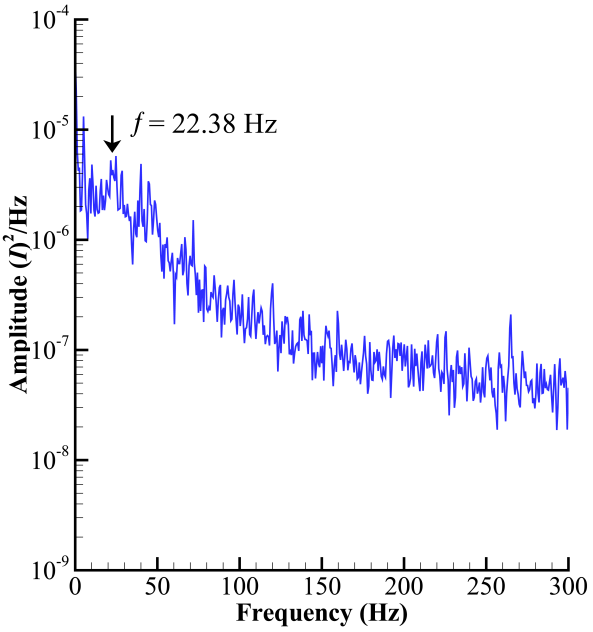

Figure 3.68: Power spectral density of shock oscillation up to 300 Hz for $M = 0.7$ and $\alpha = 0°$ suction case.

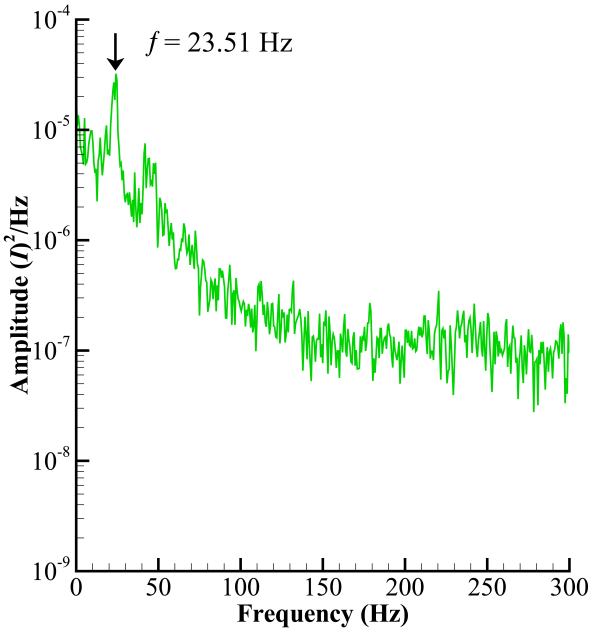

Figure 3.69: Power spectral density of shock oscillation up to 300 Hz for $M = 0.7$ and $\alpha = -1°$ no-suction case.

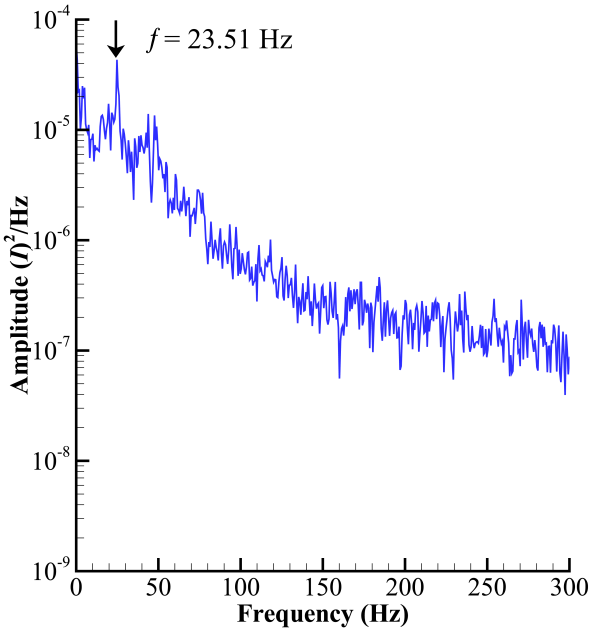

Figure 3.70: Power spectral density of shock oscillation up to 300 Hz for $M = 0.7$ and $\alpha = -1°$ suction case.

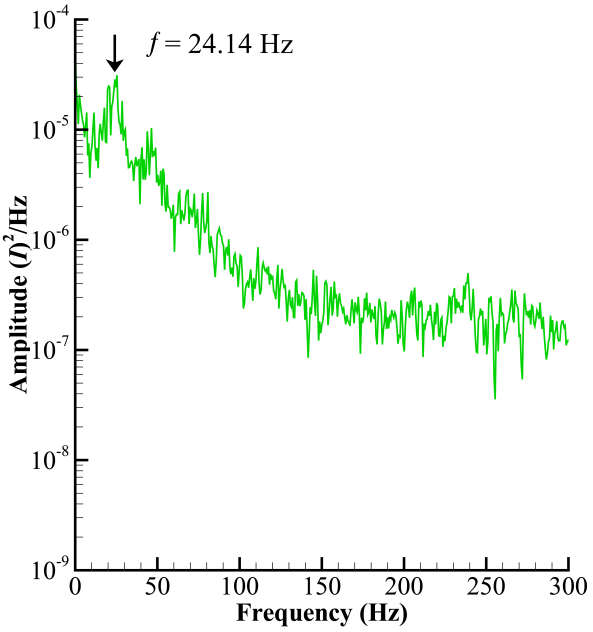

Figure 3.71: Power spectral density of shock oscillation up to 300 Hz for $M = 0.7$ and $\alpha = -2°$ no-suction case.

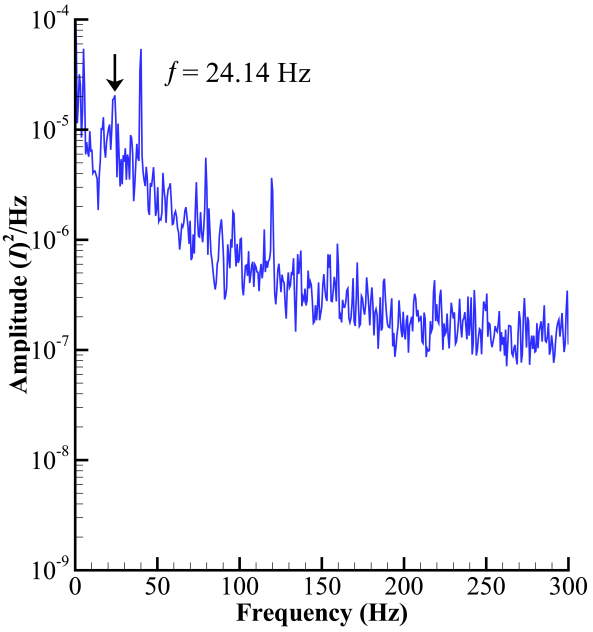

Figure 3.72: Power spectral density of shock oscillation up to 300 Hz for $M = 0.7$ and $\alpha = -2°$ suction case.

Chapter 4

Summary, Conclusions, and Recommendations

4.1 Summary

The experimental investigation performed for this study was executed at the transonic wind tunnel facility at the University of Illinois at Urbana-Champaign. It encompassed the analysis and characterization of a Griffith-type airfoil in a transonic flow field to assess its laminar flow capabilities in the presence of boundary layer-suction on the upper surface of the airfoil. The general performance of the airfoil was evaluated across a Mach number range of $M = 0.3 - 0.7$ and angle-of-attack range of α = -2° − 2°. Static pressure measurements were acquired across the upper and lower surfaces of the airfoil to obtain integral lift and moment coefficients. Stagnation and static pressure measurements were also acquired in the wake region of the airfoil from which profile drag data were obtained. In addition, PIV experiments in the near-wake region of the airfoil were performed to further characterize the effect of suction in the momentum-deficit alleviation in the off-body flow field. Flow visualization experiments were also performed to identify the suction influence on the boundary-layer transition characteristics of the airfoil. Lastly, Schlieren imaging diagnostics were used to analyze the effect of suction on the structure and stability of transonic shocks.

4.1.1 Airfoil Aerodynamic Performance

Suction Effect on Pressure Distributions

Suction was observed to have a beneficial impact in the C_p distributions across all Mach numbers and angles of attack tested by achieving lower C_p values across the upper surface, allowing for a more aggressive pressure recovery after the slot location and achieving higher trailing edge recovery pressures. At the design angle of attack of $\alpha = 0°$, the reductions in C_p were observed to begin around the $x/c = 0.35 - 0.40$ region and persisted until the slot location where values downstream of the $x/c = 0.90$ location were observed to

be greater as the pressure recovery was assisted by suction. However, for the $M = 0.7$ case, the suction influence on the C_p distribution was observed to occur further downstream of the local supersonic region at around the $x/c = 0.55$ location. This was identified to be related to a circulation-based effect in which, due to a local supersonic region, flow properties downstream cannot propagate upstream at the same velocity as in a subsonic flow and therefore do not have a first-order influence in the pressure characteristic of the airfoil near the leading edge.

When considering all of the angles of attack at $M = 0.7$, the initial pressure recovery region was observed to vary by approximately $5\%c$ between $\alpha = 2°$ and -2°. Stronger transonic shocks were also identified by abrupt and discrete increases in static pressures at the ends of the local supersonic regions of the airfoil at angles of attack of $\alpha = 1°$ and 2°. It was observed that under the influence of suction, the shock location moved downstream and the pressure rise across was reduced indicating a weaker shock structure.

Suction Effect on Aerodynamic Polars

The effect of suction on the lift-curve slope is seen to be constant across all Mach number conditions, shifting by a constant difference in C_l. The slope is seen to increase slightly with increasing Mach number, as was expected due to compressibility effects. The moment coefficient similarly shows a relatively constant shift under the influence of suction at all Mach numbers tested. Also, the moment coefficient is seen to decrease with increasing Mach number. Both of these behaviors in the C_m are due to the increased aft loading produced with the use of suction and higher velocities that can be observed in the pressure distributions.

Unlike the lift and moment coefficients, suction did not have a similar linear effect in the reduction of drag. With the exception of the $M = 0.3$ case, drag reductions were observed to be greatest at the higher angles of attack with some cases ($M = 0.6$ and 0.7) even showing increases in drag at lower angles of attack with suction applied. However, when comparing the suction and no-suction L/D parameter, performance benefits were observed across all conditions tested. In an effort to compare the aerodynamic performance gains from this technology, experiments were also conducted on a RAE 2822 airfoil under the same experimental conditions for which the drag polars are presented. When comparing the suction and RAE 2822 cases, a similar trend was observed in which the drag reductions increased with increases in angle of attack. This behavior is due to the fact that at the lower angles of attack the boundary layer across the upper surface is not subjected to significantly strong pressure gradients (when compared to higher angles of attack), and

hence the applied suction has limited influence on the reduction of the momemtum loss in the boundary layer.

At the design conditions of $M = 0.7$ and $\alpha = 0°$, a reduction in C_d of 10.70% and an increase in L/D of 14.68% were observed between the suction and no-suction cases. Similarly, for the RAE 2822 and suction cases a reduction in C_d of 6.94% and an increase in L/D of 7.33% were also observed. Tables 4.1 to 4.5 show a summary of the reductions in C_d and improved L/D performance at all angles of attack based on each Mach number tested.

Table 4.1: Aerodynamic performance summary for all angles of attack at M = 0.3.

α	Suction & No-Suction		Suction & RAE 2822	
	ΔC_d	$\Delta L/D$	ΔC_d	$\Delta L/D$
2°	-0.0018 (-26.47%)	45.28 (48.00%)	-0.0039 (-43.82%)	69.50 (99.15%)
1°	-0.0022 (-36.37%)	60.96 (66.61%)	-0.0036 (-48.65%)	84.23 (123.42%)
0°	-0.0021 (-31.81%)	37.28 (53.75%)	-0.0028 (-38.36%)	46.74 (78.06%)
-1°	-0.0025 (-32.05%)	28.05 (66.70%)	-0.0021 (-28.38%)	23.51 (50.47%)
-2°	-0.0022 (-27.16%)	16.30 (66.96%)	-0.0016 (-21.33%)	10.16 (33.32%)

Table 4.2: Aerodynamic performance summary for all angles of attack at M = 0.4.

α	Suction & No-Suction		Suction & RAE 2822	
	ΔC_d	$\Delta L/D$	ΔC_d	$\Delta L/D$
2°	-0.0039 (-48.75%)	98.19 (125.08%)	-0.0057 (-58.16%)	113.26 (178.56%)
1°	-0.0029 (-42.65%)	71.74 (90.95%)	-0.0035 (-47.30%)	79.70 (112.38%)
0°	-0.0019 (-27.14%)	30.80 (48.72%)	-0.0016 (-23.88%)	29.27 (45.21%)
-1°	-0.0015 (-20.27%)	20.00 (41.52%)	-0.0006 (-9.23%)	15.59 (29.66%)
-2°	-0.0017 (-21.52%)	17.78 (77.65%)	-0.0009 (-12.68%)	7.58 (22.91%)

Table 4.3: Aerodynamic performance summary for all angles of attack at M = 0.5.

α	Suction & No-Suction		Suction & RAE 2822	
	ΔC_d	$\Delta L/D$	ΔC_d	$\Delta L/D$
2°	-0.0027 (-33.75%)	50.25 (61.88%)	-0.0037 (-41.11%)	56.96 (76.48%)
1°	-0.0013 (-19.12%)	25.17 (30.40%)	-0.0019 (-25.68%)	36.22 (50.48%)
0°	-0.0014 (-20.29%)	21.37 (33.37%)	-0.0013 (-19.12%)	20.59 (31.76%)
-1°	-0.0008 (-11.76%)	8.72 (17.25%)	-0.0009 (-13.04%)	11.33 (23.65%)
-2°	-0.0011 (-14.86%)	17.79 (71.00%)	-0.0008 (-11.27%)	10.77 (33.58%)

Table 4.4: Aerodynamic performance summary for all angles of attack at M = 0.6.

α	Suction & No-Suction		Suction & RAE 2822	
	ΔC_d	$\Delta L/D$	ΔC_d	$\Delta L/D$
2°	-0.0016 (-19.28%)	24.49 (29.76%)	-0.0020 (-22.99%)	34.43 (47.58%)
1°	-0.0009 (-12.50%)	18.53 (23.76%)	-0.0011 (-14.86%)	26.37 (37.58%)
0°	-0.0010 (-13.70%)	14.05 (23.08%)	-0.0007 (-10.00%)	10.17 (15.71%)
-1°	-0.0007 (-9.33%)	8.07 (18.97%)	-0.0002 (-2.86%)	3.35 (7.09%)
-2°	-0.0004 (-5.26%)	8.15 (31.78%)	0.0002 (2.86%)	3.91 (13.08%)

Table 4.5: Aerodynamic performance summary for all angles of attack at M = 0.7.

α	Suction & No-Suction		Suction & RAE 2822	
	ΔC_d	$\Delta L/D$	ΔC_d	$\Delta L/D$
2°	-0.0016 (-20.25%)	27.37 (31.10%)	-0.0013 (-17.11%)	26.61 (29.97%)
1°	-0.0012 (-15.58%)	18.31 (24.69%)	-0.0010 (-13.33%)	18.10 (24.33%)
0°	-0.0008 (-10.67%)	8.64 (14.68%)	-0.0005 (-6.94%)	4.60 (7.33%)
-1°	0.0003 (3.95%)	0.77 (1.96%)	0.0007 (9.72%)	-4.99 (-11.06%)
-2°	0.0002 (2.47%)	6.20 (37.36%)	0.0004 (5.06%)	-0.51 (-2.17%)

Suction Effect on Wake Momentum Deficit

Averaged velocity flow fields in the wake region obtained from PIV data were presented for all Mach numbers at $\alpha = 0^\circ$ for both suction and no-suction cases. It was observed that for all Mach numbers the application of suction resulted in a noticeable increase in the velocity magnitude of the wake. For the design $M = 0.7$, a maximum normalized difference in velocity magnitude of approximately 0.16 was observed. This increase in velocity resulted in an momentum deficit alleviation across the wake which is related to the drag benefits observed at the design angle of attack of $\alpha = 0^\circ$ for all Mach number conditions. In addition, the effect of suction on the stronger pressure recovery region was also observed in the velocity flow field. This was qualitatively determined by the more rapid and distinct change in velocity gradients in the streamwise direction, as observed in the velocity flow field contour plots.

4.1.2 Transition Characteristics

To understand the transition and laminar flow characteristics of the airfoil, surface-oil flow visualization experiments were performed at all angle-of-attack cases for $M = 0.7$. It was observed for both suction and no-suction conditions that the airfoil experienced an extensive region of laminar flow up to the shock location. The laminar flow region was then followed by a pronounced laminar separation bubble which reattached further downstream. However, for the α = -1° and -2° suction cases, a distinct stagnation region characteristic of a laminar separation bubble was not observed. Hence, since the flow visualization images provide a time-averaged and qualitative representation of an unsteady process, a conclusive statement regarding the transition process could not be made. Therefore, the regions following the shock up to the slot location for these two angles were identified as low-shear regions according to experimental observations.

For the no-suction cases, the onset of the laminar separation bubble, corresponding to the averaged shock location, was observed to move downstream approximately $0.02c$ as the angle of attack was decreased by increments of 1°. As a result, the laminar flow runs are shock limited as transition is assumed to be produced by the shockwave boundary-layer interaction. The streamwise length of the laminar separation bubble was also decreased as the angle of attack was reduced, having a constant turbulent reattachment point at approximately $0.77c$. With the application of suction, the shock location was observed to remain fairly constant when compared to the no-suction cases, being further upstream at the lower angles of attack. A summary of the averaged shock locations obtained from the flow visualization data for both suction and

no-suction conditions is presented in Table 4.6.

Table 4.6: Averaged shock locations from flow visualization experiments for suction and no-suction cases.

α	No-Suction	Suction
2°	0.641c	0.661c
1°	0.662c	0.679c
0°	0.685c	0.689c
-1°	0.705c	0.692c
-2°	0.722c	0.699c

4.1.3 Transonic Shock Characteristics

Transonic shocks were observed for all angle-of-attack conditions at the $M = 0.7$ design case. Throughout the Schlieren experments, a low-frequency oscillatory process was identified for the shock build-up process which was characterized in three distinct phases. First, Mach waves were observed to begin forming on the upper surface of the airfoil. This wave-formation process led to to the fully-developed shock structure which was then observed to weaken and dissipate before the oscillation occurred again. This oscillatory process was related to a hysteresis feedback interaction common in airfoils operating at low-transonic Mach numbers. The application of suction to the airfoil did not alter the shock-formation process or frequency of oscillation; however, under suction conditions the fully-developed shock appeared further downstream with a well-defined lambda structure when compared to the no-suction cases.

The characteristic frequencies of the shock oscillatory process were obtained through a PSD analysis based on extracted pixel intensities from the Schlieren data. For the design conditions of $\alpha = 0°$ and $M = 0.7$, a characteristic frequency of 22.38 Hz was identified which showed excellent agreement with qualitative analysis of the data. It was observed that with the application of suction, the amplitude corresponding to this broadband peak was significantly reduced showing a beneficial influence on the stability of the oscillatory motion of the shock. Similar characteristic frequencies were also obtained for the other off-design angle-of-attack conditions. However, significant reductions in the PSD amplitudes were only observed at the higher angles of attack with no influence shown for the α = -1° and -2° cases. Averaged shock locations were also obtained from the Schlieren data which show good agreement with those obtained from flow visualization images. Table 4.7 shows a summary of the oscillatory frequencies and averaged shock locations obtained from Schlieren data.

Table 4.7: Shock oscillatory frequency and averaged shock location summary from Schlieren data at M = 0.7.

α	Frequency	Averaged Shock Location	
		No-Suction	Suction
2°	22.24 Hz	0.649c	0.670c
1°	22.87 Hz	0.668c	0.677c
0°	22.38 Hz	0.677c	0.686c
-1°	23.51 Hz	0.708c	0.693c
-2°	24.14 Hz	0.729c	0.695c

4.2 Conclusions

1. Suction allows for a more aggresive presure recovery at all conditions tested. This aggresive pressure recovery results from the unforced adverse pressure gradient region moving further downstream where pressures are observed to recover to overall higher values over a shorter distance.

2. The influence in the C_p distribution as a result of suction at the design condition of M = 0.7 was observed to occur over a shorter region and further downstream when compared to the lower Mach numbers. This characteristic was linked to a circulation-based effect common to transonic airfoils.

3. The C_l and C_m aerodynamic coefficients varied linearly with suction applied across the angle-of-attack range. The curves essentially increased in magnitude by a relatively constant value due to the lower C_p values achieved and increased aft loading under suction.

4. Drag benefits resulting from applied suction did not scale linearly with angle-of-attack variations, being greatest at the higher angles of attack. This shows that the application of suction has negligible influence on profile drag reductions at conditions where the boundary layer is not subjected to strong pressure gradients. However, improvements in the L/D characteristics of the airfoil can still be obtained due to notable increases in lift.

5. The laminar flow capabilities of the airfoil were observed to be limited by the presence of transonic shocks at the design M = 0.7 condition, which for most cases were followed by a laminar separation bubble region. Hence, the short increase in the laminar runs for the suction cases was due to the delay

of the unforced adverse pressure gradient region which in turn delayed the average shock location. The delay in the shock location resulted in a smaller separated region as the reattachment location was observed to remain constant. This behavior is related to the low-Reynolds number condition tested, since transition was predicted to occur further upstream at flight Reynolds numbers of commercial aircraft during the development of the airfoil.

6. Suction was found to stabilize the unsteady shock oscillatory process by reducing the amplitude and also resulted in shocks with well-defined lambda structures when fully developed. Similar to the drag performance, there was not a noticeable influence on the stability of the shock at the lower angles of attack. In addition, suction was found to decrease the pressure rise across the shock, which could result in reductions in wave drag resulting from a weaker shock structure.

4.3 Recommendations

In an effort to expand on the work resulting from this experimental investigation and to progress on the development of laminar-flow airfoil technology for transonic aircraft applications, the following recommendations are given:

1. The airfoil used in this study was originally intended to be used with a centrifugal blower which would route the air being pulled from the upper surface of the airfoil through the trailing edge. This addition of momentum in the wake has a thrust effect which further reduces the profile drag. Hence, experiments incorporating trailing edge ejection of the air mass being pulled from the upper surface should be performed at transonic speeds. This would potentially show drag reductions at the lower angles of attack where suction alone did not show improvements.

2. This airfoil technology showed good improvement in the L/D performance, ability to maintain laminar flow, and better shock characteristics in a two-dimensional flow field. However, the influence of boundary-layer suction should be tested in a three-dimensional wing geometry with moderate sweep. Testing in a representative transonic wing geometry will allow the airfoil to be evaluated under the influence of cross-flow instabilities resulting from sweep, and determine if the technology is able to show improvements in the laminar flow capabilities and overall wing performance.

3. When considering the implementation of this airfoil concept into an aircraft system, an equivalent drag penalty taking into account the tradeoffs between operational requirements and performance benefits obtained should be considered. In addition, the limitations in the performance envelope of an aircraft upon the failure of the suction/blowing system should also be considered during the design stage.

4. Since transition at transport-aircraft flight Reynolds numbers should occur farther upstream than the cases studied here, the effect of suction is envisaged as a method to extend the laminar flow region by significantly larger chordwise distances. Hence, further experimentation at higher Reynolds numbers should be performed to evaluate the aerodynamic performance improvements of this technology for applications in wing sections for transonic commercial-transport aircraft.

5. This airfoil concept offers a potential avenue to provide drag reductions and improved aerodynamic efficiency on HALE aircraft operating at similar Reynolds numbers (as those tested), transonic speeds, and high C_l values where the drag benefits were observed to be the greatest. Therefore, if special consideration is given to properly tailoring the pressure gradient and suction-pressure recovery, the laminar separation bubble that currently limits HALE airfoil performance can be eliminated and result in further drag reductions.

6. The stabilizing effect favorable pressure gradients have on boundary-layer transition encompasses a significant design consideration in which laminar boundary layers are desired to extend as far downstream as possible while being able to transition before the point where separation would occur across the transonic shock. Further investigation should follow in order to identify the effect of applied suction on the boundary-layer stability and transition behavior for these types of airfoils, allowing for an improved understanding of the natural tradeoff between the length of laminar flow produced and compressibility losses in the transonic regime.

7. Given that the implementation of this airfoil technology in an aircraft will depend on the use of external power sources and require redundancy, the use of passive flow control devices in airfoil designs to achieve transonic laminar flow should also be considered.

Appendix A

Power Spectral Density (PSD) Calculation

To characterize the frequencies of the oscillatory shock motions produced at the end of local sonic regions across the upper surface of the airfoil, a power spectral density analysis was performed as discussed in Section 2.5. This approach considers the distribution of energy in the frequency domain to determine the relevant frequency scales of a time-dependent measurement or signal [50]. The formulation included below is derived from that presented by Ansell [39] and by Bendat and Piersol [40]. In general, the distribution of energy in the frequency spectrum was obtained using standard fast Fourier transform (FFT) methods which are used to compute the discrete Fourier transform (DFT) of a signal at much greater speed when compared to standard DFT calculations [39]. This method is commonly used to estimate the spectral density in a signal [40].

The DFT of an unsteady signal can be described using Eq. (A.1).

$$X_k = \sum_{n=0}^{N-1} x_n e^{-i2\pi k \frac{n}{N}} \qquad k = 0, 1, 2, ..., N-1 \tag{A.1}$$

In the above equation, X_k corresponds to the transformed signal, $x_0, x_1, x_2, ..., x_{N-1}$ are complex numbers, and N is the number of data points in the DFT. The parameter k represents the discrete frequency values as shown in Eq. (A.2) where Δt corresponds to the temporal spacing between the data points.

$$f_k = \frac{k}{N\Delta t} \qquad k = 0, 1, 2, ..., N-1 \tag{A.2}$$

The power spectral density can be expressed as a function of the discrete frequencies obtained in Eq. (A.2) and using the DFT calculated from Eq. (A.1) as shown in Eq. (A.3) where E represents the expected value of the term in brackets. By using the PSD method presented here, the distribution of power was characterized across the frequency spectrum ranging from $f = 0$ Hz to the Nyquist limit of one-half of the sampling frequency [39, 40].

$$G_{xx}(f) = 2 \lim_{T \to \infty} \frac{1}{T} E\left[|X_k(f,T)|^2\right] \tag{A.3}$$

The actual calculation for the PSD was performed using an ensemble average of data points for which N_s, being the number of data samples in the signal, and N_{ens}, being the number of realizations for the ensemble average, were defined. The realizations used were extracted from the raw signal S acquired during the experiment, according to the number of realizations N_{ens} as shown in Eq. (A.4).

$$S_{ens} = S\left(\left((i-1)\frac{N_s}{N_{esb}} + 1\right) : \left(i\frac{N_s}{N_{esb}}\right)\right) \qquad i = 0, 1, 2, ..., N_{ens} \tag{A.4}$$

The DFT in Eq. (A.1) is then calculated using an FFT for each of the S_{ens} sets obtained. The calculation of the PSD for each DFT obtained is performed using a modification of Eq. (A.3) considering the number of realizations as shown in Eq. (A.5).

$$G_{xxi} = 2\frac{F_s N_s}{N_{ens}} |X_{ki}|^2 \qquad i = 0, 1, 2, ..., N_{ens} \tag{A.5}$$

The RMS average of the extracted PSDs was then calculated as shown in Eq. (A.6) and plotted against the frequency distribution corresponding to the number of realizations and the Nyquist limit as shown in Eq. (A.7).

$$G_{xx} = \sqrt{{N_{ens}}^{-1} \sum_{i=1}^{N_{ens}} {G_{xx}}_i^2} \tag{A.6}$$

$$f = \left(0 : \frac{F_s N_s}{N_{ens}} : \frac{F_s}{2}\right) \tag{A.7}$$

Appendix B

Uncertainty Analysis

As with all experimental studies, the data obtained were associated with some uncertainties that must be characterized to allow for proper interpretation of the acquired results. Bias errors, related to the uncertainty in measurement capabilities or accuracy of an instrument, were determined using the methods presented by Coleman and Steele [51] and Kline and McClintock [52]. The uncertainty in the velocity flow field obtained through PIV was determined using the LaVision DaVis V8.3 software which is based on the methods presented by Neal et al. [53], Sciacchitano et al. [54], and Wieneke [55].

To obtain the uncertainty of a calculated parameter, the uncertainty of every measurement that was used in the calculation has to be considered individually. For instance, a general parameter (p) depends on n number of measured quantities as seen in Eq. (B.1).

$$p = p(x_1, x_2, x_3, ..., x_n) \tag{B.1}$$

The uncertainty of p can be calculated using Eq. (B.2), where U is the uncertainty value.

$$U_p = \sqrt{\left(\frac{\partial p}{\partial x_1} U_{x_1}\right)^2 + \left(\frac{\partial p}{\partial x_2} U_{x_2}\right)^2 + \left(\frac{\partial p}{\partial x_3} U_{x_3}\right)^2 + ... + \left(\frac{\partial p}{\partial x_n} U_{x_n}\right)^2} \tag{B.2}$$

The following subsections show in detail the uncertainty derivation for each calculated experimental parameter presented in this study. Sample uncertainty values calculated for each parameter at an arbitrary test condition are also shown.

B.1 Pressure Coefficient (C_p) Uncertainty

The pressure coefficient was calculated using Eq. (B.3), where ΔP was directly measured form the PSI pressure scanners and P_0 and P_∞ were measured from OMEGA® pressure transducers as discussed in

Chapter 2.

$$C_p = \frac{P - P_\infty}{q_\infty} = \frac{\Delta P}{P_0 - P_\infty} \tag{B.3}$$

Using Eq. (B.2), the uncertainty for C_p becomes Eq. (B.4).

$$U_{C_p} = \sqrt{\left(\frac{\partial C_p}{\partial \Delta P} U_{\Delta P}\right)^2 + \left(\frac{\partial C_p}{\partial P_0} U_{P_0}\right)^2 + \left(\frac{\partial C_p}{\partial P_\infty} U_{P_\infty}\right)^2} \tag{B.4}$$

From Eq. (B.3), the partial derivatives in Eq. (B.4) result in Eqs. (B.5) to (B.7).

$$\frac{\partial C_p}{\partial \Delta P} = \frac{1}{q_\infty} \tag{B.5}$$

$$\frac{\partial C_p}{\partial P_0} = \frac{\text{-}\Delta P}{q_\infty^2} \tag{B.6}$$

$$\frac{\partial C_p}{\partial P_\infty} = \frac{\Delta P}{q_\infty^2} \tag{B.7}$$

B.2 Lift Coefficient (C_l) Uncertainty

The lift coefficient was calculated using Eq. (B.8) where C_n is the normal force coefficient, C_a is the axial force coefficient, and α is the angle of attack as discussed in Chapter 2.

$$C_l = c_n \cos(\alpha) - c_a \sin(\alpha) \tag{B.8}$$

Using Eq. (B.2), the uncertainty for C_l becomes Eq. (B.9).

$$U_{C_l} = \sqrt{\left(\frac{\partial C_l}{\partial C_n} U_{C_n}\right)^2 + \left(\frac{\partial C_l}{\partial C_a} U_{C_a}\right)^2 + \left(\frac{\partial C_l}{\partial \alpha} U_\alpha\right)^2} \tag{B.9}$$

From Eq. (B.8), the partial derivatives in Eq. (B.9) result in Eqs. (B.10) to (B.12).

$$\frac{\partial C_l}{\partial C_n} = \cos(\alpha) \tag{B.10}$$

$$\frac{\partial C_l}{\partial C_a} = -\sin(\alpha) \tag{B.11}$$

$$\frac{\partial C_l}{\partial \alpha} = -\left[C_n \sin(\alpha) + C_a \cos(\alpha)\right] \tag{B.12}$$

Since C_n and C_a are calculated values, their respective uncertainties U_{C_n} and U_{C_a} must be calculated as well. Considering first the normal force coefficient, C_n was calculated using Eq. (B.13) as discussed in Chapter 2 where the subscripts u and l correspond to upper and lower surfaces and the distribution of pressure taps is considered in the summations.

$$C_n = \sum_{i=1}^{N_l} C_{P_l} dx - \sum_{i=1}^{N_u} C_{P_u} dx \tag{B.13}$$

The actual calculation of C_n from the C_p values calculated at each pressure tap was performed using the trapezoidal rule; hence, Eq. (B.13) can also be expressed as Eq. (B.14) where the x locations are normalized by the airfoil chord.

$$C_n = \sum_{i=1}^{N_l-1} \frac{\left(C_{p_{li}} + C_{p_{li+1}}\right)}{2} \left(x_{li+1} - x_{li}\right) - \sum_{i=1}^{N_u-1} \frac{\left(C_{p_{ui}} + C_{p_{ui+1}}\right)}{2} \left(x_{ui+1} - x_{ui}\right) \tag{B.14}$$

Using Eq. (B.2), the uncertainty for C_n becomes Eq. (B.15).

$$\begin{aligned} U_{C_n} = \Bigg[&\left(\frac{\partial C_n}{\partial C_{p_{li}}} U_{C_{p_{li}}}\right)^2 + \left(\frac{\partial C_n}{\partial C_{p_{li+1}}} U_{C_{p_{li+1}}}\right)^2 + \left(\frac{\partial C_n}{\partial C_{p_{ui}}} U_{C_{p_{ui}}}\right)^2 + \left(\frac{\partial C_n}{\partial C_{p_{ui+1}}} U_{C_{p_{ui+1}}}\right)^2 + \\ &\left(\frac{\partial C_n}{\partial x_{li+1}} U_{x_{li+1}}\right)^2 + \left(\frac{\partial C_n}{\partial x_{li}} U_{x_{li}}\right)^2 + \left(\frac{\partial C_n}{\partial x_{ui+1}} U_{x_{ui+1}}\right)^2 + \left(\frac{\partial C_n}{\partial x_{ui}} U_{x_{ui}}\right)^2 \Bigg]^{\frac{1}{2}} \end{aligned} \tag{B.15}$$

From Eq. (B.14), the partial derivatives in Eq. (B.15) result in Eqs. (B.16) to (B.23).

$$\frac{\partial C_n}{\partial C_{p_{li}}} = \sum_{i=1}^{N_l-1} \frac{\left(x_{li+1} - x_{li}\right)}{2} \tag{B.16}$$

$$\frac{\partial C_n}{\partial C_{p_{li+1}}} = \sum_{i=1}^{N_l-1} \frac{\left(x_{li+1} - x_{li}\right)}{2} \tag{B.17}$$

$$\frac{\partial C_n}{\partial C_{p_{ui}}} = - \sum_{i=1}^{N_u-1} \frac{(x_{ui+1} - x_{ui})}{2} \tag{B.18}$$

$$\frac{\partial C_n}{\partial C_{p_{ui+1}}} = - \sum_{i=1}^{N_u-1} \frac{(x_{ui+1} - x_{ui})}{2} \tag{B.19}$$

$$\frac{\partial C_n}{\partial x_{li+1}} = \sum_{i=1}^{N_l-1} \frac{\left(C_{p_{li}} + C_{p_{li+1}}\right)}{2} \tag{B.20}$$

$$\frac{\partial C_n}{\partial x_{li}} = - \sum_{i=1}^{N_l-1} \frac{\left(C_{p_{li}} + C_{p_{li+1}}\right)}{2} \tag{B.21}$$

$$\frac{\partial C_n}{\partial x_{ui+1}} = - \sum_{i=1}^{N_u-1} \frac{\left(C_{p_{ui}} + C_{p_{ui+1}}\right)}{2} \tag{B.22}$$

$$\frac{\partial C_n}{\partial x_{ui}} = \sum_{i=1}^{N_u-1} \frac{\left(C_{p_{ui}} + C_{p_{ui+1}}\right)}{2} \tag{B.23}$$

Similar to C_n, the axial force coefficient produced by the airfoil C_a was calculated using Eq. (B.24) which by using the trapezoidal rule simplified to Eq. (B.25).

$$C_a = \sum_{i=1}^{N_u} C_{P_u} \frac{dy_u}{dx} dx - \sum_{i=1}^{N_l} C_{P_l} \frac{dy_l}{dx} dx \tag{B.24}$$

$$C_a = \sum_{i=1}^{N_u-1} \frac{\left(C_{p_{ui}} + C_{p_{ui+1}}\right)}{2} (y_{ui+1} - y_{ui}) - \sum_{i=1}^{N_l-1} \frac{\left(C_{p_{li}} + C_{p_{li+1}}\right)}{2} (y_{li+1} - y_{li}) \tag{B.25}$$

Using Eq. (B.2), the uncertainty for C_a becomes Eq. (B.26).

$$\begin{aligned} U_{C_a} = \Bigg[& \left(\frac{\partial C_a}{\partial C_{p_{ui}}} U_{C_{p_{ui}}}\right)^2 + \left(\frac{\partial C_a}{\partial C_{p_{ui+1}}} U_{C_{p_{ui+1}}}\right)^2 + \left(\frac{\partial C_a}{\partial C_{p_{li}}} U_{C_{p_{li}}}\right)^2 + \left(\frac{\partial C_a}{\partial C_{p_{li+1}}} U_{C_{p_{li+1}}}\right)^2 + \\ & \left(\frac{\partial C_a}{\partial y_{ui+1}} U_{y_{ui+1}}\right)^2 + \left(\frac{\partial C_a}{\partial y_{ui}} U_{y_{ui}}\right)^2 + \left(\frac{\partial C_a}{\partial y_{li+1}} U_{y_{li+1}}\right)^2 + \left(\frac{\partial C_a}{\partial y_{li}} U_{y_{li}}\right)^2 \Bigg]^{\frac{1}{2}} \end{aligned} \tag{B.26}$$

From Eq. (B.25), the partial derivatives in Eq. (B.26) result in Eqs. (B.27) to (B.34).

$$\frac{\partial C_a}{\partial C_{p_{ui}}} = \sum_{i=1}^{N_u-1} \frac{(y_{ui+1} - y_{ui})}{2} \tag{B.27}$$

$$\frac{\partial C_s}{\partial C_{p_{ui+1}}} = \sum_{i=1}^{N_u-1} \frac{(y_{ui+1} - y_{ui})}{2} \tag{B.28}$$

$$\frac{\partial C_a}{\partial C_{p_{li}}} = - \sum_{i=1}^{N_l-1} \frac{(y_{li+1} - y_{li})}{2} \tag{B.29}$$

$$\frac{\partial C_a}{\partial C_{p_{li+1}}} = - \sum_{i=1}^{N_l-1} \frac{(y_{li+1} - y_{li})}{2} \tag{B.30}$$

$$\frac{\partial C_a}{\partial y_{ui+1}} = \sum_{i=1}^{N_u-1} \frac{\left(C_{p_{ui}} + C_{p_{ui+1}}\right)}{2} \tag{B.31}$$

$$\frac{\partial C_a}{\partial y_{ui}} = - \sum_{i=1}^{N_u-1} \frac{\left(C_{p_{ui}} + C_{p_{ui+1}}\right)}{2} \tag{B.32}$$

$$\frac{\partial C_a}{\partial y_{li+1}} = - \sum_{i=1}^{N_l-1} \frac{\left(C_{p_{li}} + C_{p_{li+1}}\right)}{2} \tag{B.33}$$

$$\frac{\partial C_a}{\partial y_{li}} = \sum_{i=1}^{N_l-1} \frac{\left(C_{p_{li}} + C_{p_{li+1}}\right)}{2} \tag{B.34}$$

B.3 Moment Coefficient (C_m) Uncertainty

The moment coefficient about the quarter-chord location was calculated using Eq. (B.35) where C_{mLE} is the moment coefficient about the leading edge of the airfoil as discussed in Chapter 2.

$$C_m = C_{mLE} + \frac{1}{4} C_l \tag{B.35}$$

Using Eq. (B.2), the uncertainty for C_m becomes Eq. (B.36).

$$U_{C_m} = \sqrt{\left(\frac{\partial C_m}{\partial C_{mLE}} U_{C_{mLE}}\right)^2 + \left(\frac{\partial C_m}{\partial C_l} U_{C_l}\right)^2} \tag{B.36}$$

From Eq. (B.35), the partial derivatives in Eq. (B.36) result in Eqs. (B.37) and (B.38).

$$\frac{\partial C_m}{\partial C_{mLE}} = 1 \tag{B.37}$$

$$\frac{\partial C_m}{\partial C_l} = \frac{1}{4} \tag{B.38}$$

Since C_{mLE} and C_l are calculated values, their respective uncertainties $U_{C_{mLE}}$ and U_{C_l} must be calculated as well. The uncertainty for C_l is already derived in Appendix B.2. Considering the moment coefficient about the leading edge, C_{mLE} was calculated using Eq. (B.39) as discussed in Chapter 2 where the subscripts u and l correspond to upper and lower surfaces and the distribution of pressure taps is distributed in the summations.

$$C_{mLE} = \sum_{i=1}^{N_u} C_{P_u} x_u dx - \sum_{i=1}^{N_l} C_{P_l} x_l dx + \sum_{i=1}^{N_u} C_{P_u} \frac{d_{yu}}{dx} y_u dx - \sum_{i=1}^{N_l} C_{P_l} \frac{d_{yl}}{dx} y_l dx \tag{B.39}$$

The actual calculation of C_{mLE} from the C_p values calculated at each pressure tap was performed using the trapezoidal rule; hence, Eq. (B.39) can also be expressed as Eq. (B.40) where the x and y locations are normalized by the airfoil chord.

$$\begin{aligned} C_{mLE} = &\sum_{i=1}^{N_u-1} \frac{\left(C_{p_{ui}} + C_{p_{ui+1}}\right)}{2} \left(x_{ui+1} - x_{ui}\right) x_{uk} - \sum_{i=1}^{N_l-1} \frac{\left(C_{p_{li}} + C_{p_{li+1}}\right)}{2} \left(x_{li+1} - x_{li}\right) x_{lk} + \ldots \\ &\sum_{i=1}^{N_u-1} \frac{\left(C_{p_{ui}} + C_{p_{ui+1}}\right)}{2} \left(y_{ui+1} - y_{ui}\right) y_{uk} - \sum_{i=1}^{N_l-1} \frac{\left(C_{p_{li}} + C_{p_{li+1}}\right)}{2} \left(y_{li+1} - y_{li}\right) y_{lk} \end{aligned} \tag{B.40}$$

Using Eq. (B.2), the uncertainty for C_{mLE} becomes Eq. (B.41).

$$\begin{aligned} U_{C_{mLE}} = \Bigg[&\left(\frac{\partial C_{mLE}}{\partial C_{p_{ui}}} U_{C_{p_{ui}}}\right)^2 + \left(\frac{\partial C_{mLE}}{\partial C_{p_{ui+1}}} U_{C_{p_{ui+1}}}\right)^2 + \left(\frac{\partial C_{mLE}}{\partial x_{ui+1}} U_{x_{ui+1}}\right)^2 + \left(\frac{\partial C_{mLE}}{\partial x_{ui}} U_{x_{ui}}\right)^2 + \ldots \\ &\left(\frac{\partial C_{mLE}}{\partial C_{p_{li}}} U_{C_{p_{li}}}\right)^2 + \left(\frac{\partial C_{mLE}}{\partial C_{p_{li+1}}} U_{C_{p_{li+1}}}\right)^2 + \left(\frac{\partial C_{mLE}}{\partial x_{li+1}} U_{x_{li+1}}\right)^2 + \left(\frac{\partial C_{mLE}}{\partial x_{li}} U_{x_{li}}\right)^2 + \ldots \\ &\left(\frac{\partial C_{mLE}}{\partial y_{ui+1}} U_{y_{ui+1}}\right)^2 + \left(\frac{\partial C_{mLE}}{\partial y_{ui}} U_{y_{ui}}\right)^2 + \left(\frac{\partial C_{mLE}}{\partial y_{li+1}} U_{y_{li+1}}\right)^2 + \left(\frac{\partial C_{mLE}}{\partial y_{li}} U_{y_{li}}\right)^2 + \ldots \\ &\left(\frac{\partial C_{mLE}}{\partial x_{uk}} U_{x_{uk}}\right)^2 + \left(\frac{\partial C_{mLE}}{\partial x_{lk}} U_{x_{lk}}\right)^2 + \left(\frac{\partial C_{mLE}}{\partial y_{uk}} U_{y_{uk}}\right)^2 + \left(\frac{\partial C_{mLE}}{\partial y_{lk}} U_{y_{lk}}\right)^2 \Bigg]^{\frac{1}{2}} \end{aligned} \tag{B.41}$$

From Eq. (B.40), the partial derivatives in Eq. (B.41) result in Eqs. (B.42) to (B.57).

$$\frac{\partial C_{mLE}}{\partial C_{p_{ui}}} = \sum_{i=1}^{N_u-1} \frac{(x_{ui+1} - x_{ui})}{2} x_{uk} + \sum_{i=1}^{N_u-1} \frac{(y_{ui+1} - y_{ui})}{2} y_{uk} \tag{B.42}$$

$$\frac{\partial C_{mLE}}{\partial C_{p_{ui+1}}} = \sum_{i=1}^{N_u-1} \frac{(x_{ui+1} - x_{ui})}{2} x_{uk} + \sum_{i=1}^{N_u-1} \frac{(y_{ui+1} - y_{ui})}{2} y_{uk} \tag{B.43}$$

$$\frac{\partial C_{mLE}}{\partial x_{ui+1}} = \sum_{i=1}^{N_u-1} \frac{\left(C_{p_{ui}} + C_{p_{ui+1}}\right)}{2} x_{uk} \tag{B.44}$$

$$\frac{\partial C_{mLE}}{\partial x_{ui}} = - \sum_{i=1}^{N_u-1} \frac{\left(C_{p_{ui}} + C_{p_{ui+1}}\right)}{2} x_{uk} \tag{B.45}$$

$$\frac{\partial C_{mLE}}{\partial C_{p_{li}}} = - \sum_{i=1}^{N_l-1} \frac{(x_{li+1} - x_{li})}{2} x_{lk} - \sum_{i=1}^{N_l-1} \frac{(y_{li+1} - y_{li})}{2} y_{lk} \tag{B.46}$$

$$\frac{\partial C_{mLE}}{\partial C_{p_{li+1}}} = - \sum_{i=1}^{N_l-1} \frac{(x_{li+1} - x_{li})}{2} x_{lk} - \sum_{i=1}^{N_l-1} \frac{(y_{li+1} - y_{li})}{2} y_{lk} \tag{B.47}$$

$$\frac{\partial C_{mLE}}{\partial x_{li+1}} = - \sum_{i=1}^{N_l-1} \frac{\left(C_{p_{li}} + C_{p_{li+1}}\right)}{2} x_{lk} \tag{B.48}$$

$$\frac{\partial C_{mLE}}{\partial x_{li}} = \sum_{i=1}^{N_l-1} \frac{\left(C_{p_{li}} + C_{p_{li+1}}\right)}{2} x_{lk} \tag{B.49}$$

$$\frac{\partial C_{mLE}}{\partial y_{ui+1}} = \sum_{i=1}^{N_u-1} \frac{\left(C_{p_{ui}} + C_{p_{ui+1}}\right)}{2} y_{uk} \tag{B.50}$$

$$\frac{\partial C_{mLE}}{\partial y_{ui}} = - \sum_{i=1}^{N_u-1} \frac{\left(C_{p_{ui}} + C_{p_{ui+1}}\right)}{2} y_{uk} \tag{B.51}$$

$$\frac{\partial C_{mLE}}{\partial y_{li+1}} = - \sum_{i=1}^{N_l-1} \frac{\left(C_{p_{li}} + C_{p_{li+1}}\right)}{2} y_{lk} \tag{B.52}$$

$$\frac{\partial C_{mLE}}{\partial y_{li}} = \sum_{i=1}^{N_l-1} \frac{\left(C_{p_{li}} + C_{p_{li+1}}\right)}{2} y_{lk} \tag{B.53}$$

$$\frac{\partial C_{mLE}}{\partial x_{uk}} = \sum_{i=1}^{N_u-1} \frac{\left(C_{p_{ui}} + C_{p_{ui+1}}\right)}{2} \left(x_{ui+1} - x_{ui}\right) \tag{B.54}$$

$$\frac{\partial C_{mLE}}{\partial x_{uk}} = \sum_{i=1}^{N_l-1} \frac{\left(C_{p_{li}} + C_{p_{li+1}}\right)}{2} \left(x_{li+1} - x_{li}\right) \tag{B.55}$$

$$\frac{\partial C_{mLE}}{\partial y_{uk}} = \sum_{i=1}^{N_u-1} \frac{\left(C_{p_{ui}} + C_{p_{ui+1}}\right)}{2} \left(y_{ui+1} - y_{ui}\right) \tag{B.56}$$

$$\frac{\partial C_{mLE}}{\partial y_{lk}} = \sum_{i=1}^{N_l-1} \frac{\left(C_{p_{li}} + C_{p_{li+1}}\right)}{2} \left(y_{li+1} - y_{li}\right) \tag{B.57}$$

B.4 Drag Coefficient (C_d) Uncertainty

The profile drag coeffient was calculated using Eq. (B.58) where N referes to the number locations for which pressure data was collected in the wake which varied among experimental cases and dy is the traverse displacement between pressure survey locations. The term $C_d{}'$ is defined in Eq. (B.59) and discussed in Chapter 2 where P_0 and P correspond to stagnation and static pressures respectively and the subscripts ∞ and 1 indicate freestream and wake survey locations. As discussed in Chapter 2, the freestream pressure data were obtained using the OMEGA® pressure transducers and the pressure data at the wake were obtained through the PSI NetScanner system.

$$C_d = \sum_{i=1}^{N} C_d{}' dy \tag{B.58}$$

$$C_d{}' = 2\left(\frac{P_{0,1}}{P_{0,\infty}}\right)^{\frac{\gamma-1}{\gamma}} \left(\frac{P_1}{P_\infty}\right)^{\frac{1}{\gamma}} \left\{\frac{1-\left(\frac{P_1}{P_{0,1}}\right)^{\frac{\gamma-1}{\gamma}}}{1-\left(\frac{P_\infty}{P_{0,\infty}}\right)^{\frac{\gamma-1}{\gamma}}}\right\}^{\frac{1}{2}} \left[1-\left\{\frac{1-\left(\frac{P_\infty}{P_{0,1}}\right)^{\frac{\gamma-1}{\gamma}}}{1-\left(\frac{P_\infty}{P_{0,\infty}}\right)^{\frac{\gamma-1}{\gamma}}}\right\}^{\frac{1}{2}}\right] \tag{B.59}$$

The actual calculation of C_d from the $C_d{}'$ calculated at each wake survey location was performed using the trapezoidal rule; hence, Eq. (B.58) can also be expressed as Eq. (B.60).

$$C_d = \sum_{i=1}^{N-1} \frac{\left(C_{d_i}' + C_{d_{i+1}}'\right)}{2} dy \tag{B.60}$$

Using Eq. (B.2), the uncertainty for C_d becomes Eq. (B.61).

$$U_{C_d} = \sqrt{\left(\frac{\partial C_d}{\partial C_{d_i}'} U_{C_{d_i}'}\right)^2 + \left(\frac{\partial C_d}{\partial C_{d_{i+1}}'} U_{C_{d_{i+1}}'}\right)^2 + \left(\frac{\partial C_d}{\partial dy} U_{dy}\right)^2} \tag{B.61}$$

From Eq. (B.60), the partial derivatives in Eq. (B.61) result in Eqs. (B.62) to (B.64).

$$\frac{\partial C_d}{\partial C_{d_i}'} = \sum_{i=1}^{N-1} \frac{dy}{2} \tag{B.62}$$

$$\frac{\partial C_d}{\partial C_{d_{i+1}}'} = \sum_{i=1}^{N-1} \frac{dy}{2} \tag{B.63}$$

$$\frac{\partial C_d}{\partial dy} = \sum_{i=1}^{N-1} \frac{\left(C_{d_i}' + C_{d_{i+1}}'\right)}{2} \tag{B.64}$$

Since $C_d{}'$ is a calculated value, its respective uncertainty $U_{C_d{}'}$ must be calculated as well. Using Eq. (B.2) the uncertainty for $C_d{}'$ becomes Eq. (B.65).

$$U_{C_d{}'} = \sqrt{\left(\frac{\partial C_d{}'}{\partial P_{0,1}} U_{P_{0,1}}\right)^2 + \left(\frac{\partial C_d{}'}{\partial P_{0,\infty}} U_{P_{0,\infty}}\right)^2 + \left(\frac{\partial C_d{}'}{\partial P_1} U_{P_1}\right)^2 + \left(\frac{\partial C_d{}'}{\partial P_\infty} U_{P_\infty}\right)^2} \tag{B.65}$$

The corresponding partial derivative terms in Eq. (B.65) were calculated analytically from Eq. (B.59) using MATLAB®.

B.5 Mach Number (M) Uncertainty

The Mach number was calculated using Eq. (B.66), where P_0 and P were measured from the OMEGA® pressure transducers as discussed in Chapter 2.

$$M = \sqrt{\left(\left(\frac{P_0}{P}\right)^{0.285714} - 1\right) 5} \tag{B.66}$$

Using Eq. (B.2), the uncertainty for M becomes Eq. (B.67).

$$U_M = \sqrt{\left(\frac{\partial M}{\partial P_0} U_{P_0}\right)^2 + \left(\frac{\partial M}{\partial P} U_P\right)^2} \tag{B.67}$$

From Eq. (B.66), the partial derivatives in Eq. (B.67) result in Eqs. (B.68) and (B.69).

$$\frac{\partial M}{\partial P_0} = \frac{0.31944\sqrt{P^{0.285714}}}{{P_0}^{0.714286} P^{0.285714}\sqrt{{P_0}^{0.285714} - P^{0.285714}}} \tag{B.68}$$

$$\frac{\partial M}{\partial P} = \frac{\text{-}0.31944{P_0}^{0.285714}\sqrt{P^{0.285714}}}{P^{1.285714}\sqrt{{P_0}^{0.285714} - P^{0.285714}}} \tag{B.69}$$

B.6 Lift-to-Drag Ratio (L/D) Uncertainty

The lift-to-drag ratio was calculated using Eq. (B.70), where C_l and C_d are calculated parameters and their respective uncertainties are derived in Appendices B.2 and B.4.

$$\frac{L}{D} = \frac{C_l}{C_d} \tag{B.70}$$

Using Eq. (B.2), the uncertainty for L/D becomes Eq. (B.71).

$$U_{L/D} = \sqrt{\left(\frac{\partial \frac{L}{D}}{\partial C_l} U_{C_l}\right)^2 + \left(\frac{\partial \frac{L}{D}}{\partial C_d} U_{C_d}\right)^2} \tag{B.71}$$

From Eq. (B.70), the partial derivatives in Eq. (B.71) result in Eqs. (B.72) and (B.73).

$$\frac{\partial \frac{L}{D}}{\partial C_l} = \frac{1}{C_d} \tag{B.72}$$

$$\frac{\partial \frac{L}{D}}{\partial C_d} = \text{-}\frac{C_l}{{C_d}^2} \tag{B.73}$$

B.7 Sample Uncertainty Results

Sample uncertainty results are presented in Table B.1 for the different aerodynamic coefficients and wind tunnel experimental measurements based on calculations from the derived uncertainties in this appendix. In addition, uncertainty values for averaged PIV velocity components obtained using the LaVision DaVis V8.3 software as discussed in Chapter 2 are presented. The uncertainty values shown are representative of the Griffith-type transonic, laminar-flow airfoil at the design conditions of $M = 0.7$ and $\alpha = 0^\circ$ without suction

being applied.

Table B.1: Example of uncertainties for experimental measurements at $M = 0.7$, $\alpha = 0°$, and no-suction.

Parameter	Reference Value	Absolute Uncertainty	Relative Uncertainty (%)
C_p $(x/c = 0.50)$	-0.81092	±0.00183	±0.22573
C_l	0.44051	±0.01403	±3.18419
C_d	0.01410	$\pm 2.7868e^{-5}$	±0.19765
C_m	-0.11496	±0.01105	±9.61240
M	0.69959	$\pm 7.9104e^{-5}$	±0.11307
L/D	31.24157	±0.99671	±3.19035
u (PIV)	241.89625 m/s	±8.34302 m/s	±3.44901
v (PIV)	241.89625 m/s	±8.38779 m/s	±3.46752

References

[1] D. M. Somers, "Design of a Slotted, Natural-Laminar-Flow Airfoil for Business-Jet Applications," NASA CR-2012-217559, 2012.

[2] D. M. Somers, "An Exploratory Investigation of a Slotted, Natural-Laminar-Flow Airfoil," NASA CR-2012-217560, 2012.

[3] R. L. Campbell and M. N. Lynde, "Building a Practical Natural Laminar Flow Design Capability," AIAA Paper 2017-3059, 2017.

[4] M. N. Lynde and R. L. Campbell, "Computational Design and Analysis of a Transonic Natural Laminar Flow Wing for a Wind Tunnel Model," AIAA Paper 2017-3058, 2017.

[5] J. D. Crouch, "Boundary-Layer Transition Prediction for Laminar Flow Control," AIAA Paper 2015-2472, 2015.

[6] M. D. Maughmer and D. M. Somers, "Design and Experimental Results for a High-Altitude, Long-Endurance Airfoil," *Journal of Aircraft*, vol. 26, no. 2, pp. 148–153, 1989.

[7] K. Biber and C. P. Tilmann, "Supercritical Airfoil Design for Future HALE Concepts," AIAA Paper 2003-1095, 2003.

[8] B. Morrisey and R. McDonald, "Multidisciplinary Design Optimization of an Extreme Aspect Ratio HALE UAV," AIAA Paper 2009-6949, 2009.

[9] D. Cerra and J. Katz, "Design and Evaluation of a High-Lift, Thick Airfoil for UAV Applications," AIAA Paper 2008-292, 2008.

[10] W. H. Phillips, "Some Design Considerations for Solar-Powered Aircraft," NASA Technical Paper 1675, 1980.

[11] F. Johnson, "Sensor Craft 'Tomorrow's Eyes and Ears of the Warfighter'," AIAA Paper 2001-4370, 2001.

[12] M. Drela, "Transonic Low-Reynolds Number Airfoils," *Journal of Aircraft*, vol. 29, no. 6, pp. 1106–1113, 1992.

[13] J. G. Coder, M. D. Maughmer, and D. M. Somers, "Theoretical and Experimental Results for the S414, Slotted, Natural-Laminar-Flow Airfoil," *Journal of Aircraft*, vol. 51, no. 6, pp. 1883–1890, 2014.

[14] M. D. Maughmer, J. G. Coder, and D. M. Somers, "Exploration of a Slotted, Natural-Laminar-Flow Airfoil Concept," AIAA Paper 2018-3815, 2018.

[15] U. Cella, D. Quagliarella, and R. Donelli, "Design and Optimization of a Transonic Natural Laminar Flow Airfoil," Associazione Italiana Di Aeronautica e Astronautica (AIDAA), 2005.

[16] F. K. Viken, S. A. Viken, W. Pfenninger, H. L. Morgan, Jr., and C. R. L, "Design of the Low-Speed NLF(1)-0414F and the High-Speed HSNLF(1)-0213 Airfoils with High-Lift Systems," NASA 90-12540, 1987.

[17] F. Saeed and M. S. Selig, "Multipoint Inverse Airfoil Design Method for Slot-Suction Airfoils," *Journal of Aircraft*, vol. 33, no. 4, pp. 708–715, 1996.

[18] A. S. W. Thomas, *Active Wave Control of Boundary-Layer Transition*, pp. 179–199. Viscous Drag Reduction in Boundary Layers, Progress in Astronautics and Aeronautics, AIAA, 1989.

[19] A. Duchmann, B. Simon, P. Magin, C. Tropea, and S. Grundmann, "In-Flight Transition Delay with DBD Plasma Actuators," AIAA Paper 2013-0900, 2013.

[20] E. J. Richards, W. S. Walker, and J. R. Greening, "Tests of a Griffith Aerofoil in the 13 ft x 9 ft Wind Tunnel," Aeronautical Research Council Reports and Memoranda No. 2148-7561, 1944.

[21] A. Perry, P. J. Ansell, M. F. Kerho, G. Ananda, and S. D'Urso, "Design, Analysis, and Evaluation of a Propulsive Wing Concept," AIAA Paper 2016-4178, 2016.

[22] F. Goldschmied, "Thick-Wing Spanloader All-Freighter: Design Concept for Tomorrow's Air Cargo," AIAA Paper 1990-3198-CP, 1990.

[23] F. Saeed and M. S. Selig, "A New Class of Airfoils with Slot-Suction," AIAA Paper 1996-0058, 1996.

[24] M. Kerho, B. Kramer, P. J. Ansell, S. D'Urso, G. Ananda, and A. Perry, "Design, Analysis, and Evaluation of a Novel Propulsive Wing Concept," Rolling Hills Research Corporation, NNX15AE39A, El Segundo, CA, 2016.

[25] C. D. Gray, "Design and Development of a Continuous, Open-Return Transonic Wind Tunnel Facility," Thesis, Department of Aerospace Engineering, University of Illinois at Urbana-Champaign, Urbana, IL, 2017.

[26] V. Kulkarni, N. Sahoo, and S. D. Chavan, "Simulation of Honeycomb-Screen Combinations for Turbulence Management in a Subsonic Wind Tunnel," *Journal of Wind Engineering and Industrial Aerodynamics*, vol. 99, no. 1, pp. 37–45, 2011.

[27] R. Loehrke and H. Nagib, "Control of Free-Stream Turbulence by Means of Honeycombs: a Balance Between Suppression and Generation," *Journal of Fluids Engineering*, vol. 98, no. 3, pp. 342–351, 1976.

[28] S. M. Batill, M. J. Caylor, and J. J. Hoffman, "An Experimental and Analytic Study of the Flow Subsonic Wind Tunnel Inlets," AFWAL-TR-3109, 1983.

[29] B. H. Goethert, *Transonic Wind Tunnel Testing*, ch. 2. Mineola, New York: Dover, 2007.

[30] U. Cella, D. Quagliarella, R. Donelli, and B. Imperatore, "Design and Test of the UW-5006 Transonic Natural-Laminar-Flow Wing," *Journal of Aircraft*, vol. 47, no. 3, pp. 783–795, 2010.

[31] M. Drela and H. Youngren, "XFOIL 6.94 User Guide," 2001.

[32] R. C. Pankhurst and D. W. Holder, *Wind-Tunnel Technique: An Account of Experimental Methods in Low- and High-Speed Wind Tunnels*, ch. 6. London: Sir Isaac Pitman & Sons, LTD., 1952.

[33] M. Mokry, Y. Y. Chan, and D. J. Jones, "Two-Dimensional Wind Tunnel Wall Interference," AGARD-AG-281, 1983.

[34] W. M. B. Sewall, "Effects of Sidewall Boundary Layers in Two-Dimensional Subsonic and Transonic Wind Tunnels," *AIAA Journal*, vol. 20, no. 9, pp. 1253–1256, 1982.

[35] J. Jin, X. Ren, C. Gao, J. Xiong, F. Liu, and S. Luo, "Analysis of Effects of Wall Interference on 0.4x0.8-Meter Transonic Wind Tunnel Airfoil Tests," AIAA Paper 2013-0641, 2013.

[36] R. J. Adrian and J. Westerweel, *Particle Image Velocimetry*. Cambridge University Press, 2011.

[37] D. Brown, T. Cole, B. Peters, J. Wilson, and G. Havener, "CFI-Shadowgraph/Schlieren Photography for Aerodynamic Applications," AIAA Paper 1994-2616, 1994.

[38] G. S. Settles, *Schlieren and Shadowgraph Techniques: Visualizing Phenomena in Transparent Media*. Springer Science & Business Media, 2012.

[39] P. J. Ansell, "Unsteady Modes in the Flowfield About an Airfoil with a Leading-Edge Horn-Ice Shape," Ph.D. Dissertation, Department of Aerospace Engineering, University of Illinois at Urbana-Champaign, Urbana, IL, 2013.

[40] J. S. Bendat and A. G. Piersol, *Random Data: Analysis and Measurement Procedures*, ch. 11. Hoboken, New Jersey: John Wiley & Sons, Inc., 4 ed., 2010.

[41] N. Sudani, M. Sato, H. Kanda, and K. Matsuno, "Flow Visualization Studies on Sidewall Effects in Two-Dimensional Transonic Airfoil Testing," *Journal of Aircraft*, vol. 31, no. 6, pp. 1233–1239, 1994.

[42] Y. Su, "Mechanism of Sidewall Effect Studied with Oil Flow Visualization," *AIAA Journal*, vol. 27, no. 12, pp. 1828–1830, 1989.

[43] L. Veldhuis and J. van Craenenbroeck, "Analysis of Multi-Element Airfoil High Lift Improvement by Efficient Upper Surface Suction," AIAA Paper 2017-1211, 2017.

[44] S. Goldstein, "Low-Drag and Suction Airfoils," *Journal of the Aeronautical Sciences*, vol. 15, no. 4, pp. 189–214, 1948.

[45] I. H. Abbott and E. Albert, *Theory of Wing Sections*. Mineola, New York: Dover, 1959.

[46] L. L. Pauley, P. Moin, and W. C. Reynolds, "The Structure of Two-Dimensional Separation," *Journal of Fluid Mechanics*, vol. 220, pp. 397–411, 1990.

[47] E. Malkiel and R. Mayle, "Transition in a Separation Bubble," *Journal of Turbomachinery*, vol. 118, no. 4, pp. 752–759, 1996.

[48] L. L. Levy Jr., "Experimental and Computational Steady and Unsteady Transonic Flows about a Thick Airfoil," *AIAA Journal*, vol. 16, no. 6, pp. 564–572, 1978.

[49] H. Schlichting, *Boundary-Layer Theory*, ch. XIII. New York: McGraw-Hill, 7 ed., 1979.

[50] A. R. Collazo Garcia, III and P. J. Ansell, "Characterization of a Griffith-Type Transonic, Laminar-Flow Airfoil," *Journal of Aircraft*, accessed April 1, 2019.

[51] H. W. Coleman and W. G. Steele, *Experimentation and Uncertainty Analysis for Engineers*, pp. 40–118. Hoboken, New Jersey: John Wiley & Sons, Inc., 3 ed., 2009.

[52] S. J. Kline and F. A. McClintock, "Describing Uncertainties in Single Sample Experiments," *Mechanical Engineering*, vol. 75, no. 1, pp. 3–8, 1953.

[53] D. R. Neal, A. Sciacchitano, B. L. Smith, and F. Scarano, "Collaborative Framework for PIV Uncertainty Quantification: the Experimental Database," *Measurement Science and Technology*, vol. 26, no. 7, p. 074003, 2015.

[54] A. Sciacchitano, D. R. Neal, B. L. Smith, S. O. Warner, P. P. Vlachos, B. Wieneke, and F. Scarano, "Collaborative Framework for PIV Uncertainty Quantification: Comparative Assessment of Methods," *Measurement Science and Technology*, vol. 26, no. 7, p. 074004, 2015.

[55] B. Wieneke, "PIV Uncertainty Quantification from Correlation Statistics," *Measurement Science and Technology*, vol. 26, no. 7, p. 074002, 2015.